Developing a charge plunger method for lifetime measurements in heavy elements

Thesis submitted in accordance with the requirements of
the University of Liverpool for the degree of Doctor in Philosophy
by

Jacob A. M. Heery

Oliver Lodge Laboratory
University of Liverpool

October 2021

UNIVERSITY OF
LIVERPOOL

"Science makes people reach selflessly for truth and objectivity; it teaches people to accept reality, with wonder and admiration, not to mention the deep awe and joy that the natural order of things brings to the true scientist."

- Lise Meitner

Acknowledgements

Firstly, I would like to thank my supervisor Prof. Rodi Herzberg for giving me the opportunity to study this PhD and for all the support and guidance he has provided along the way.

Thank you, as well, to all those who helped out on the M16 experiment that took place at the University of Jyväskylä Accelerator Laboratory in June-July 2019. I would like to pay special thanks to Dr. Nara Singh Bondili, Dr. Claus Müller-Gatermann, Dr. Jan Sarén, Dr. Juha Uusitalo, Liam Barber and Dr. Dave Cullen for their helpful comments and advice on the various aspects of this work.

A second thank you to Rodi and Nara Singh for reading through several drafts of this thesis and providing their expertise to help improve it.

I am grateful to the STFC for providing the financial support that enabled me to conduct this research, and providing funding for a long term attachment at the University of Jyväskylä. I am also grateful to Prof. Paul Greenlees for helping arrange this LTA.

I have immensely enjoyed being a member of the Liverpool Nuclear Physics Group and would like to thank all members of the group for providing wonderful colleagues to work with over the past four years.

Finally, I would like to thank my family for their constant support throughout my PhD, especially my mum, dad and Sarah. Sarah, thank you for your patience with me throughout the Covid pandemic, even whilst you were writing your own thesis!

Abstract

The use of the charge plunger method with a mass recoil separator provides a means of measuring the lifetime of low-lying states in exotic nuclei which de-excite via transitions with large internal conversion coefficients. These lifetime measurements provide tests for theoretical models predicting the structure of nuclei far from stability.

The charge plunger method was used in an experiment at the University of Jyväskylä Accelerator Laboratory with the purpose of measuring the lifetime of excited states in ^{178}Pt which de-excite through γ-ray transitions and internal electron conversions. The DPUNS plunger device was connected to the in-flight mass separator MARA which separated ions by their charge state. Ionic charge-state distributions (CSD) were then observed at the focal plane of MARA. The JUROGAM 3 spectrometer surrounded DPUNS and was used to select ions in coincidence with γ-ray transitions in ^{178}Pt .

Ionic charges were selected by MARA and measured at the focal plane in coincidence with the $4^+_1 \rightarrow 2^+_1$ 257 keV γ-ray transition detected using JUROGAM 3 . The resulting CSD were analysed using the differential decay curve method (DDCM) framework to obtain a lifetime value of $430(20)$ ps for the 2^+_1 state in ^{178}Pt .

As an alternative analysis, ions were selected in coincidence with the ^{178}Pt alpha decay ($E_{\mathrm{alpha}} = 5.458(5)$ MeV) in the double-sided silicon strip detector (DSSSD) at the focal plane of MARA. Lifetime information was obtained by fitting a two-state Bateman equation to the decay curve with the lifetime of individual states defined by a single quadrupole moment. This yielded a lifetime value of $430(50)$ ps for the 2^+_1 state, and $54(6)$ ps for the 4^+_1 state. An analysis method based around the Bateman equation will become especially important when using the charge plunger method for the cases where utilising coincidences between prompt γ rays and recoils is not feasible.

Publications based on this thesis work

Lifetime measurements of yrast states in ^{178}Pt using the charge plunger method with a recoil separator

J. Heery, L. Barber, J. Vilhena, B.S. Nara Singh, R.-D. Herzberg, D.M. Cullen, C. Müller-Gatermann, G. Beeton, M. Bowry, A. Dewald, T. Grahn, P.T. Greenlees, A.Illana, R. Julin, S. Juutinen, J.M. Keatings, M. Luoma, D. O'Donnell, J. Ojala, J. Pakarinen, P. Rahkila, P. Ruotsalainen, M. Sandzelius, J. Sarén, J. Sinclair, J.F. Smith, J. Sorri, P. Spagnoletti, H. Tann, J. Uusitalo, G. Zimba. *European Physics Journal A*, 57, (2021).

DOI 10.1140/epja/s10050-021-00425-8.

URL `https://link.springer.com/article/10.1140/epja/s10050-021-00425-8`.

A charge plunger device to measure the lifetimes of excited nuclear states where transitions are dominated by internal conversion

L. Barber, J. Heery, D.M. Cullen, B.S. Nara Singh, R.-D. Herzberg, C. Müller-Gatermann, G. Beeton, M. Bowry, A. Dewald, T. Grahn, P.T. Greenlees, A.Illana, R. Julin, S. Juutinen, J.M. Keatings, M. Luoma, D. O'Donnell, J. Ojala, J. Pakarinen, P. Rahkila, P. Ruotsalainen, M. Sandzelius, J. Sarén, J. Sinclair, J.F. Smith, J. Sorri, P. Spagnoletti, H. Tann, J. Uusitalo, J. Vilhena, G. Zimba. *Nuclear Instruments and Methods in Physics Research Section A: Accelerators, Spectrometers, Detectors and Associated Equipment*, 979:164454, 2020.

DOI 10.1016/j.nima.2020.164454.

URL `https://www.sciencedirect.com/science/article/pii/S0168900220308512`.

Contents

4 Experimental Methodology and Apparatus 52

5 Analysis and Results 74

6 Discussion and Future Work 96

Chapter 1

Introduction

The length of time for which a nuclear state exists before transitioning to another state is inherently random and cannot be precisely predicted. Instead only the general timescale for the transition can be predicted, called the lifetime of the state. The lifetime is a fundamental property which is related by the electromagnetic operator to the wavefunction of the nuclear states involved. It therefore constitutes an important measurable quantity, and lifetime measurements play a crucial role in shaping our understanding of the nuclear landscape. Lifetime measurements have shed light on a number of nuclear structure phenomena, including shape coexistence, proton-neutron correlations, and the role of three-body forces [Hey11, Del10, For13, Cie20]. Measuring the limits of existence at the very edges of stability will shed light on the subtleties of the nuclear force. As such, the development of existing techniques in order to perform these measurements is an important area of research in nuclear physics.

Plunger techniques have been often employed for lifetime measurements of excited nuclear states [Nol79, Dew12]. The most common plunger method is the recoil distance Doppler-shift (RDDS) technique [Ale70, Dew12]. The RDDS technique relies on populating excited states in a nucleus (through e.g. Coulomb excitation, fusion-evaporation reactions, etc., with a beam and target setup) that is moving with some velocity and then reducing its velocity by using a foil. The technique relies on the Doppler shift of the energy of a γ ray in the laboratory frame when emitted from a moving nucleus. The amount that the energy is Doppler shifted by depends on the velocity of the nucleus. When the nucleus is at rest then the energy of a γ ray in the laboratory frame will be the same as the energy in the rest frame of the nucleus, i.e. it is not Doppler shifted. The applicability of the RDDS technique depends on the ability to measure the differences in the Doppler shifts of the γ-ray transitions. The method is less efficient, and in some cases impractical, for measuring the lifetime of excited states that de-excite predominantly by the internal conversion process, i.e., the nuclear de-excitation proceeds via the emission of an atomic electron instead of a γ ray.

In the heavy region of the nuclear chart ($Z \geq 90$), there is much less information on the lifetime of non-isomeric states. This is, in part, a consequence of the reasons stated above. Internal conversion coefficients are seen to increase with proton number and nuclear level schemes display strong collective modes of excitation, resulting in low-energy transitions between states. For example, the 2_1^+ transition in ^{254}No lies at 44 keV, and de-excites to the 0_1^+ ground state. The ratio at which the de-excitation proceeds via internal conversion to γ-ray emission is 1510 : 1 [Kib08].

A second problem arises from the slow velocities at which heavy nuclei in this region are produced in fusion-evaporation reactions. This will result in a small Doppler shift for low-energy transitions. For example, in the reaction ^{208}Pb(^{48}Ca, 2n)^{254}No at a beam energy of 219 MeV, the recoils are produced moving at a velocity of $v/c \sim 2\%$ [Her06]. For the $6^+ \rightarrow 4^+$ 160 keV transition, this results in a Doppler shift of $\sim$1 keV. This is similar to the typical full width half maximum (FWHM) of a germanium detector, FWHM $\approx$ 1.14 keV at 122 keV [Ebe08]. If the recoils were slowed down using a foil, as is required in an RDDS experiment, the widths of the Doppler shifted γ-ray peaks would be similar to or greater than the difference between the peaks. Therefore, it would be difficult to resolve between the two Doppler-shifted γ-ray peaks. As stated above, the ability to measure the differences in the Doppler shifts of a γ-ray transition is an important aspect of the RDDS technique.

Given the large internal conversion probabilities, the slow velocities that recoils are produced at, and the low cross sections for fusion-evaporation production, e.g. for ^{254}No $\sigma \approx 3\,\mu$b, the RDDS technique is unfavoured as a method of measuring the lifetime of low-lying states in the heavy region of the chart. Currently, lifetime information for low-lying states of even-even transfermium nuclei can only be estimated through empirical formulae and direct experimental lifetime measurements would shed light on a number of physical phenomena including nuclear deformation and alpha and fission decay barriers [Rei99].

Two practical methods for measuring the lifetime of nuclear states that de-excite via strong internal conversion are the charge plunger method, the focus of this work, and the recoil shadow method [Bac78]. The recoil shadow method uses an electron spectrometer to detect electrons from the internal conversion of excited states that de-excite in flight after the target foil. The target is "shadowed" from the spectrometer using a longitudinal semi-cylindrical baffle

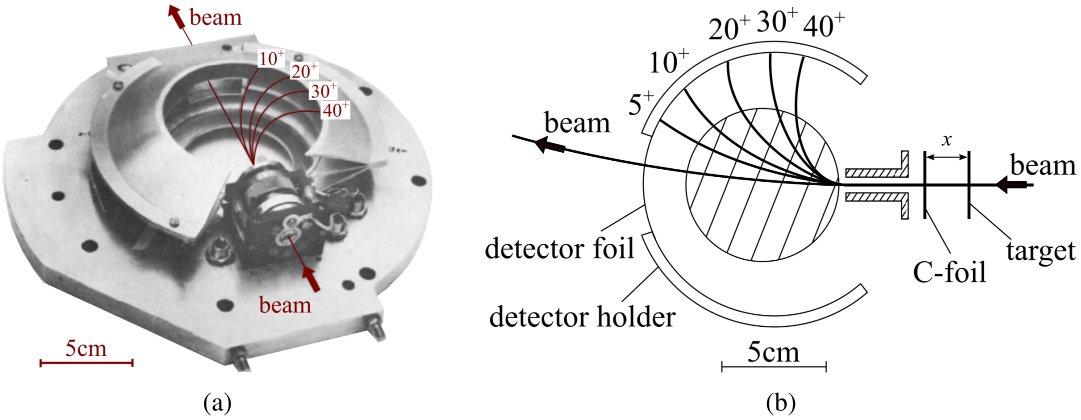

(a) (b)

Figure 1.1: (a) Original experimental setup of the charge plunger method developed during the 1970s and (b) a schematic of the setup. The authors used a tabletop magnet to separate ions after a carbon charge reset foil. The position of an ion on the detector foil was then used to determine the charge state of the ion. The detection system was optimised for studying fissioning nuclei. These figures have been adapted from ref. [Ulf78].

which suppresses the large δ-electron background originating from reactions in the target. Lifetime measurements are then possible by varying the target position. The recoil shadow method is impractical for states which de-excite via low-energy transitions ($E_\gamma \leq 100\,\text{keV}$). For example, in ^{254}No the internal conversion of an electron in the L_1 atomic shell from the $2^+_1 \rightarrow 0^+_1$ 44 keV transition will cause the electron to be emitted with a kinetic energy of $\approx$15 keV [Kib08]. The difference between the binding energies of the L_1 and M_1 shells is $\varepsilon_{L_1} - \varepsilon_{M_1} = 21.55$ keV [Sev79], and therefore the kinetic energies of some emitted Auger electrons will be comparable to the kinetic energy of the internal conversion electron. The presence of Auger electrons, along with the remaining δ-electron background, will complicate the electron energy spectrum. Therefore, the recoil shadow method would not be a suitable choice of method for measuring the lifetime of this state.

The charge plunger method is based on an analysis of changes in the charge-state distribution (CSD) of ions caused by a cascade of Auger electrons that follow internally converted transitions [Ulf78]. After an internal conversion, an atom is left in an excited state. During the atomic relaxation process many Auger electrons can be emitted, leaving the ion in a high charge state (a large excess of protons to electrons). The setup of the charge plunger method is very similar to the RDDS technique, however the stopper foil is replaced by a thin charge reset foil which ions can pass through and be detected on the other side. An ion passing through the reset foil will have its charge state reset to a lower value. Thus the distribution of ionic charge states after the reset foil will contain a low and high charge component, reflecting the proportion of internal conversions occurring before or after the reset foil. The charge plunger method is discussed in more depth in chapter 3.

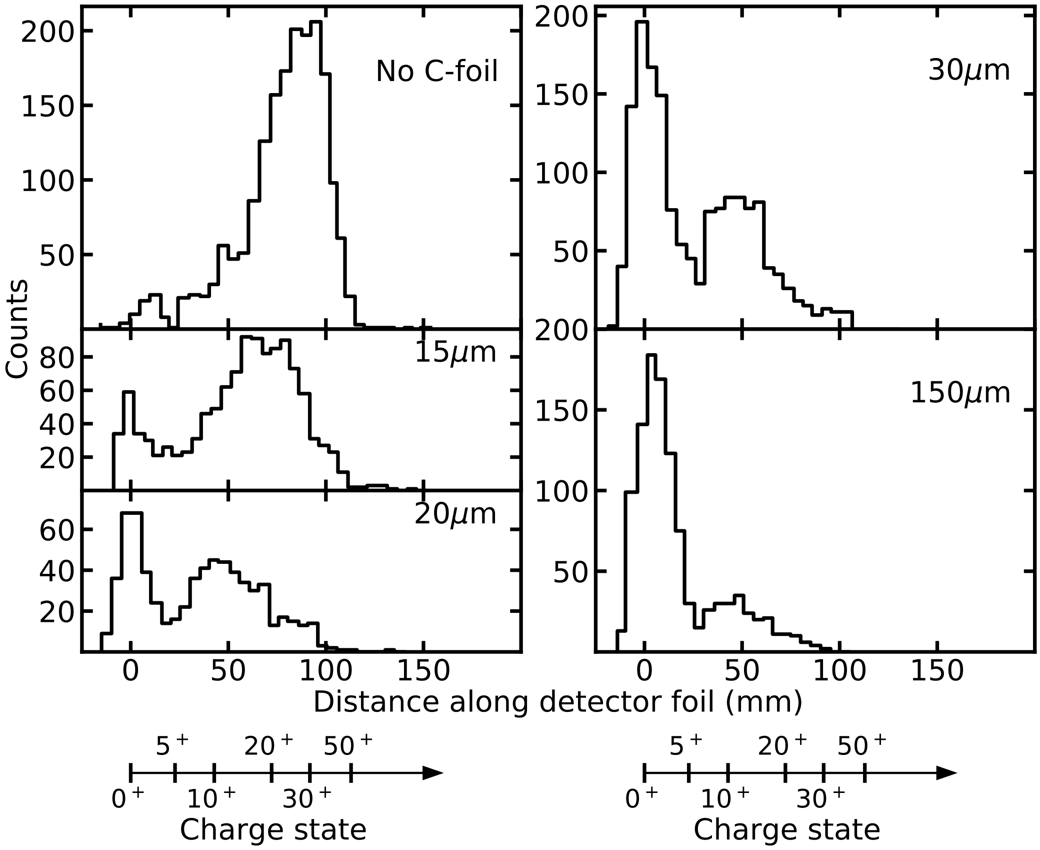

Figure 1.2: Example CSD spectrum using the original charge plunger method setup shown in fig. 1.1. This figure has been adapted from ref. [Hab77].

In refs. [Ulf78, Hab77, Ulf79] the authors used a tabletop magnetic deflector after the reset foil to separate ions by charge and deposit them on to a catcher foil. The distribution of recoils along the catcher foil was then measured offline. The setup is shown in fig. 1.1a along with a schematic in fig. 1.1b. This was done for several target-to-reset foil distances, measured using a micrometer, to determine the change in intensity of high-charge components in the CSD with distance. Fig. 1.2 shows CSD spectra that were measured using this method for the 8 µs fission isomer in ^{239}Pu. High and low charge components are present in the spectrum, with the intensity of high charge components decreasing at larger target-to-reset foil distances. Lifetime information was obtained through either an integral or differential analysis. In the integral analysis the overall de-excitation of a sequence of states such as a rotational band is found by measuring the total yield of highly charged recoils as a function of target-to-reset foil distance. The differential analysis uses the decay curve of the different components in the CSD corresponding to 1, 2, 3 etc. internal conversions after the reset foil to measure the lifetime of individual states in a rotational band. Using this method the authors determined the lifetime of excited states in fission isomers for uranium and plutonium isotopes [Ulf79, Hab77].

More recently the charge plunger method has been developed further in order to extend studies to nuclear states produced with low production cross sections in nuclear reactions [Bar20b, Hee21]. Here, the DPUNS plunger device [Tay13b] was used for improved control of the distance between the target and reset foils. The recoils of interest are separated from the beam like and fissioning reaction products according to their mass/charge (m/q) ratio by the MARA recoil separator [Sar08] and are transported to the focal plane for their detection by a multiwire proportional counter (MWPC) and a double-sided silicon strip detector (DSSSD). Nuclei of interest can then identified by employing the recoil-decay tagging technique, i.e. using coincidences between the recoil implanted in the DSSSD and the subsequent particle decay [Pau95]. Alternatively, recoils can be identified using γ-ray-recoil coincidences between the prompt γ rays detected at the target position, using the JUROGAM 3 spectrometer [Pak20], and the recoils detected in the MWPC and DSSSD.

The separation of ions in MARA is demonstrated in fig. 1.3. The horizontal (x) position of ions at the focal plane is determined by their m/q value. A comparison of figs. 1.1 and 1.3 shows the change in the scale of the setup between the original method, developed in the 1970s, and the current application of the method in this work. The much larger magnets used in a recoil separator such as MARA allows one to accurately select weakly produced reaction channels, allowing for studies of exotic nuclei far from stability. Clearly, detection of all the ionic charges with one single setting of magnet is preferable. However, the demand for recoil optics over a long distance results in a large spread in the CSD of recoils at the focal plane. Covering the entire distribution would require impractically large detectors. Therefore, to measure the whole CSD, it is necessary to perform a scan over a range of separator settings.

In ref. [Bar20b], ions at the focal plane were selected in coincidence with a γ ray of the feeding transition to the 2_1^+ state in ^{180}Pt, occurring before the reset foil. The intensity of charge components in the CSD were then influenced only by the de-excitation from the 2_1^+ state via the internal conversion process. An analysis within the differential decay curve method (DDCM) [Dew89] framework was performed to obtain the lifetime of the 2_1^+ state in ^{180}Pt. The DDCM analysis, as it was used in ref. [Bar20b], requires the γ-ray coincidence gate to be set on the feeding transition occurring before the reset foil. However, it was not possible to resolve the Doppler-shifted components of the $4_1^+ \rightarrow 2_1^+$ feeding transition occurring before and after the reset foil. Therefore, the analysis was restricted to data points taken at longer distances where the feeding transition always occurs before the reset foil.

In ref. [Hee21] (the present work), the lifetime of the 2_1^+ state in ^{178}Pt is also obtained by applying a DDCM analysis to the CSD of ions detected in coincidence with the $4_1^+ \rightarrow 2_1^+$

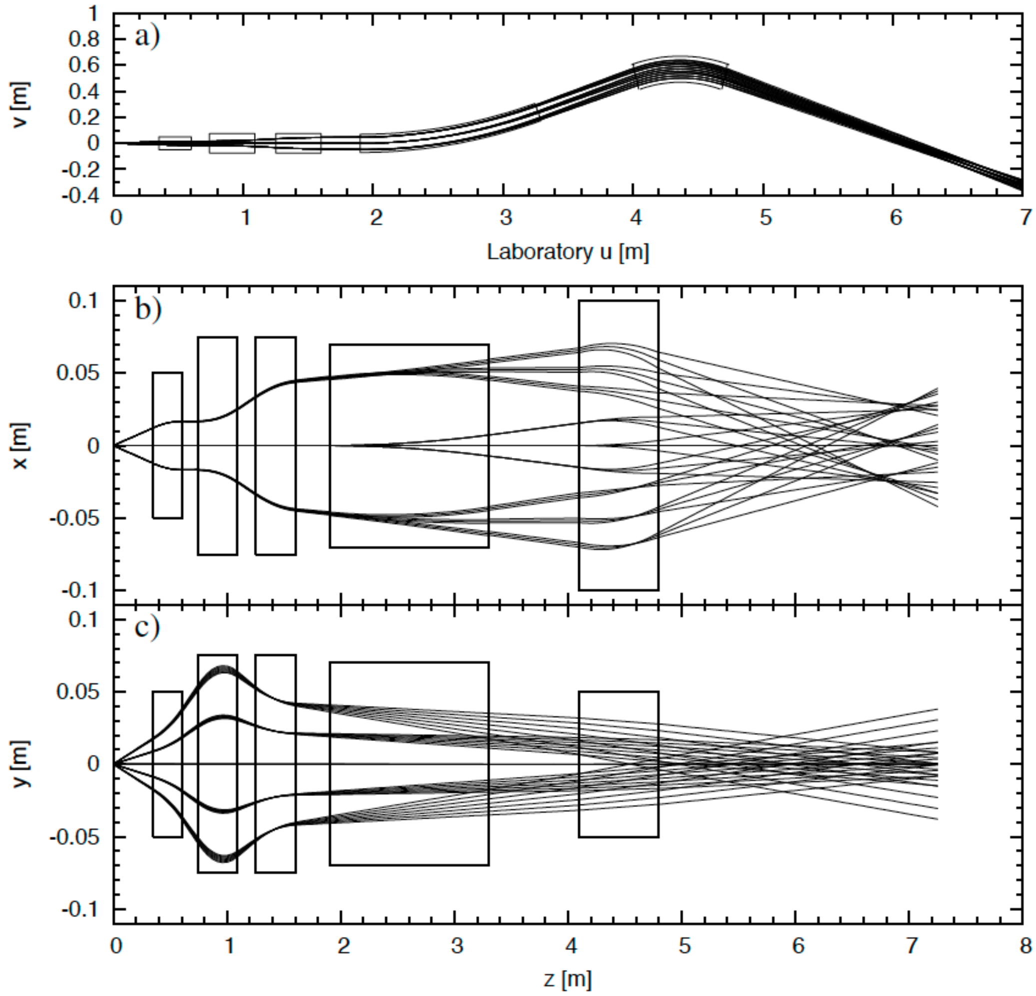

Figure 1.3: The trajectories of ions in MARA viewed (a) from above in the laboratory coordinate system, (b) from above with the straightened optical axis, and (c) from the side with the straightened optical axis. From left to right the elements of MARA are QQQED, where Q are the quadrupole focusing magnets, E is the electrostatic deflector and D is the dipole magnet. The different trajectories shown are for varying ion mass/charge (m/q) ratios. Panel (b) shows that the horizontal (x) position of an ion at the focal plane ($z \sim 7$ m) is dependent on its m/q ratio. This figure has been taken from ref. [Sar11]. For more details on MARA see section 4, or refs. [Sar11, Sar08].

257 keV feeding transition. As in ref. [Bar20b], it was not possible to resolve the Doppler-shifted components of the feeding transition occurring before and after the reset foil. Therefore the analysis was again restricted to data points taken at longer distances where the γ-ray de-excitation from the 4_1^+ state always occurs before the reset foil.

The present work also builds on the charge plunger analysis techniques by developing a Bateman method of analysis. Here, a fit is applied to the intensity of charge states in the CSD at varying distances using the Bateman equation. This takes into account the de-excitation properties of higher energy states feeding the level of interest and, as such, will incorporate more unknowns and free parameters than a DDCM analysis. The benefit of this type of analysis is that one can apply an analysis procedure for charge plunger experiments which is not dependent on observing the γ-ray emission of the feeding transition. This would be especially important for cases where the DDCM is unsuitable due to either low production cross sections, where coincidence analyses are limited due to low statistics, or the presence of multiple highly converted transitions in a band.

To perform the Bateman analysis, CSD spectra were obtained by detecting recoiling ions in coincidence with a characteristic 5.5 MeV ^{178}Pt ground-state alpha decay (branching ratio $\sim 7.5\%$) in the DSSSD [Sch80a]. The CSD is then influenced by the internal conversion of transitions other than the $2_1^+ \rightarrow 0_1^+$ 170 keV transition. The lifetime of the 2_1^+ and 4_1^+ states were then obtained using the Bateman equation, accounting for the de-excitation of two states.

In this work the charge plunger method was used to obtain an accurate measurement for the lifetime of the 2_1^+ state in ^{178}Pt. This state is difficult to measure using the RDDS technique due to both the substantial internal conversion coefficient for the $2_1^+ \rightarrow 0_1^+$transition ($\alpha = 0.63$ [Kib08]) and the slow velocity that recoils are produced at in fusion-evaporation experiments ($v/c = 1.77(2)$ in this work). Additionally, the ability of the charge plunger method to obtain lifetime information has no dependence on the energy of the transition depopulating the excited state, unlike the recoil shadow method. The charge plunger method, therefore, represents an ideal technique for measuring the lifetime of the 2_1^+ state in ^{254}No. This would be the first such measurement of a non-isomeric excited state in the transfermium region of the nuclear landscape.

Chapter 2

Theoretical Framework

2.1 Transitions between quantum states

The wavefunction of a particle is defined with separable position, $\vec{r}$, and time, t, components, the solutions for which are determined by the well known time-dependent Schrödinger equation,

$$|\Psi(\vec{r},t)\rangle = e^{-i\omega t}\,|\psi(\vec{r})\rangle \quad , \tag{2.1}$$

where $\omega = E/\hbar$ and E is the energy eigenvalue of the state [Rae08, chap. 2]. The expectation value of an observable, O, of this wavefunction is given by,

$$\langle\hat{O}\rangle = \int \Psi^*\,\hat{O}\,\Psi \;\; d^3\vec{r} = \langle\Psi|\hat{O}|\Psi\rangle \quad , \tag{2.2}$$

where Ψ^* is the complex conjugate of Ψ. The complex conjugate of the time-dependent part of the wavefunction gives $e^{+i\omega t}$. The consequence of this is that all time dependence in equation 2.2 disappears, and the properties of the wavefunction do not change with time. As such, these solutions to the wavefunction are known as stationary states, and they will live forever. The implication of this is that there can be no transitions between true stationary states.

If a small perturbing field, H', is added to the system, the exact solutions to $|\Psi\rangle$ are now only approximate solutions. The perturbation causes an uncertainty in the energy eigenvalue corresponding to a Lorentzian distribution centred on the value E for the stationary state solution [Kra88, chap. 2]. The wavefunction is now,

$$|\Psi(\vec{r},t)\rangle = e^{-i\omega t} e^{\frac{\Gamma}{2\hbar}t} |\psi(\vec{r})\rangle \ \ , \tag{2.3}$$

where the parameter Γ is the width of the Lorentzian distribution, often called the width of the state. The expectation value of an observable of the state, $\langle \hat{O} \rangle$, will contain a factor $\exp\left(\frac{\Gamma}{\hbar}t\right)$ and thus the wavefunction has an associated lifetime,

$$\tau = \frac{\hbar}{\Gamma} \ \ . \tag{2.4}$$

This is the Heisenberg uncertainty principle [Hei27]. The addition of a small perturbing field allows there to be transitions between quantum states which have an associated energy uncertainty. A typical width of a 1 MeV excited nuclear state is of the order $\sim \mu$eV [Lin62], and $\hbar \approx 658$ meV fs, which gives the typical lifetime of an excited nuclear state on the order of ~ 100 ps.

2.2 Transition probability

The probability for an initial quantum state $|\psi_i\rangle$ to transition to a final state $|\psi_f\rangle$ can be calculated using time-dependent perturbation theory and is given by Fermi's golden rule,

$$\lambda_{fi} = \frac{2\pi}{\hbar} \, |\langle \psi_f^0 | \hat{H}' | \psi_i^0 \rangle|^2 \, \rho(E_f) \ \ , \tag{2.5}$$

where $|\psi_i^0\rangle$ and $|\psi_f^0\rangle$ describe the stationary states and $\rho(E_f)$ is the density of final states. The quantity $\langle \psi_f^0 | \hat{H}' | \psi_i^0 \rangle$ is the matrix element for the transition with the operator $\hat{H}'$ [Hey94, chap. 3]. The transition probability λ_{fi} therefore depends on the physical process which causes an uncertainty in the energy eigenvalues of the wavefunction.

2.2.1 Reduced transition probability

An operator can be characterised by the amount of angular momentum it transfers to the state $|\psi_i\rangle$ to transform it into the state $|\psi_f\rangle$ [Boh75a, chap. 1]. It is therefore useful to define nuclear states in terms of their angular momentum quantum number J and the projection of J on to the z-axis $M = -J, -J+1, ..., J$. Here, we are working in the intrinsic frame of the nucleus and ignore any collective effects. The set of transition operators $\hat{H}'_{\lambda\mu}$ ($\mu = -\lambda, -\lambda+1, ...\lambda$) act on an initial state $|J_i, M_i\rangle$ to transfer angular momentum λ with z-axis components μ, creating a final state $|J_f, M_f\rangle$,

$$\sum_{M_i}\sum_{\mu} \langle J_i M_i \lambda \mu | J_f M_f \rangle \, \hat{H}'_{\lambda\mu} \, |J_i, M_i\rangle = \mathscr{N} \, |J_f, M_f\rangle \quad , \tag{2.6}$$

where $\mathscr{N}$ is a normalization constant which is independent of the final magnetic quantum numbers M_f. The transformation coefficients $\langle J_i M_i \lambda \mu | J_f M_f \rangle$ are the Clebsch-Gordan coefficients describing the coupling of angular momenta J_i, M_i and λ, μ to form a state J_f, M_f. It is useful to define the operator in this way as the matrix element in equation 2.5 can now be separated into two parts, a Clebsch-Gordan coefficient which contains all the information of the magnetic quantum numbers μ, M_i and M_f, and another part containing characteristics of the wavefunctions and operator. This is the Wigner-Eckart theorem,

$$\langle J_f, M_f | \hat{H}'_{\lambda\mu} | J_i, M_i \rangle = (2J_f + 1)^{-1/2} \, \langle J_i M_i \lambda \mu | J_f M_f \rangle \, \langle J_f || \hat{H}'_{\lambda} || J_i \rangle \quad , \tag{2.7}$$

where $\langle J_f || \hat{H}'_{\lambda} || J_i \rangle$ is known as the reduced matrix element which has no dependence on the magnetic quantum numbers. In a nuclear transition $J_i \rightarrow J_f$, involving the transfer of angular momentum λ, the total transition probability is proportional to the summation of the transition probabilities $|\langle J_f, M_f | \hat{H}'_{\lambda\mu} | J_i, M_i \rangle|^2$ over the magnetic quantum numbers μ and M_f. This quantity is represented by the reduced transition probability,

$$B(\hat{H}'_{\lambda}, J_i \rightarrow J_f) = \sum_{M_f}\sum_{\mu} |\langle J_f, M_f | \hat{H}'_{\lambda\mu} | J_i, M_i \rangle|^2 = (2J_i + 1)^{-1} |\langle J_f || \hat{H}'_{\lambda} || J_i \rangle|^2 \quad . \tag{2.8}$$

2.3 Electromagnetic emission

2.3.1 γ-ray emission

A nucleus in an energetically excited state can transition to a lower energy state of the same nucleus through the emission of electromagnetic radiation in the form of a γ-ray photon,

$$ {}^{A}_{Z}X^{*} \rightarrow {}^{A}_{Z}X + \gamma \ , \tag{2.9} $$

where the de-excitation must conserve energy, momentum and angular momentum. In the transition of an initial state $E_i(\mathbf{J_i})$ to a final state $E_f(\mathbf{J_f})$, the energy of the γ ray, E_γ, is given by,

$$ E_\gamma = E_i - E_f \ , \tag{2.10} $$

whilst the angular momentum of the γ ray, $\mathbf{L}$, is given by,

$$ \mathbf{L} = \mathbf{J_i} - \mathbf{J_f} \ , \tag{2.11} $$

which gives the possible values for the absolute value of the γ-ray angular momentum L with z component m as,

$$ \begin{gathered} |J_i - J_f| \leq L \leq J_i + J_f \ , \\ M_i - M_f = m \ , \end{gathered} \tag{2.12} $$

where the angular momentum are in units of $\hbar$. The angular momentum values J_i and J_f must both be integer or half-integer values, meaning L has to be an integer value. L is referred to as the multipolarity of the γ ray.

For a each value of L, a γ ray can be described by one of two possible types of wave, electric (E) and magnetic (M), each with opposite parity. An electric transition is associated with a change in the charge distribution of the nucleus and a magnetic transition is associated with a change in the current distribution. The type of wave that describes the γ ray is determined by the parity of the initial (π_i) and final (π_f) states and the multipolarity of the transition. The parity of the γ ray is subject to the following selection rule,

$$\pi(EL) = (-1)^{L} \ , \tag{2.13}$$
$$\pi(ML) = (-1)^{L+1} \ ,$$

where it is possible to see from equation 2.11 that in a transition $J_i \rightarrow J_f$ the γ ray emitted can be a mixture of electric and magnetic multipole radiation with the same parity. In general, the transition probability is greatly reduced towards higher multipole radiation, and so the de-excitation is dominated by the first couple of multipole orders. For example, in a transition $3^+ \rightarrow 2^+$, the emitted γ ray will be dominated by a mixture of $M1$ and $E2$ radiation, whilst the amount of $M3$, $E4$ and $M5$ radiation is negligible [Hey94, chap. 6].

Due to the transverse nature of an electromagnetic wave, it is not possible for photons with angular momentum $L = 0$ to be emitted from the nucleus. The consequence of this, which can be seen from equations 2.12, is that single γ-ray emission is forbidden between two states which both have 0 units of angular momentum. $E0$ transitions can proceed through internal conversion (see section 2.3.2), however $M0$ transitions between states of opposite parity are completely forbidden. This is supported by experimental evidence [Kuh93].

In classical electromagnetism it is convenient to describe the radiation field, emitted from a general charge and current distribution varying periodically with time, as a multipole expansion [Bla52, chap. 7]. The radiated power of a particular multipolarity is then found to be,

$$P(\sigma L) \propto \mathscr{M}(\sigma L)^2 \ , \tag{2.14}$$

where $\mathscr{M}(\sigma L)$ is the amplitude of the electric ($\sigma = E$) or magnetic ($\sigma = M$) multipole moment. To cross over into a quantum mechanical treatment two steps are needed. Firstly, electromagnetic radiation is emitted in quanta of energy E_γ. Secondly, the multipole moment is replaced by the appropriate multipole operator which changes the nucleus from an initial state $|J_i, M_i\rangle$ to a final state $|J_f, M_f\rangle$,

$$H'_{LM} \propto \hat{\mathscr{M}}(\sigma L, M) \ . \tag{2.15}$$

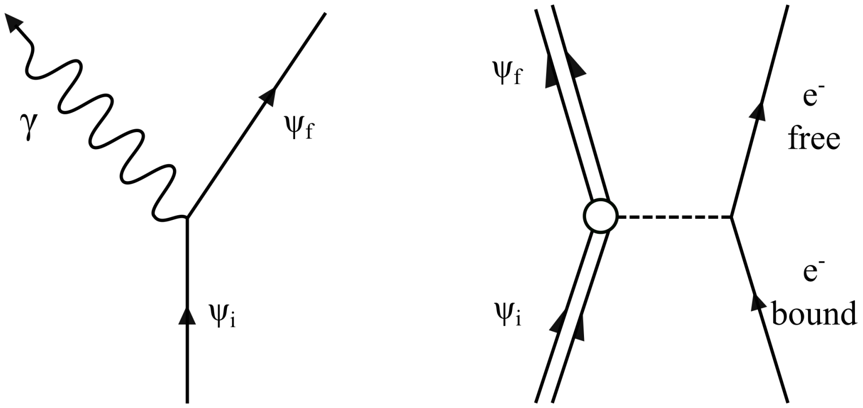

(a) γ-ray emission

(b) Internal conversion electron emission

Figure 2.1: De-excitation from an initial excited nuclear state, ψ_i, to a final state, ψ_f, can proceed by either γ-ray emission (a) or internal conversion (b). In (b), the double line represents the atomic nucleus and the dashed line indicates the direct transfer of energy to the atomic electron via the electromagnetic interaction with no γ ray emitted in the process. These figures have been adapted from ones shown in [Hey94, chap. 6].

The total probability for γ-ray emission in the transition $J_i \to J_f$ is given by,

$$\lambda(\sigma L; J_i \to J_f) = \frac{8\pi(L+1)}{L[(2L+1)!!]^2} \left(\frac{E_\gamma}{\hbar c}\right)^{2L+1} B(\sigma L; J_i \to J_f) \ , \tag{2.16}$$

where,

$$B(\sigma L; J_i \to J_f) \propto \sum_{M_f} \sum_{M} |\langle J_f M_f | \mathscr{M}(\sigma L, M) | J_i M_i \rangle|^2 \ . \tag{2.17}$$

is the reduced transition probability given in equation 2.8 [Boh75a, chap. 3].

2.3.2 Internal conversion

In γ-ray emission the electromagnetic multipole fields of the nucleus radiate energy away from the nucleus in the form of a photon. However, the energy associated with the transition, E_γ, can instead be directly transferred to an atomic electron via the electromagnetic interaction between the nucleus and the electron. This causes the electron to be emitted from the atom, with no γ ray emitted in the process. This process, shown in comparison to γ-ray emission in fig. 2.1, is known as internal conversion.

For the internal conversion of an electron from the i^{th} atomic shell, the energy of the transition must be large enough to overcome the atomic binding energy of the electron, ε_i. The kinetic energy of the emitted electron, E_{e^-}, can therefore be written as,

$$E_{e^-} = E_\gamma - \varepsilon_i \ , \tag{2.18}$$

where the binding energy will depend on the atomic shell that the electron is emitted from. Since internal conversion is a process that competes with γ-ray emission, the total probability for a transition between nuclear states has two components,

$$\lambda_{\text{total}} = \lambda_\gamma (1+\alpha) \ , \tag{2.19}$$

where the internal conversion coefficient, α, is defined as the ratio of the probabilities that the transition proceeds by internal conversion or γ-ray emission,

$$\alpha = \frac{\lambda_{\text{ic}}}{\lambda_\gamma} \ , \tag{2.20}$$

where λ_γ is the transition probability for γ-ray emission, and λ_{ic} is the transition probability for internal conversion. The electron can be ejected from any occupied atomic shell and the internal conversion coefficient can be written more generally as a sum of the conversion coefficients for each shell,

$$\alpha = \alpha_K + \alpha_L + \alpha_M + ... \ , \tag{2.21}$$

where α_i is the internal conversion coefficient relating to the probability of the emission of an electron from the i^{th} atomic shell. The probability that an electron is ejected from a shell is dependent on the strength of the electromagnetic interaction between the nucleus and the electron. This is dominated by the electrostatic Coulomb interaction, which falls off at roughly $1/r$ in the far-field region away from the nucleus, where r is the distance between the nucleus and the electron [Bla52, chap. 7]. Therefore, the conversion coefficients for s-wave (K, L_1, M_1, ...) electrons are generally larger than for other orbitals as they have non-vanishing wavefunctions near the nucleus (see fig. 2.2) [Hey94, chap. 6]).

Estimates for the internal conversion coefficient can be made by comparison of the theoretical transition probabilities for internal conversion and γ-ray emission [Bla52, chap. 7]. Equation

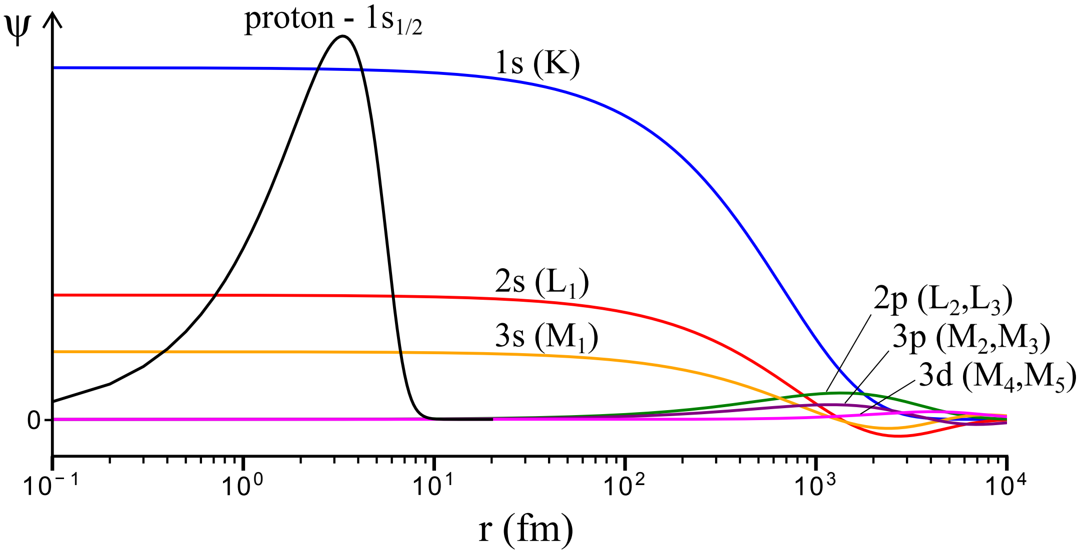

Figure 2.2: Pictorial representation of the overlap between the radial wavefunctions of inner atomic electrons (coloured) and a $1s_{1/2}$ proton (black). The proton wavefunction is calculated for a ^{178}Pt nucleus using the Hartree-Fock method with a Woods-Saxon potential [Hey11, chap. 10]. The electron wavefunctions are calculated for a hydrogenic atom with Z=78 [Kra88, chap. 2]. Only the *s*-wave electrons have a wavefunction with non-vanishing amplitudes around the nuclear region. Therefore, electrons in these orbital have a greater probability of undergoing internal conversion.

2.5, which allows for the transition rate between two quantum states subject to a perturbation H' to be calculated, can be used to estimate the internal conversion transition probability. The perturbation is caused by the electromagnetic field originating from the nucleus and therefore the transition potential for the interaction can be written as a sum over the multipoles of the electromagnetic field [Ban02],

$$H' = \sum_L \sum_M H'_{LM} \ , \tag{2.22}$$

each of which are proportional to the multipole moment operator,

$$H'_{LM} \propto \mathscr{M}(\sigma L, M) \ , \tag{2.23}$$

where only terms of the same parity contribute to equation 2.22 subject to the same selection rules as γ-ray radiation (equation 2.13). The transition probability for internal conversion due to the L^{th}-multipole of the electromagnetic field is therefore,

$$\lambda_{\text{ic}}(\sigma L; J_i \rightarrow J_f) \propto \sum_{M_f} \sum_M |\langle J_f M_f | \mathscr{M}(\sigma L, M) | J_i M_i \rangle|^2 \ , \tag{2.24}$$

where one will notice that the factor $\sum_{M_f}\sum_M |\langle J_f M_f|\hat{\mathscr{M}}(\sigma L,M)|J_i M_i\rangle|^2$, which contains the direct dependence on the nuclear structure, is present in the transition probability for both γ-ray emission and internal conversion (equations 2.16 and 2.24). Therefore, the internal conversion coefficient is independent of nuclear structure effects. However, this is an over-simplification as this calculation does not consider the finite size of the nucleus which leads to a small probability that the initial electron wavefunction penetrates inside the nucleus, where charge and current densities are localised and thus the transition potential, H', felt by the electron changes. This effect is most important for highly hindered transitions where the de-exciting state lives long enough for an inner electron to penetrate the nucleus [Ram02]. In the full calculation, the internal conversion coefficient for a transition is found to,

(a) Increase with increasing atomic number, Z.

(b) Increase with increasing transition multipolarity, L.

(c) Decrease with increasing transition energy, E_γ.

(d) Decrease with increasing principal quantum number of the atomic shell from which the electron is ejected, n_i.

Detailed calculations of internal conversion coefficients are given in tables (see [Ban02, Hag68, Rös78]) or can be looked up using the BrIcc database [Kib08].

2.4 Predicting nuclear transition rates

2.4.1 Single-particle transitions

The independent-particle model can be used to estimate the reduced transition probability for a transition between low-lying states in a nucleus [Ell57, chap. 4]. In this model, the state of a nucleus is described by the quantum numbers of individual nucleons. The multipole matrix elements can be calculated by assuming that a transition from an initial state to a final state, $J_i \rightarrow J_f$, is due to the change of quantum numbers for only one nucleon. In a crude approximation, nucleons are described as non-relativistic point particles with charge ($0e$ for neutrons and $+e$ for protons) and intrinsic magnetic moment. The nucleons are considered free and moving in a mean potential field due to all the other nucleons in the nucleus.

The reduced transition probability for the L^{th} multipole of an electric transition is calculated for the case of a proton moving from J_i to J_f and is given as,

$$B_{sp}(EL;J_i \to J_f) = \frac{e^2}{4\pi}(2L+1)\,\langle J_i\tfrac{1}{2}L0|J_f\tfrac{1}{2}\rangle^2\,\langle J_f|r^L|J_i\rangle^2 \quad , \tag{2.25}$$

where the contribution due to nucleon intrinsic spin is much smaller than the contribution of the charge density and therefore ignored. This does not apply to magnetic transitions however where nuclear intrinsic spin gives a sizeable contribution. For a nucleon (either proton or neutron) involved in the transition J_i to J_f the reduced transition probability for the L^{th} multipole is given as,

$$B_{sp}(ML;J_i \to J_f) = \left(\frac{e\hbar}{2Mc}\right)^2\left(g_s - \frac{2}{L+1}g_l\right)^2 L^2\frac{2L+1}{4\pi}\,\langle J_i\tfrac{1}{2}L0|J_f\tfrac{1}{2}\rangle^2\,\langle J_f|r^{L-1}|J_i\rangle^2 \ , \tag{2.26}$$

where g_s and g_l are the spin and orbital angular momentum g-factors for the nucleon contributing to the transition [Boh75a, chap. 3].

Equation 2.25 can be written more conveniently using the method set out by Weisskopf [Bla52, chap. 7]. The proton, assumed to be in a spin-up state, $s = +1/2$, has initial orbital angular momentum $L\hbar$ and final orbital angular momentum $0\hbar$. The initial and final proton wavefunctions can be written,

$$\begin{aligned} |p_{\text{initial}}\rangle &= u_i(r)Y_{L,M}(\theta,\phi)\chi_{\uparrow} \ , \\ |p_{\text{final}}\rangle &= u_f(r)(4\pi)^{1/2}\chi_{\uparrow} \ , \end{aligned} \tag{2.27}$$

where $u_{i(f)}(r)$ contains the radial dependence of the initial (final) wavefunction, $\chi_{\uparrow}$ is the function for a spin-up particle and $Y_{L,M}(\theta,\phi)$ is a spherical harmonic containing the angular dependence. A simple estimate uses the assumption,

$$u_i(r) = u_f(r) = \begin{cases} \sqrt{\frac{3}{R^3}}, & r \le R \ , \\ 0, & r > R \ , \end{cases} \tag{2.28}$$

Table 2.1: Weisskopf estimates for L^{th} multipole γ transition probabilities between states. The transition probabilities are given in s^{-1} and energies, E_γ, are given in MeV. A is the mass number of the nucleus.

Electric Transitions	Magnetic Transitions
$\lambda(E1) = 1.0\times10^{14}A^{2/3}E_\gamma^3$	$\lambda(M1) = 3.1\times10^{13}E_\gamma^3$
$\lambda(E2) = 7.3\times10^{7}A^{4/3}E_\gamma^5$	$\lambda(M2) = 2.2\times10^{7}A^{2/3}E_\gamma^5$
$\lambda(E3) = 34A^{2}E_\gamma^7$	$\lambda(M3) = 10A^{4/3}E_\gamma^7$
$\lambda(E4) = 1.1\times10^{-5}A^{8/3}E_\gamma^9$	$\lambda(M4) = 3.3\times10^{-6}A^{2}E_\gamma^9$

where the nuclear radius is $R = 1.2A^{1/3}\,\text{fm}$ (A is the mass number of the nucleus). The constant factor $\sqrt{\frac{3}{R^3}}$ is found by normalising the wave functions in equation 2.27. With this assumption, the matrix element in equation 2.25 is of the order $\langle J_f|r^L|J_i\rangle \sim \frac{3R^L}{L+3}$. Equation 2.25 can then be written,

$$B_w(EL) = \frac{(1.2)^{2L}}{4\pi}\left(\frac{3}{L+3}\right)^2 A^{2L/3} \quad , \tag{2.29}$$

with units $e^2(\text{fm})^{2L}$. The magnetic reduced transition probabilities are by convention chosen to be $B_w(ML) \sim 10\left(\frac{\hbar}{McR}\right)^2 B_w(EL)$,

$$B_w(ML) = \frac{10}{\pi}(1.2)^{2L-2}\left(\frac{3}{L+3}\right)^2 A^{(2L-2)/3} \quad , \tag{2.30}$$

with units $\left(\frac{e\hbar}{2Mc}\right)^2(\text{fm})^{2L-2}$. Equations 2.29 and 2.30 can be used in equation 2.16 to gain approximate values for the electromagnetic transition probability of an initial state to a final state. These are shown for low multipolarities in table 2.1.

Often, experimental transition rates are quoted in Weisskopf units (W.u.), such that,

$$B(\sigma L) = \frac{\lambda(\sigma L)_{\text{experiment}}}{\lambda(\sigma L)_{\text{Weisskopf}}} \quad [\text{W.u.}] \ . \tag{2.31}$$

Writing transition probabilities in this way is useful for comparing experimental values to theoretical values predicted by a model involving a single proton. Fig. 2.3 shows experimental $B(E2)$ values in W.u. against proton number for 345 $2_1^+ \to 0_1^+$ transitions in various even-even nuclei across the nuclear chart. The Weisskopf model reproduces transition probabilities well close to magic proton numbers ($Z = 2, 4, 8, 20, 28, 50, 82$) where the shell model [May50] predicts closed shells and excited states are due to single-particle excitations. However, away from the proton magic numbers the Weisskopf estimate is poor at reproducing $B(E2)$ values. In these regions, more than one nucleon contributes to the transition and the Weisskopf calculation can underestimate the $B(E2)$ value for the transition by several orders of magnitude [Bla52, chap. 7]. Predicting $B(E2)$ values for these transitions is covered in 2.4.2.

2.4.2 Collective transitions: the rotational model

In the Bohr-Mottelson rotational model, excited states can also exist due to the collective motion of the nucleus as a whole [Boh75b, chap. 4]. For example the entire nucleus can rotate about some axis. In the intrinsic frame of the nucleus this rotation cannot be observed and nuclear states are defined by the intrinsic configuration of the protons and neutrons in the nucleus. In the laboratory frame the rotation of the nucleus is observed and quantised collective states, corresponding to faster rotational frequency about the axis of rotation, are built upon the intrinsic state.

Rotational motion can only be observed in nuclei with stable deformed shapes. This is due to the impossibility to distinguish between spherical systems that differ only by rotation.

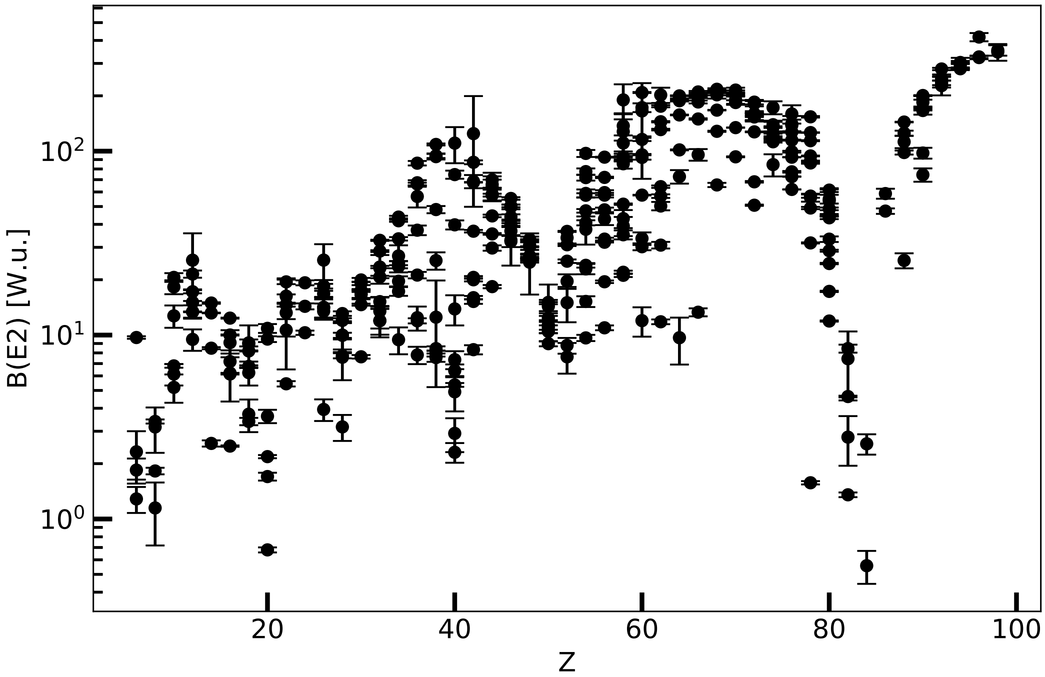

Figure 2.3: $B(E2)$ values in W.u. for $2_1^+ \to 0_1^+$ transitions in even-even nuclei across the nuclear chart. Data are shown for 345 even-even nuclei between $Z = 6 - 98$. $B(E2)$ values reduce significantly around magic Z numbers, giving clear evidence of shell effects [May50]. Data points have been taken from the ENSDF database [ENS], and in some cases is a weighted average from several experiments.

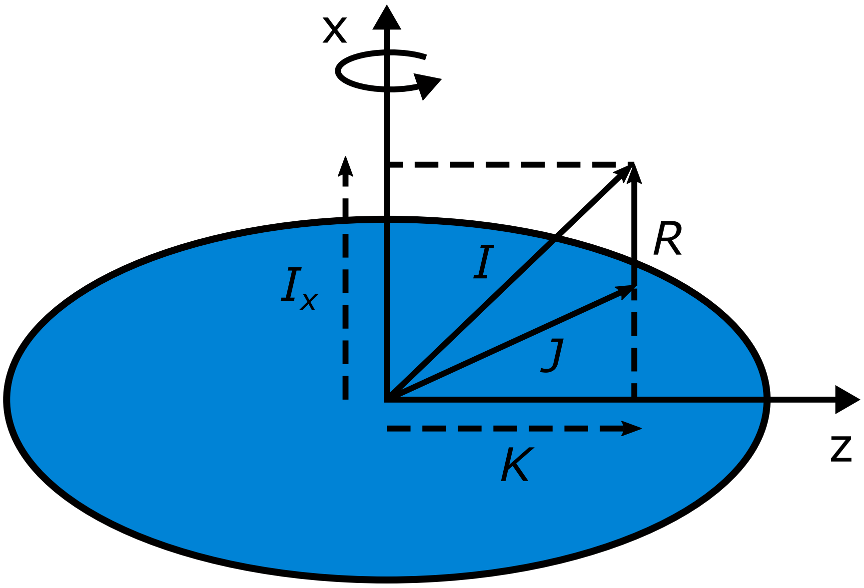

Figure 2.4: Prolate-deformed nucleus showing the coupling of rotational angular momentum **R** to intrinsic single-particle angular momentum **J**, to give total angular momentum **I**. The symmetry axis is z.

The most common non-spherical nuclei are quadrupole deformed, found in the mass ranges $150 < A < 190$ and $A > 220$ [Kra88, chap. 5]. The surface of a quadrupole-deformed nucleus is given by,

$$R(\theta,\phi) = R_0\left[1+\beta Y_{20}(\theta,\phi)\right] \ , \tag{2.32}$$

where $R_0 = 1.2A^{1/3}$ fm and the spherical harmonic $Y_{20}(\theta,\phi) = \sqrt{\frac{5}{16\pi}}(3\cos^2\theta - 1)$ is independent of ϕ, and gives a nuclear shape with cylindrical symmetry. The deformation parameter β is given by,

$$\beta = \frac{4}{3}\sqrt{\frac{\pi}{5}}\frac{\Delta R}{R_0} \ , \tag{2.33}$$

where ΔR is the difference between the semimajor (z) axis and the semiminor (x and y) axes. Shapes with $\beta > 0$ are prolate deformed, whilst shapes with $\beta < 0$ have oblate deformation.

As shown in fig. 2.4 for a prolate deformed nucleus, the angular momentum associated with a rotation **R** couples with the total angular momentum from single-particles states, **J**, to give total angular momentum,

$$\mathbf{I} = \mathbf{R} + \mathbf{J} \ . \tag{2.34}$$

The projection of the total angular momentum onto the symmetry axis gives the quantum number, K. As the rotational angular momentum is perpendicular to the symmetry axis, K is a conserved quantum number, such that changing **R** does not change K.

States with $K = 0$ are labelled by the eigenvalue r such that,

$$r = (-1)^I \ , \tag{2.35}$$

and the rotational spectrum contains states with total angular momentum,

$$\begin{aligned} I &= 0^\pi, 2^\pi, 4^\pi, \ldots \quad r = +1 \ , \\ I &= 1^\pi, 3^\pi, 5^\pi, \ldots \quad r = -1 \ , \end{aligned} \tag{2.36}$$

where π is the parity of the intrinsic system. The energy of states in the band is given by,

$$E_{\mathrm{rot}}(I) = \frac{\hbar^2}{2\mathscr{I}} I(I+1) \ , \tag{2.37}$$

where $\mathscr{I}$ is the effective moment of inertia for the rotating body. Successive states in a $K = 0$ band are connected by stretched $E2$ transitions and detailed information on the deformation can be gained from studying the $E2$-matrix elements connecting transitions in a band. The reduced transmission probability for $E2$ transitions between states in a rotational band is given by,

$$B(E2; I_1 \to I_2) = \frac{5}{16\pi} e^2 Q_0^2 \langle I_1 020 | I_2 0 \rangle \ , \tag{2.38}$$

where Q_0 is the electric quadrupole moment, which gives an idea of the charge distribution in the nucleus. The quadrupole moment is related to the deformation parameter by,

$$Q_0 = \sqrt{\frac{16\pi}{5}} \frac{3}{4\pi} R_0^2 Z e \beta \ , \tag{2.39}$$

where Z is the proton number of the nucleus.

Using equations 2.38 and 2.16 together the lifetime of a level with angular momentum I in a $K = 0$ band is related to the intrinsic quadrupole moment of the nucleus by,

$$\tau(I) = \frac{0.826}{E_\gamma^5 Q_0^2 |\langle I\,020|I{-}2\,0\rangle|^2 (1+\alpha)} \quad [\mathrm{ps}] \ , \tag{2.40}$$

where E_γ is the transition energy in MeV, α is the internal conversion coefficient for the transition, Q_0 is the intrinsic quadrupole moment in units of $e\,$b and $\langle I\,020|I{-}2\,0\rangle$ is the relevant Clebsch-Gordan coefficient. The factor $(1+\alpha)$ is included to account for the probability that the transition proceeds via internal conversion.

2.4.3 Grodzin's rule

Grodzin's rule is a global empirical formula which relates the lifetime for γ-ray emission and excitation energy of the yrast 2^+ state in even-even nuclei [Gro62]. The relationship gives,

$$\tau_\gamma(2_1^+ \to 0_1^+) = (2.74 \pm 0.91) \times 10^{13} E_\gamma^{-4} Z^{-2} A \ , \tag{2.41}$$

where Z is proton number, A is atomic mass number, E_γ is given in keV and τ_γ is in ps. The constant is determined from a best fit to experimental data obtained across the nuclear chart. The transition probability due to internal conversion is not accounted for. The E_γ^{-4} relationship is demonstrated in fig. 2.5.

That a relationship exists between $E(2_1^+)$ and $\tau(2_1^+)$ becomes apparent when one considers that for a classical rigid rotor with charge, the rotational kinetic energy and the electromagnetic power dissipated are both dependent on the shape of the object. The dependence on E_γ^{-4} and Z^{-2} in equation 2.41 can then be understood by considering the collective models of spherical and axially-symmetric deformed nuclei developed by Bohr and Mottelson [Boh75b, chap. 4]. These models, however, are not able to give the correct absolute value for the transition probability and predict a dependence of $A^{-1/3}$. The models also predict discontinuities at the boundaries between vibrating and rotating nuclei. However, as can be seen from fig. 2.5, no such discontinuities have been experimentally measured.

Subsequent work by Raman et al. [Ram89] refined equation 2.41 by keeping the exponents in E_γ and A as free parameters in the best fit,

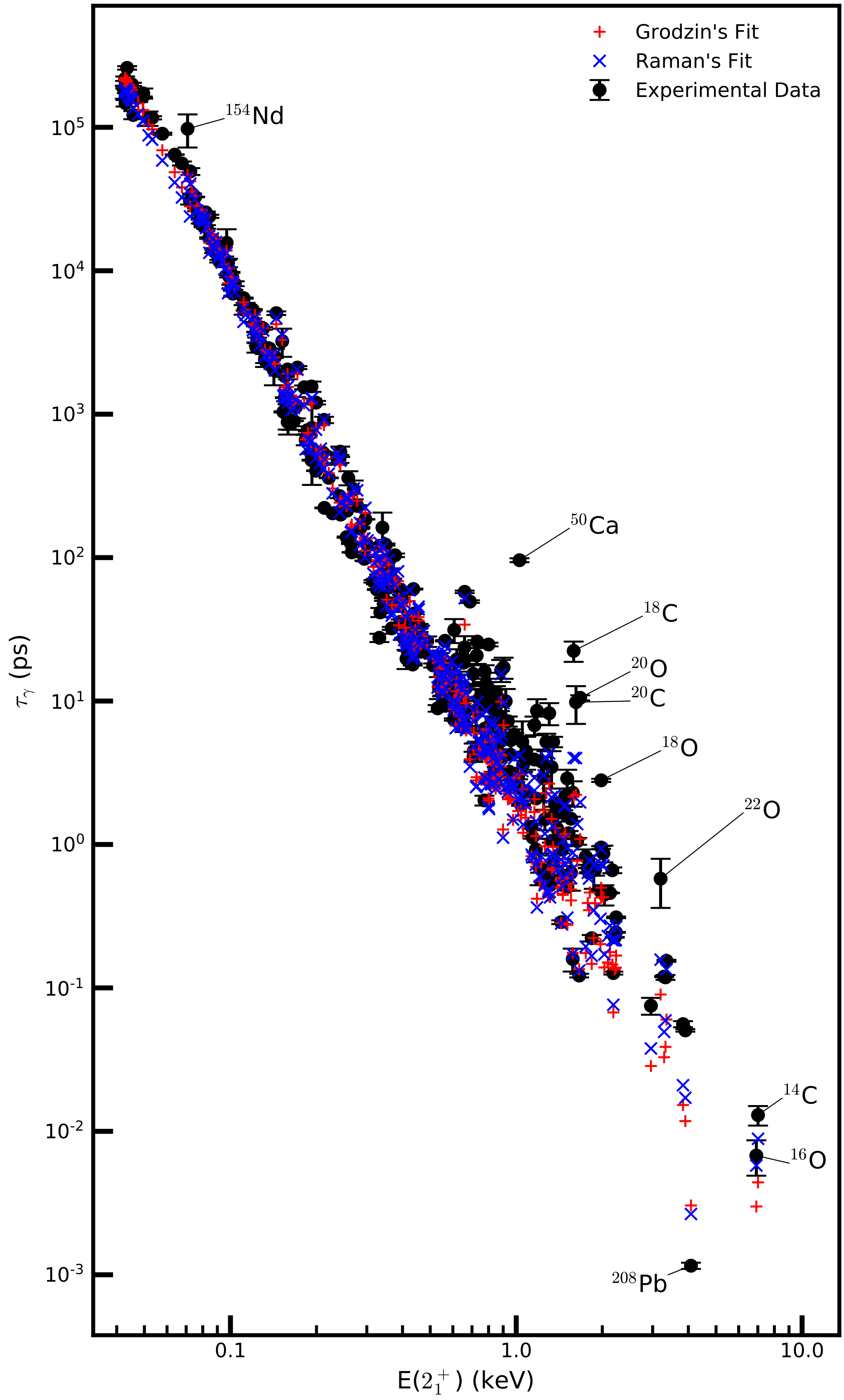

Figure 2.5: Lifetime for γ-ray de-excitation of 2_1^+ state against γ-ray energy. Grodzin's rule gives a global E_γ^4 dependence on the transition probability for $2_1^+ \rightarrow 0_1^+$ transitions. Experimental data are shown along with estimates from Grodzin's and Raman's global fits for 345 even-even nuclei between $Z = 6 - 98$. Error bars are only shown for the experimental data points. Experimental data points have been taken from the ENSDF database [ENS], and in some cases is a weighted average from several experiments..

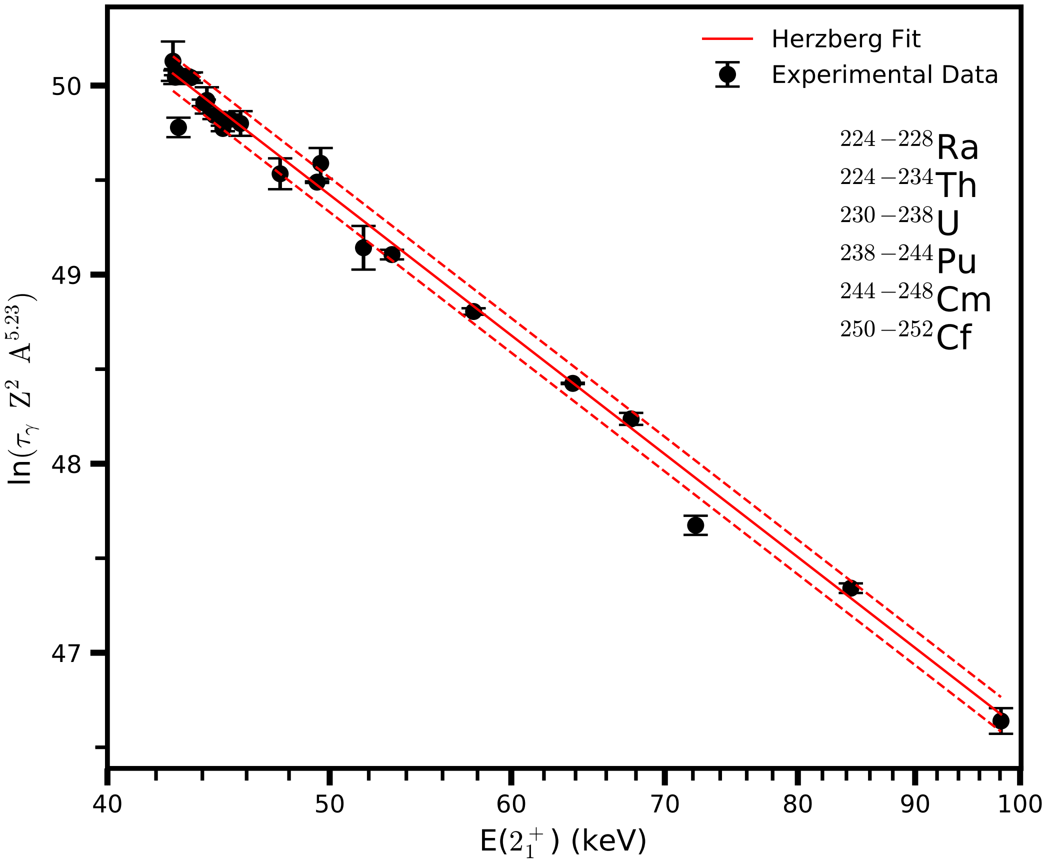

Figure 2.6: Experimental lifetimes versus excitation energy for nuclei with $Z \geq 88$ and $E(2_1^+) < 100$ keV. The fit is a modification to Grodzin's rule adapted for the region of the isotopes shown. The dashed red lines represent the uncertainty of the fit. This figure is adapted from ref. [Her01]. Experimental data points have been taken from the ENSDF database [ENS].

$$\tau_\gamma(2_1^+ \rightarrow 0_1^+) = (1.25 \pm 0.50) \times 10^{14} E_\gamma^{-(4.00\pm0.03)} Z^{-2} A^{(0.69\pm0.05)} \quad . \tag{2.42}$$

Estimates for τ_γ from Grodzin's and Raman's global fits are shown alongside experimental data points for even-even nuclei in the range $Z = 6 - 98$ in fig. 2.5. These experimental data points are taken from the ENSDF database [ENS].

With the availability of more data in recent years, it has been possible to extend these lifetime systematics to heavier regions of the nuclear chart. The actinide nuclei have been observed to lie on a slightly different trajectory to the global fits given in equations 2.41 and 2.42. This is partly due to the substantial hexadecapole deformation seen in this region [Mil77, Zum84, Zum86, Zam95]. In ref. [Her01], Herzberg et al. give a "local fit" which is specific to this region,

$$\ln(\tau_\gamma Z^2) = (65.15 \pm 4.22) - (4.017 \pm 0.111)\ln(E_\gamma) - (5.23 \pm 0.70)\ln(A) \ , \tag{2.43}$$

which gives an overall uncertainty on the lifetime of 14%, within the range of the fit. The "local fit" is shown in fig. 2.6.

2.5 Experimental nuclear lifetime measurements

The measurement of the lifetime of an excited nuclear state provides a good test of theoretical nuclear models predicting the structure of the nucleus. They therefore constitute an important experimental tool. However, lifetime values for excited states vary over a broad range, usually $10^{-15} - 10^{-6}$ s (see fig. 2.5). There are different experimental methods that can be used to perform lifetime measurements, and the choice of method will depend on the lifetime value. Fig. 2.7 shows some of the different methods used for performing measurements for different lifetime regimes [Nol79]. The figure is divided into direct methods, that measure the state lifetime τ, and indirect methods, which measure the state width Γ.

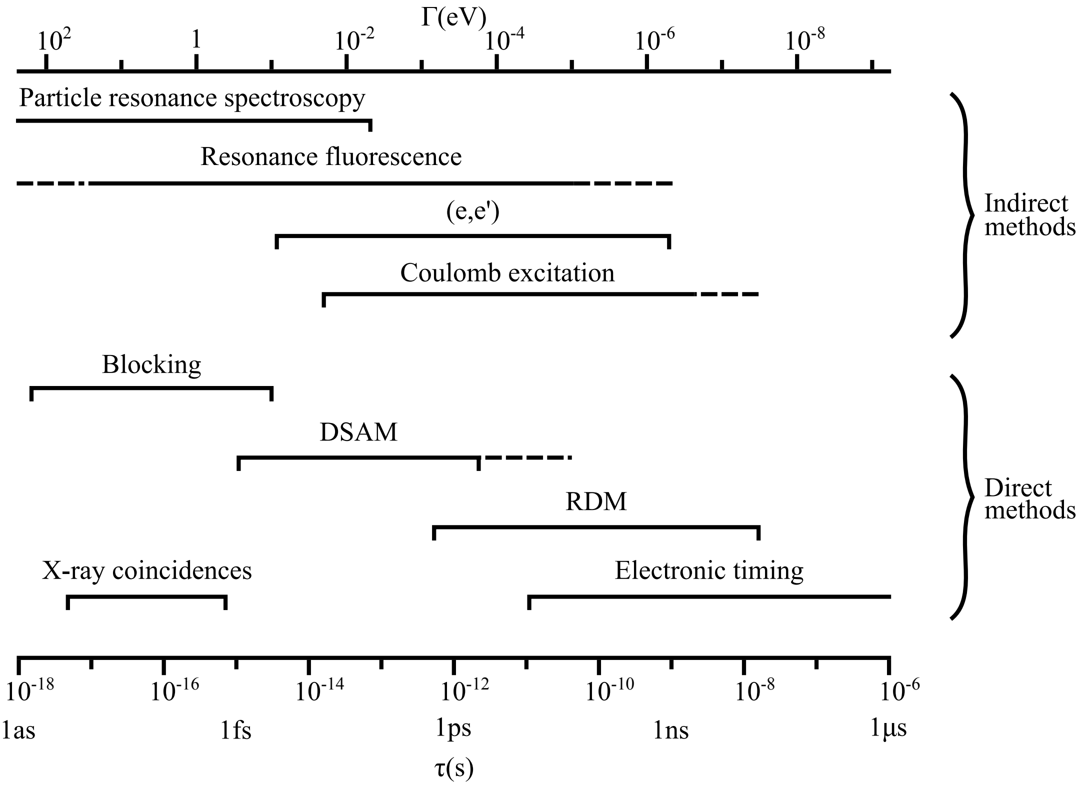

Figure 2.7: Different methods of measuring lifetimes. This figure has been adapted from that in ref. [Nol79].

Many of the lifetime data that contributed to fig. 2.5 were measured using the recoil distance method (RDM) and electronic timing techniques. Electronic timing techniques rely on measuring the time difference between two correlated events (e.g. β-γ or γ-γ coincidences) [Sch63, Mac89, Mos89]. The time difference between events can be measured using either the timestamps of a data acquisition (DAQ) system or time-to-amplitude convertor (TAC) modules. The method relies on good efficiency for detectors in order to detect coincidences between events. The RDM is performed using a plunger setup, and is often associated with the recoil distance Doppler-shift (RDDS) method [Dew12]. The charge plunger method is a variation of the RDM and will be explained in more detail in chapter 3. Information on the other methods shown in fig. 2.7 can be found in ref. [Nol79].

2.6 Changes in ionic charge states

The use of the charge plunger method requires a good understanding of the different physical processes that affect the charge state of an ion. Of particular importance are the phenomena of Auger electron emission and the charge-changing processes which occur when an ion passes through a solid material.

2.6.1 Auger electron emission

When a vacancy is created in an atomic shell (*A*), e.g. after internal conversion, an electron from a higher shell (*B*) will de-excite to fill the vacancy, emitting an X ray in the process.

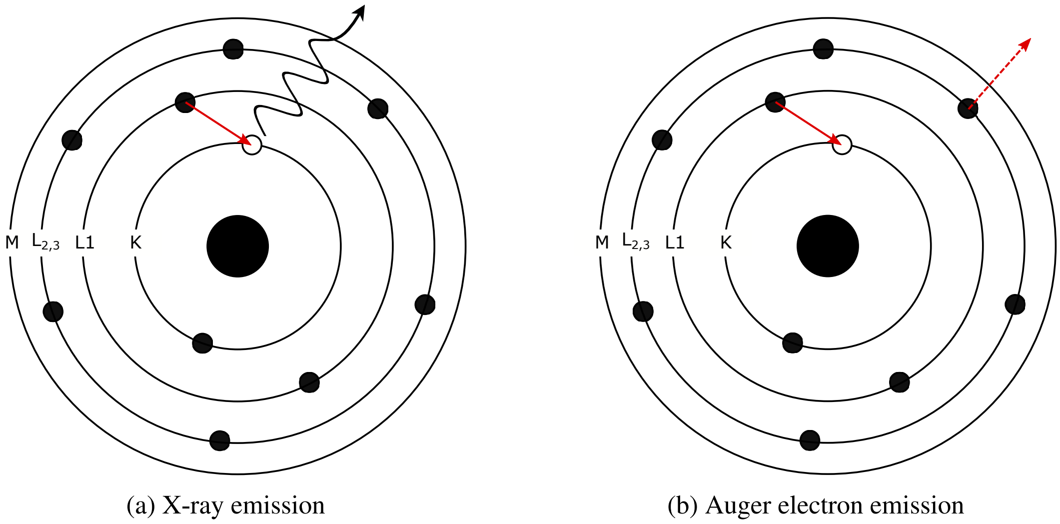

(a) X-ray emission

(b) Auger electron emission

Figure 2.8: Transitions between atomic states can result in (a) X-ray emission or (b) Auger electron emission.

The energy of the X ray is,

$$E_X = \varepsilon_A - \varepsilon_B \ , \tag{2.44}$$

where ε_A and ε_B are the binding energies of the atomic shells involved. However, instead of an X ray being emitted, the energy can be directly transferred to an electron in an outer atomic shell (C) which is then ejected from the atom. This is known as an Auger emission [Mei22, Aug25] and is an atomic process which is analogous to the internal conversion of a nuclear transition. The Auger electron is ejected from the atom with a kinetic energy, E_{e^-},

$$E_{e^-} = E_X - \varepsilon_C^B \ , \tag{2.45}$$

where ε_C^B is the atomic binding energy of an electron in the C atomic shell when the atom is already ionised with a single vacancy in the B atomic shell [Lee12]. The process will result in vacancies in both the B and C atomic shells. The X-ray and Auger emission processes are shown in fig. 2.8.

A nuclear process, such as the emission of an internal conversion electron, that causes a vacancy in an inner atomic shell will result in an atomic cascade as electrons from higher shells de-excite to fill the vacancy [Lee12]. The vacancy will travel up the atomic shells until there are no more electrons to de-excite into it. In the full atomic relaxation process several Auger electrons can be emitted, significantly increasing the charge state of the ion. Since X-ray and Auger emission are competing processes, the number of Auger electrons emitted in a cascade will be a distribution. This distribution has been observed to be Gaussian in character [Car66, Lee13].

To calculate the number of Auger electrons emitted in an atomic cascade, one can follow two approaches. The first is to use empirical formulae to estimate the distribution of final charge states. In ref. [Car66], a vacancy was created in the chosen shell of a neutralised noble gas by irradiating the gas with a tunable monochromatic X-ray source. The final atomic charge state distribution was then analysed using a magnetic spectrometer. Thus the authors obtained empirical curves to describe the average number of electrons emitted following a vacancy in the K, L_1, $L_{2,3}$, M_1, $M_{2,3}$ and $M_{4,5}$ atomic shells as a function of atomic number, Z. The relationship is shown in fig. 2.9. Ref. [Car66] does not give information on how the width of the charge distribution due to Auger emission changes with atomic number, but previous

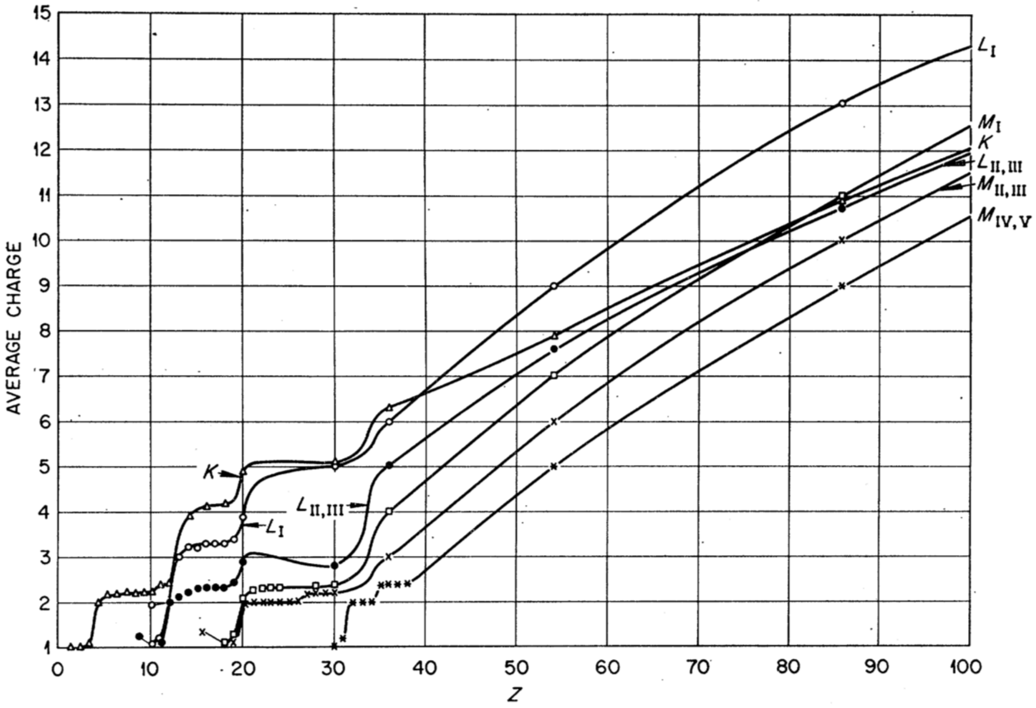

Figure 2.9: Average increase in ionic charge state following the emission of an electron from the K, L_1, $L_{2,3}$, M_1, $M_{2,3}$ and $M_{4,5}$ atomic shells. This figure is taken from ref. [Car66].

studies estimate a width of $\sim 8-10$ charge states in actinide nuclei [Met75, Ulf78].

An alternative method is to simulate the entire atomic relaxation process using theoretical Auger transition probabilities. These are difficult to calculate and the theory will not be covered here. The problem becomes even more complicated when one considers that this is a multistep process and that the atomic configuration will change at each step. They can be calculated using the General Purpose Relativistic Atomic Structure Program (GRASP2K) [Jön13] and Relativistic Atomic Transition and Ionization Properties (RATIP) [Nik06] computer programs. These programs use the relativistic multi-configurational Dirac-Fock (MCDF) method, which can account for higher atomic charge states when the Auger process takes place. In ref. [Lee13] the authors used these codes in Monte Carlo simulations to accurately reproduce experimental charge spectra of $^{131\mathrm{m}}$Xe ions where an Auger cascade is triggered by the emission of an internal conversion electron.

2.6.2 Charge-changing in solid materials

An ion travelling through a solid target may capture or lose electrons upon collisions with the target material, changing the charge state, q, of the ion. For a beam of ions these collisions result in a change in the distribution of ionic charge states. If each ion undergoes many collisions then the fraction of ions in each charge state, $F(q)$, observed after the target, reaches an equilibrium value. As long as the average energy of the ions does not change significantly while passing through the foil, $F(q)$ does not change when the target thickness is increased, and is independent of the initial charge state distribution before the target. An extensive review of charge-changing cross sections for fast heavy ion beams in gaseous and solid materials is given by Betz in ref. [Bet72]. The charge state distribution after the target is Gaussian and the average charge state is defined as,

$$\bar{q} = \sum_{q=0}^{Z} qF(q) \ , \tag{2.46}$$

where q runs over all charge states and Z is the atomic number of the ion beam. The width of the distribution, $d_{\bar{q}}$, is,

$$d_{\bar{q}} = \sqrt{\sum_{q=0}^{Z} (q-\bar{q})^2 F(q)} \ . \tag{2.47}$$

In principle, the values $F(q)$, $\bar{q}$ and $d_{\bar{q}}$ can be calculated theoretically using charge exchange cross sections. However, these are not well understood for fast heavy ions. Instead, empirical formulae can provide accurate estimates for $\bar{q}$ and $d_{\bar{q}}$.

A commonly used formula for estimating $\bar{q}$ and $d_{\bar{q}}$ for heavy ion projectiles ($Z_\mathrm{p} \gtrsim 20$) passing through a solid target foil is set out by Nikolaev and Dimitriev [Nik68],

$$\bar{q} = Z_\mathrm{p}\left[1 + \left(\frac{v}{Z_\mathrm{p}^{\alpha} v'}\right)^{-1/k}\right]^{-k} \ , \tag{2.48}$$

where $k = 0.6$, $\alpha = 0.45$ and $v' = 3.6 \times 10^6$ m/s. The width of the distribution is given as,

$$d_{\bar{q}} = d_0 \sqrt{\bar{q}\left[1 - \left(\frac{\bar{q}}{Z_\mathrm{p}}\right)^{1/k}\right]} \ , \tag{2.49}$$

where $d_0 = 0.5$.

Another more modern formula, developed by Schiwietz and Grande [Sch01], is obtained from a fit to a large set of experimental charge state distributions. The result of the fit is,

$$\bar{q} = Z_\mathrm{p} \frac{12x + x^4}{0.07x^{-1} + 6 + 0.3x^{0.5} 10.37x + x^4} \ , \tag{2.50}$$

where,

$$x = \left(\frac{v_\mathrm{p} Z_\mathrm{p}^{-0.52} Z_\mathrm{t}^{-0.019 Z_\mathrm{p}^{-0.52} v_\mathrm{p}/v_0}}{1.68 v_0} \right)^{1+1.8/Z_\mathrm{p}} \ , \tag{2.51}$$

and v_p is the velocity of the projectile ions, Z_t is the atomic number of the target atoms and $v_0 = 2.19 \times 10^6$ m/s is the Bohr velocity. The width of distribution is given by,

$$d_{\bar{q}} = \frac{w}{Z_\mathrm{p}^{-0.27} Z_\mathrm{t}^{0.035-0.0009Z_\mathrm{p}} f(\bar{q}) f(Z_\mathrm{p} - \bar{q})} \ , \tag{2.52}$$

where,

$$f(x) = \sqrt{1 + 0.37 \frac{Z_\mathrm{p}^{0.6}}{x}} \ , \tag{2.53}$$

and the reduced width parameter, w, varies between 0.6-0.9 (see ref. [Sch01]). The relative uncertainty of the Schiwietz and Grande formula compared to the entire experimental data set (850 data points) is $\Delta\bar{q}/Z_\mathrm{p} = 2.3\%$. In comparison, the relative uncertainty of the Nikolaev and Dimitriev formula, when applied only to ions with $Z_\mathrm{p} > 10$ and $Z_t = 6$, is given as $\Delta\bar{q}/Z_\mathrm{p} = 3.3\%$. Both formulae provide good estimates of the charge state distribution of ions passing through a solid target.

In this work, a beam ^{178}Pt ions were passed through a nickel charge reset foil. Using the Schiwietz and Grande formula, an average charge state of $\bar{q}$ =16.3 e with $d_{\bar{q}} = 1.8$-$2.8e$ for $w = 0.6$-0.9 is expected. These values compare well to the experimental data, described in section 5.5, which give $\bar{q}$ =16.4(1) e and $d_{\bar{q}} = 2.30(9)\,e$.

Chapter 3

Charge Plunger Method

The charge plunger method was developed in the 1970s as a way of measuring the lifetime of states that de-excite predominantly through transitions with high internal conversion coefficients [Ulf78]. The method relies on the large increase in ionic charge state following internal conversion due to the ensuing Auger cascade. The charge plunger method has not been used regularly, due to experimental difficulties that can be more easily overcome using the RDDS technique. For example, the experimental setup in ref. [Ulf78] is not suitable for lifetime measurements in nuclei with low production cross sections. However, more recently the charge plunger technique has been performed using a recoil separator which has high background suppression and allows the method to be used for nuclei produced in fusion-evaporation reactions with low cross sections [Bar20b, Hee21].

In this chapter the analysis tools of conventional RDDS plunger measurements are introduced in section 3.1. The basic concept of the charge plunger method is described in section 3.2 and the DDCM and Bateman analysis techniques applied to charge plunger data are then discussed in sections 3.3 and 3.4, respectively.

3.1 Recoil distance Doppler-shift measurements

A typical recoil distance Doppler-shift (RDDS) setup employs a movable stopper foil placed a distance x after a target to make lifetime measurements in the ps-ns range. Beam ions incident upon the target populate the nuclear level of interest via nuclear reactions such as fusion-evaporation or Coulomb-excitation, for example. This excited state will then de-excite via either γ-ray emission or internal conversion. Nuclei recoil out of the target with a velocity

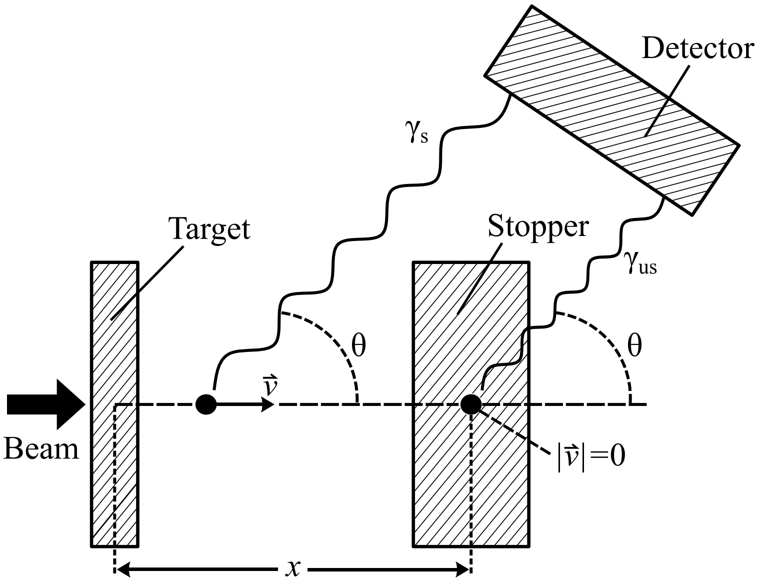

Figure 3.1: Schematic diagram of a plunger setup for the recoil distance Doppler-shift method. The stopper foil is placed at a distance x downstream of the target. Excited states are populated by nuclear reaction between beam and target nuclei. Recoils travel out of the target with a velocity $\vec{v}$ towards the stopper foil where they are brought to rest. The flight time between the target and the stopper foil is $t = x/|\vec{v}|$. A detector is placed at an angle θ to the beam axis. Depending on whether a γ ray is emitted in flight or not, the energy registered by the detector will be Doppler shifted according to equation 3.1. This figure has been adapted from ref. [Dew12].

$\vec{v}$ ($|\vec{v}| = v$) towards the stopper foil where they are brought to rest after a flight time $t = x/v$. This setup is shown schematically in fig. 3.1. By employing the stopper foil after the target two velocity regimes are created. If a recoil emits a γ ray whilst in-flight (i.e. before the recoil has reached the stopper foil), then the energy of the γ ray that is detected in the laboratory frame will be Doppler shifted. The amount by which the energy is Doppler shifted is given by,

$$E = E_0 \frac{\sqrt{1-\beta^2}}{1-\beta\cos(\theta)} \ , \tag{3.1}$$

where E is the energy of the γ ray detected in the laboratory frame, E_0 is the energy of the γ ray in the rest frame of the recoil, $\beta = v/c$ and θ is the angle between the beam axis and the direction the γ ray is travelling. The spectrum of γ-ray energies will include two components, a shifted component corresponding to decays in flight (I_s) and an unshifted component corresponding to decays at rest in the stopper foil (I_{us}). For a given flight time t, the intensity of shifted and unshifted components are dependent on the lifetime of the excited state τ. The decay curve of a state is defined as the normalised intensity of de-excitations occurring after the recoil has come to rest in the stopper foil as a function of time, t. Experimentally this is given as,

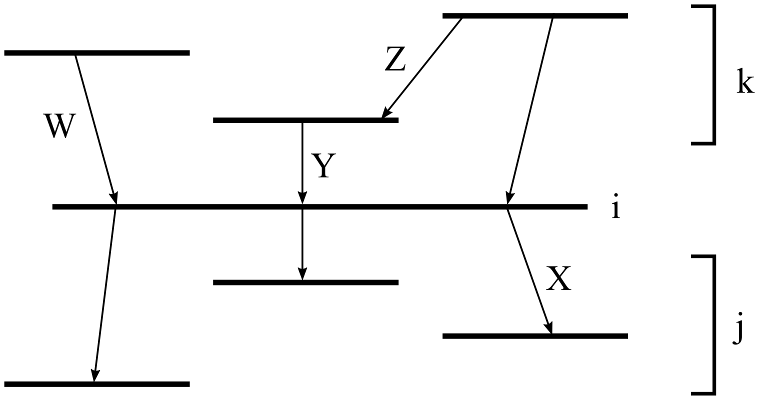

Figure 3.2: General level scheme of excited states. The levels denoted k feed the level of interest i, which in turn depopulates to the states denoted j. The transitions Y and W are direct feeders to i whilst Z is an indirect feeder. This figure has been adapted from ref. [Dew12].

$$R(t) = \frac{I_{\mathrm{us}}(t)}{I_{\mathrm{s}}(t) + I_{\mathrm{us}}(t)} \quad . \tag{3.2}$$

The setup shown in fig. 3.1 is often modified to replace the stopper foil with a thinner degrader foil, which acts to slow down the recoil but not stop it completely. There are two advantages to this. Firstly, the thinner degrader foil avoids the long slowing down time that is required when using a stopper foil [Eml84]. Secondly, the recoils can then be separated downstream of the degrader foil using an electromagnetic spectrometer and detected using solid-state detectors [Tay13b]. This allows for the nuclear species of the recoil to be identified, and timing techniques can be used to tag γ rays that correspond to a particular nucleus [Pau95]. This technique is particularly useful for nuclei that are produced with low cross sections in fusion-evaporation experiments.

3.1.1 Bateman analysis

In a Bateman analysis a fit is performed on the decay curve of the state to calculate its lifetime [Dew12]. For the simplest case of an excited state which has no feeding, the decay curve is,

$$R(t) = n(0)e^{-\lambda t} \quad , \tag{3.3}$$

where $n(0)$ is the population of the excited state at $t = 0$ and $\lambda = 1/\tau$ is the transition probability of the state. However, in general a state is fed by one or more higher-energy excited states, as shown in fig. 3.2. In this level scheme, levels are given a number $l \in \mathbb{N}$ to denote the order of their excitation energy. The level of interest i is fed by levels k and depopulates to levels j, such that $j < i < k$. The decay curve of the level of interest is dependent not only on the lifetime of the level of interest, i, but also on the lifetime of all the feeding states, k, and is found by solving the system of differential equations (Bateman equations) that govern the time dynamics of the decay [Dew12, Thi14, Bat08]. The change in the population of i at time t is given by,

$$\frac{\mathrm{d}}{\mathrm{dt}} n_i(t) = -\lambda_i n_i(t) + \sum_{k=i+1}^{N} \lambda_k n_k(t) b_{ki} \ , \tag{3.4}$$

where N is the highest feeding level considered, $n_{i(k)}(t)$ is the number of nuclei in level $i(k)$ at time t, λ_i, λ_k are the transition probabilities for level i and k and b_{ki} are the branching ratios for the transition $k \to i$. The branching ratios are defined such that $b_{ki} = I_{ki}/I_k$, where I_{ki} is the intensity of $k \to i$ transitions and I_k is the total intensity of all transitions depopulating k. Using this definition $\sum_{i(i<k)} b_{ki} = 1$. The solution to equation 3.4 with respect to the decay curve is,

$$R_i(t) = P_i e^{-\lambda_i t} + \sum_{k=i+1}^{N} M_{ki} \left[\frac{\lambda_i}{\lambda_k} e^{-\lambda_k t} - e^{-\lambda_i t} \right] \ , \tag{3.5}$$

where the value P_i is the direct feeding intensity of level i [Dew12]. The value M_{ki} is defined by,

$$M_{ki} \left(\frac{\lambda_i}{\lambda_k} - 1 \right) = b_{ki} P_k - b_{ki} \sum_{m=k+1}^{N} M_{mk} + \sum_{m=i+1}^{k-1} M_{km} b_{mi} \left(\frac{\lambda_m}{\lambda_k} \right) \ , \tag{3.6}$$

where P_k is the direct feeding intensity of level k. The function $R_i(t)$ is fitted to experimental data to obtain the lifetime τ_i. This fit in general contains a large number of free parameters including level lifetimes, branching ratios, and initial populations, and a good understanding of the level scheme is needed to obtain an accurate value for the lifetime. The fit is dependent on absolute distances and so the $x = 0$ point must also be determined.

A problem arises from side-feeding, in which a level is fed by non-discrete statistical transitions. The intensity of this side-feeding can be calculated by comparing the observed population and de-population intensities from the level of interest. The side-feeding times can be estimated by using either a statistical model [Pas00] or by making the assumption that the unobserved feeding time is equal to the average observed feeding time. This assumption has been verified from experiment [Har87].

3.1.2 Differential decay curve method

The differential decay curve method (DDCM) provides an alternative method for performing lifetime measurements on RDDS data [Dew12, Dew89, Böh93]. There are advantages to using the DDCM over a Bateman analysis. In the DDCM only experimentally accessible variables are used. This differs to the Bateman analysis where unknown parameters have to be kept free in a fit. For this reason the DDCM offers a way of measuring the lifetime of a level independent of the lifetime of other states in the level scheme. Secondly, the method requires only relative target-to-stopper foil distances instead of absolute values. This is a particular advantage when the separation between foils is small and the error on the measurement of the $x = 0$ point becomes significant.

The DDCM can be performed using either γ-ray singles or coincidence analysis. An advantage of using γ-γ coincidences is that it provides a way to overcome the problem of side-feeding [War73]. It does, however, result in lower statistics and so longer measurement times must be used to obtain necessary statistics.

Singles analysis

By integrating equation 3.4 one obtains,

$$n_i(\infty) - n_i(t) = -N_i(t) + \sum_{k=i+1}^{N} b_{ki} N_k(t) \ , \tag{3.7}$$

where the identity,

$$N_i(t) = \lambda_i \int_t^{\infty} n_i(t) dt \ , \tag{3.8}$$

has been used. For a state with a finite lifetime $n_i(\infty) = 0$, and $\frac{\mathrm{d}}{\mathrm{dt}} N_i(t) = -\lambda_i n_i(t)$. Using the relation $x = v \cdot t$ to transform from the flight time of the recoil between the target and the stopper foil to the separation distance between the two foils, x, one obtains,

$$\tau_i(x) = \frac{-R_{ij}(x) + b_{ij} \sum_k \frac{J_{ki}}{J_{ij}} R_{ki}(x)}{\frac{\mathrm{d}}{\mathrm{dx}} R_{ij}(x)} \frac{1}{v} \ , \tag{3.9}$$

where $R_i(x) = N_i(x)/N_i(0)$, J_{ki} and J_{ij} are the relative intensities of the γ transitions $k \rightarrow i$

and $i \to j$ respectively, and $R_{ij}(t) = b_{ij}R_i(t)$. The decay curve, $R_{ij}(x)$, is found experimentally from equation 3.2, where the subscript refers specifically to the transition $i \to j$. For each experimental measurement of the decay curves $R_{ij}(x)$ and $R_{ki}(x)$, a value for the lifetime $\tau_i(x)$ can be obtained. The measured lifetime is then the mean value of the lifetime obtained at each point on the decay curve, $\tau_i = \langle \tau_i(x) \rangle$.

Coincidence analysis

Consider again the level scheme in fig. 3.2. The transition Y is a direct feeder to the level of interest, whilst transition Z is an indirect feeder. If a gating condition is set to only observe transitions that are temporally coincident with a shifted component of the feeding transition Y, then all dependence on the time dynamics of previous de-excitations is destroyed. The contamination from unobserved side-feeding or observed feeding from other transitions (e.g. W) is also removed.

The lifetime of level i, when a coincidence gate condition is set on a direct feeder transition, e.g. Y, is given by,

$$\tau_i(x) = \frac{\{Y_s, X_{us}\}(x)}{\frac{\mathrm{d}}{\mathrm{dx}}\{Y_s, X_s\}(x)} \frac{1}{v} \ , \tag{3.10}$$

where the notation $\{Y, X\}(x)$ describes the intensity of X γ-ray emissions that are in coincidence with a detected Y γ ray. The s and us subscripts refer to whether the γ ray is Doppler-shifted or unshifted respectively. A change of coordinates has been performed to transfer from the flight time of the recoil between the target and the stopper foil to the separation distance between the two foils, x. The equation is modified if the coincidence gate is set on an indirect feeding transition e.g. Z,

$$\tau_i(x) = \frac{\{Z_s, X_{us}\}(x) - \xi\{Z_s, Y_{us}\}(x)}{\frac{\mathrm{d}}{\mathrm{dx}}\{Z_s, X_s\}(x)} \frac{1}{v} \ , \tag{3.11}$$

where $\xi = \langle \xi(x) \rangle_x$ is the mean value of $\xi(x)$ where,

$$\xi(x) = \frac{\{Z_s, X_{us}\}(x) + \{Z_s, X_s\}(x)}{\{Z_s, Y_{us}\}(x) + \{Z_s, Y_s\}(x)} \ . \tag{3.12}$$

corrects for differences in the measured intensities of the populating and depopulating transitions [Dew12]. The lifetime of the state is then given by the mean value of the lifetime measured at each target-to-stopper distance, $\tau_i = \langle \tau_i(x) \rangle$.

3.2 Basics of the charge plunger method

The difference between the RDDS technique and the charge plunger method is the observation of the de-excitation of a nuclear state. In the RDDS method, the de-excitation is directly observed through the emission of a γ ray, whereas in the charge plunger method the de-excitation of a state by internal conversion is inferred from a change in the distribution of charge states. As described in sections 2.3.2 and 2.6.1, an internal conversion creates a vacancy in an atomic shell which is then filled as electrons cascade down the atomic levels. This cascade of atomic electrons causes Auger electrons to be emitted from the atom and the charge state of the ion is significantly increased. The nuclear de-excitation therefore indirectly causes changes in the atomic structure which are then observed and used to infer the de-excitation.

The setup for a charge plunger experiment is similar to the RDDS technique, shown in fig. 3.1. However, the stopper foil is replaced with a thin charge reset foil, which recoils travel through and are detected afterwards. Consider a simple example of a nucleus with one excited state. The excited state is populated by nuclear reactions of the beam and target nuclei and de-excites down to the ground state via γ-ray emission or internal conversion. Recoils leave the target with a velocity, $\vec{v}$ ($|\vec{v}| = v$), and travel towards the charge reset foil, which is placed a distance x downstream of the target. After passing through the charge reset foil the ionic charge state of the recoiling nuclei will have a Gaussian charge distribution with a centroid value that is dependent on the recoils' velocity (see section 2.6.2). The setup is demonstrated in fig. 3.3. There are three possible scenarios:

(i) The level de-excites by either γ-ray emission or internal conversion before the ion exits the charge reset foil. The ionic charge state is then reset when the recoil passes through the foil.

(ii) The de-excitation occurs after the charge reset foil and proceeds via γ-ray emission which leaves the ionic charge state unchanged.

(ii) The de-excitation occurs after the charge reset foil and proceeds via the emission of an internal conversion electron. The ensuing Auger cascade causes the emission of more atomic electrons and increases the ionic charge state.

There will be two components in the charge-state distribution (CSD) of ions after the reset foil. A low charge component (Q_L) due to scenarios (i) and (ii), and a high charge component (Q_H) due to scenario (iii). The intensities of these two components (I_L and I_H) are given by,

$$I_H(x) = P_{\text{ic}} I_A(x) \ , \tag{3.13}$$

$$I_L(x) = I_B(x) + P_\gamma I_A(x) \ , \tag{3.14}$$

where I_A and I_B are the intensity of transitions that occur after and before the reset foil respectively and and $P_{\text{ic}(\gamma)}$ is the probability that the transition proceeds by internal conversion

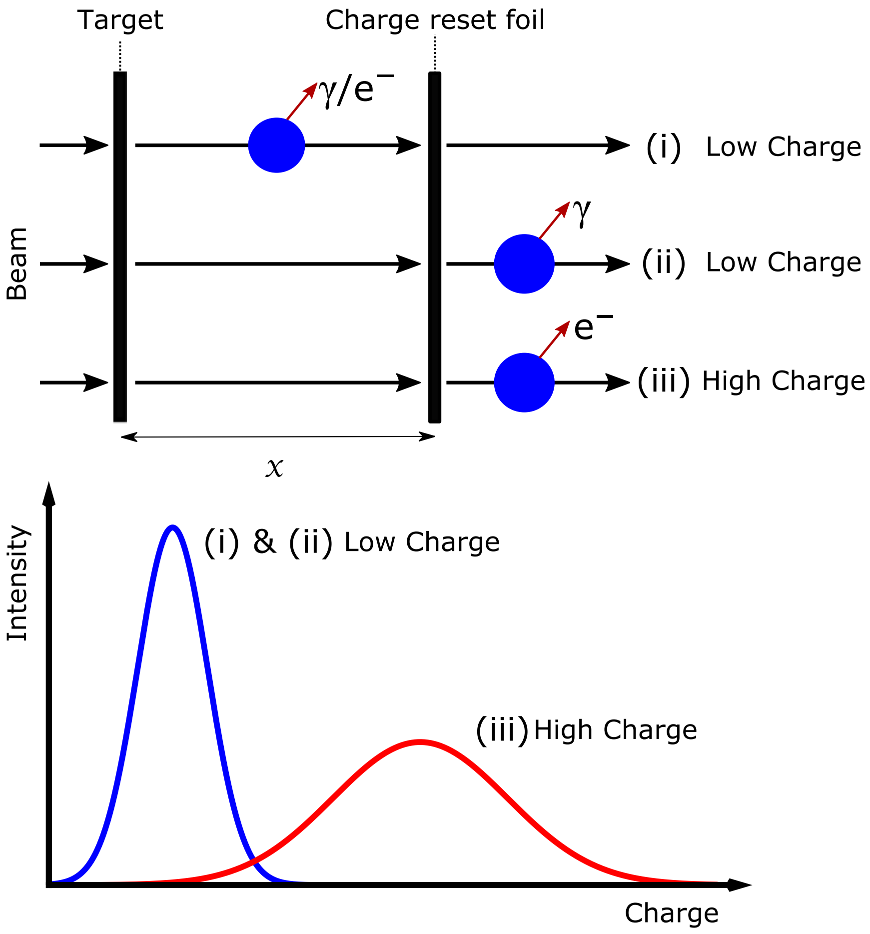

Figure 3.3: Schematic diagram of the charge plunger method (upper). An internal conversion and subsequent Auger cascade will cause the ionic charge to increase. If the transition occurs before the reset foil, the ionic charge state will be reset. If the transition occurs after the reset foil, the ion remains in a high charge state. A γ-ray transition does not create a vacancy in the atomic shell configuration and therefore does not affect the charge state of the ion. The charge-state distribution after the plunger foil will therefore contain two components (lower).

(γ-ray emission). Therefore it is possible to transform from the experimental observables, I_H and I_L, to quantities that are relevant to the de-excitation of the state, I_A and I_B, given by,

$$I_A(x) = \left(\frac{1+\alpha}{\alpha}\right) I_H(x) \ , \tag{3.15}$$

$$I_B(x) = I_L(x) - \frac{I_H(x)}{\alpha} \ , \tag{3.16}$$

where the internal conversion coefficient α is given by,

$$\alpha = \frac{P_{\text{ic}}}{P_\gamma} \ . \tag{3.17}$$

The decay curve of the excited state, which reflects the probability of a transition occurring after a time $t = x/v$, is given by,

$$R(t) = \frac{I_A(t)}{I_B(t) + I_A(t)} = \left(\frac{1+\alpha}{\alpha}\right) \frac{I_H(t)}{I_L(t) + I_H(t)} \ , \tag{3.18}$$

and depends on four variables; the average recoil velocity after the target, v, the target-to-reset foil distance, x, the internal conversion coefficient for the transition, α, and the lifetime of the excited state, τ. If the first three variables are known then it is possible to obtain the lifetime of the state.

3.2.1 Multiple high charge components

The situation becomes harder when a more realistic nuclear level scheme, shown in fig. 3.4a, is considered. There are now multiple internal conversion electrons that can be emitted after the reset foil. Each of these conversions will be succeeded by an Auger cascade and will result in multiple high charge components in the CSD as shown in fig. 3.4b. The different components of the CSD will be referred to as Q_L, Q_H, Q_{2H}, Q_{3H}, etc. (with intensities I_L, I_H, I_{2H}, I_{3H}, etc.) for the remainder of the work. Ions have a finite number of electrons, so for low-Z nuclei the effect of multiple internal conversions on the CSD will be more complicated. However, here we consider only nuclei for which the Auger emission process is not significantly altered by the fact that the ion is already positively charged.

Another problem arises due to the fact that nuclear de-excitations are only inferred from the CSD and are not directly observed. Consider the decay paths *CBA*, *DBA* and *GBA*. It will be assumed that each transition proceeds by internal conversion after the charge reset foil. Each decay path will populate the Q_{3H} component of the CSD, therefore making the decay paths indistinguishable from each other. The problem is compounded when one considers the decay path $FEBA$, where three of the transitions proceed by internal conversion and the other proceeds by γ-ray emission. This path will again cause an ion to populate the Q_{3H} component, making it indistinguishable from the three previous decay paths. The transitions may cause internal conversion electrons to be emitted from different atomic shells, which changes the average number of Auger electrons emitted from the atom (see fig. 2.9). However, these changes will be very small when compared with the width of the distribution [Ulf78].

The indistinguishability of different decay paths has consequences for a DDCM singles analysis. Equation 3.9 shows that it is necessary to know the intensity of all transitions feeding the level of interest. However, it is impossible to obtain this information for the level i in fig. 3.4a from the CSD without knowledge of the internal conversion of each feeding transition and the lifetime of the state it depopulates. Therefore, in general, the charge plunger method cannot be combined with the DDCM singles analysis to perform lifetime measurements.

Due to the difficulty in analysing a level scheme such as that shown in fig. 3.4a, for the remainder of this chapter a simple rotational band built upon the ground state will be considered, as shown in fig. 3.5. The notation used in the previous section describing the RDDS

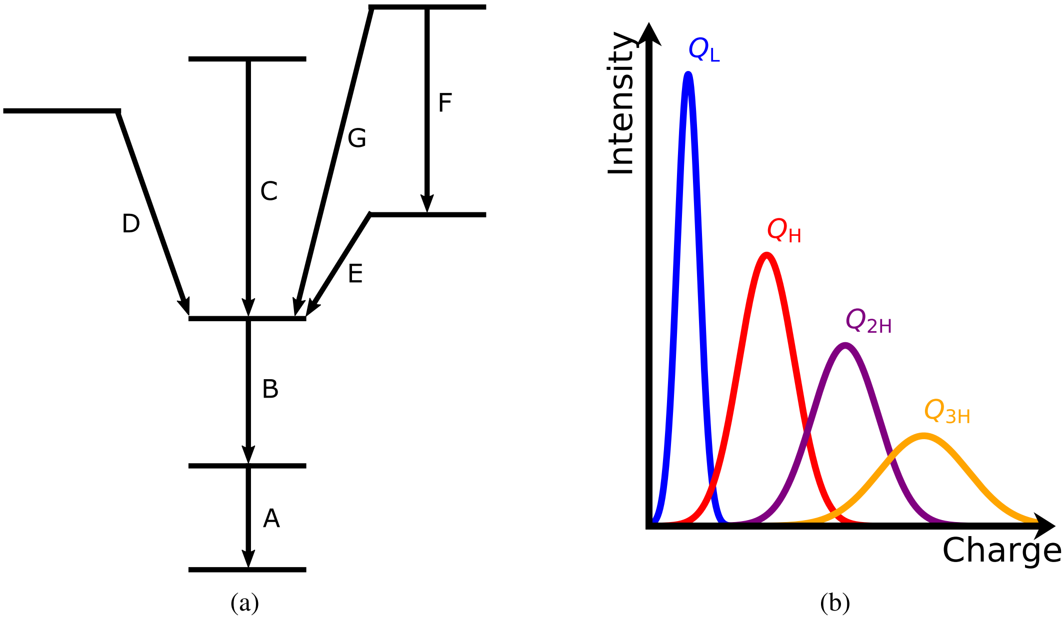

(a) (b)

Figure 3.4: (a) General level scheme. The transitions between states are labelled *A*, *B*, *C*, *D*, *E*, *F* and *G*. (b) The CSD will now contain higher charge components due to multiple internal conversions after the reset foil.

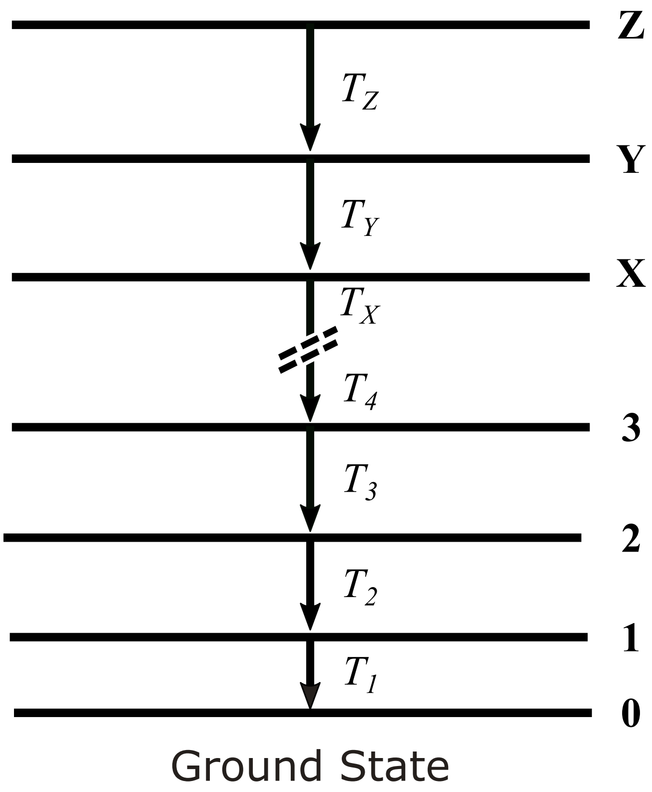

Figure 3.5: Example rotational band level scheme. Excited levels, i, are populated by a transition T_{i+1} from the level $i+1$, and depopulate via transitions T_i to the level $i-1$.

method is now discarded and a more suitable notation is adopted. Levels are once again denoted by a number $l \in \mathbb{N}$ which describes their order in excitation energy. Consecutive levels $l-1$ and l are connected by a transition T_l, which proceeds by either γ-ray emission or internal conversion. The ground state of the band is given the index $l = 0$, whilst the highest level considered is $l = Z$, such that the order of the levels is $l = 0, 1, 2, ..., X, Y, Z$. The level indexing is slightly different in this thesis to that in ref. [Hee21]. There, the highest levels in the rotational band were labelled M and N instead of X, Y and Z. The indexing has been changed here as the mathematical description of the charge plunger analysis methods are covered in more detail and the X, Y, Z notation may offer less confusion in some of the equations.

3.3 Applying a DDCM coincidence analysis to the charge plunger method

As shown in refs. [Bar20b, Hee21], a DDCM coincidence analysis can be combined with the charge plunger method to perform lifetime measurements on low-lying excited states in a nucleus. The authors used a coincidence gate on a feeding transition to the level of interest, and detected recoils, separated by ionic charge state, after the charge reset foil.

In section 3.1.2, the DDCM coincidence equations were defined in terms of the intensity of shifted (I_s) and unshifted (I_us) components of the γ-ray energy spectrum. This notation is not suitable in the charge plunger method for two reasons. Firstly, recoils are not stopped in the charge reset foil and therefore the γ-ray emission of the feeding transition to which a coincidence gate is applied (gating transition) will have a full-shifted (I_fs) and a degraded (I_de) component in the γ-ray energy spectrum corresponding to the transition occurring before or after the reset foil respectively. Secondly, the intensity of the transition depopulating the level of interest (analysing transition) is determined from analysing the intensities of charge components in the CSD. In this section, the DDCM coincidence equations will be defined again using a more suitable notation.

Consider the rotational band level scheme shown in fig. 3.5. The lifetime of level Y is given by,

$$\tau_Y(x) = \frac{\{Z_\mathrm{fs}, Y_A\}(x)}{\frac{\mathrm{d}}{\mathrm{dx}}\{Z_\mathrm{fs}, Y_B\}(x)} \cdot \frac{1}{v} \ , \tag{3.19}$$

where $\{Z, Y\}(x)$ is the number of T_Y transitions that are in coincidence with a measured γ ray from the direct feeding T_Z transition. The subscript fs indicates that the gating transition is detected in the fully shifted component of the γ-ray energy spectrum. The subscripts B and A refer to the analysing transition occurring before or after the reset foil, respectively. If instead the level of interest is $l = X$, according to equation 3.11, the lifetime of level X is given by,

$$\tau_X(x) = \frac{\{Z_\mathrm{fs}, X_A\}(x) - \xi\{Z_\mathrm{fs}, Y_A\}(x)}{\frac{\mathrm{d}}{\mathrm{dx}}\{Z_\mathrm{fs}, X_B\}(x)} \frac{1}{v} \ , \tag{3.20}$$

where the factor ξ, which corrects for differences in the measured intensities of the populating and depopulating transitions, will be unity. This is because intensities are measured from the CSD rather than the γ-ray energy spectrum and the efficiency of measuring T_Y and T_X transitions has no dependence on the energy of the transition. Using the identities,

$$\{Z_\mathrm{fs}, X_A\}(x) = \{Z_\mathrm{fs}, Y_B, X_A\}(x) + \{Z_\mathrm{fs}, Y_A\}(x) \ , \tag{3.21}$$

and,

$$\{Z_{\mathrm{fs}},Y_B\}(x) = \{Z_{\mathrm{fs}},Y_B,X_A\}(x) + \{Z_{\mathrm{fs}},X_B\}(x) \ , \tag{3.22}$$

equation 3.20 can be rewritten as,

$$\tau_X(x) = \frac{\{Z_{\mathrm{fs}},Y_B,X_A\}(x)}{\frac{\mathrm{d}}{\mathrm{dx}}\left(\{Z_{\mathrm{fs}},Y_B\}(x) - \{Z_{\mathrm{fs}},Y_B,X_A\}(x)\right)}\frac{1}{v} \ , \tag{3.23}$$

where the notation $\{Z_{\mathrm{fs}},Y_B,X_A\}$ implies that a coincidence gate is set on fully shifted T_Z γ-ray emissions, the coincident T_Y transitions also occur before the reset foil, and the coincident T_X transitions occur after the reset foil. In cases where the notation for a transition occurring before or after the reset foil is implied by that of a previous or subsequent transition, the notation is shortened to contain only the necessary information. For example, $\{Z_{\mathrm{fs}},Y_A,X_A\} \equiv \{Z_{\mathrm{fs}},Y_A\}$ and $\{Z_{\mathrm{fs}},Y_B,X_B\} \equiv \{Z_{\mathrm{fs}},X_B\}$.

The next paragraphs show how the quantities in equations 3.19 and 3.23 can be derived from the intensities of components in the CSD, when a coincidence gate is set on the transitions T_2, T_3 and T_Z shown in fig. 3.5.

Coincidence gate: T_2

For the case where a coincidence gate is set on fully-shifted T_2 transitions, only T_1 transitions can occur after the reset foil and there will be two components present in the CSD, Q_L and Q_H. This situation is exactly the same as the simple case of a nucleus with one excited state presented at the beginning of this section. The intensities of T_1 transitions occurring after and before the foil is therefore given by,

$$\{2_{\mathrm{fs}},1_A\}(x) = \left(\frac{1+\alpha_1}{\alpha_1}\right)\{2_{\mathrm{fs}},H\}(x) \ , \tag{3.24}$$

$$\{2_{\mathrm{fs}},1_B\}(x) = \{2_{\mathrm{fs}},L\}(x) - \frac{\{2_{\mathrm{fs}},H\}(x)}{\alpha_1} \ , \tag{3.25}$$

where $\{2_{\mathrm{fs}},H(L)\}(x)$ is the intensity of ions detected in Q_H (Q_L) that are in coincidence with a measured fully shifted γ ray from the T_2 transition and α_1 is the internal conversion coefficient of transition T_1. By measuring the charge state of ions in coincidence with fully shifted T_2 transitions, the equations 3.24 and 3.25 can be used together with equation 3.19 to find the lifetime of level 1.

Coincidence gate: T_3

When a gate is placed on fully-shifted T_3 transitions, there are now two transitions that can occur after the reset foil, T_2 and T_1. This means a second-high charge component, Q_{2H}, will also be present in the CSD. The possible combinations of γ-ray transitions and internal conversions that can occur after the reset foil are shown in fig. 3.6. The intensities of the charge components Q_L, Q_H and Q_{2H} are given by,

$$\{3_{\text{fs}}, 2H\}(x) = P_{2,\text{ic}}\, P_{1,\text{ic}}\, \{3_{\text{fs}}, 2_A\}(x) \ , \tag{3.26}$$

$$\{3_{\text{fs}}, H\}(x) = P_{1,\text{ic}}\, \{3_{\text{fs}}, 2_B, 1_A\}(x) + [P_{2,\text{ic}}\, P_{1,\gamma} + P_{2,\gamma} P_{1,\text{ic}}]\, \{3_{\text{fs}}, 2_A\}(x) \ , \tag{3.27}$$

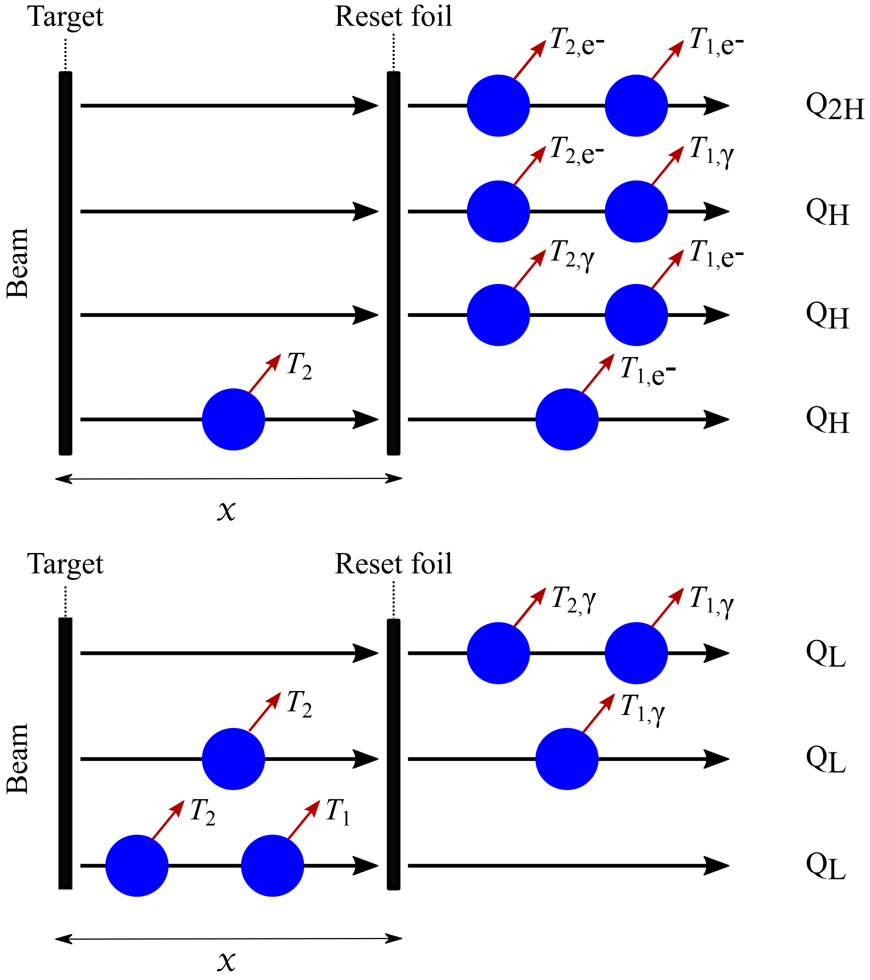

Figure 3.6: Schematic diagram to show the possible combinations that make up the different components in the CSD when there are two transitions that can occur after the reset foil.

$$\{3_{\mathrm{fs}}, L\}(x) = \{3_{\mathrm{fs}}, 1_B\}(x) + P_{1,\gamma}\{3_{\mathrm{fs}}, 2_B, 1_A\}(x) + P_{2,\gamma}P_{1,\gamma}\{3_{\mathrm{fs}}, 2_A\}(x) \ . \tag{3.28}$$

Using equation 3.26 an expression for the number of T_2 transitions occurring after the reset foil is given by,

$$\{3_{\mathrm{fs}}, 2_A\}(x) = \left(\frac{1+\alpha_2}{\alpha_2}\right)\left(\frac{1+\alpha_1}{\alpha_1}\right)\{3_{\mathrm{fs}}, 2H\} \ . \tag{3.29}$$

The number of T_2 transitions occurring before the foil is more difficult to obtain. The equations 3.27 and 3.28 are rearranged to collect expressions for transition T_2 occurring before the reset foil,

$$P_{1,\mathrm{ic}}\{3_{\mathrm{fs}}, 2_B, 1_A\}(x) = \{3_{\mathrm{fs}}, H\}(x) - [P_{2,\mathrm{ic}}P_{1,\gamma} + P_{2,\gamma}P_{1,\mathrm{ic}}]\{3_{\mathrm{fs}}, 2_A\}(x) \ , \tag{3.30}$$

$$\{3_{\mathrm{fs}}, 1_B\}(x) + P_{1,\gamma}\{3_{\mathrm{fs}}, 2_B, 1_A\}(x) = \{3_{\mathrm{fs}}, L\}(x) - P_{2,\gamma}P_{1,\gamma}\{3_{\mathrm{fs}}, 2_A\}(x) \ . \tag{3.31}$$

Using the identity,

$$\{3_{\mathrm{fs}}, 2_B\}(x) = \{3_{\mathrm{fs}}, 1_B\}(x) + P_{1,\gamma}\{3_{\mathrm{fs}}, 2_B, 1_A\}(x) + P_{1,\mathrm{ic}}\{3_{\mathrm{fs}}, 2_B, 1_A\}(x) \ , \tag{3.32}$$

and substituting in the expression for $\{3_{\mathrm{fs}}, 2_A\}(x)$ from equation 3.29, the number of T_2 transitions occurring before the reset foil is given by,

$$\{3_{\mathrm{fs}}, 2_B\}(x) = \{3_{\mathrm{fs}}, L\}(x) + \{3_{\mathrm{fs}}, H\}(x) - \{3_{\mathrm{fs}}, 2H\}(x)\left[\frac{1}{\alpha_1} + \frac{1}{\alpha_2} + \frac{1}{\alpha_2\alpha_1}\right] \ , \tag{3.33}$$

where the terms in the square bracket result from the different combinations of two transitions that can proceed by either γ-ray emission or internal conversion after the reset foil. The equations for $\{3_{\mathrm{fs}}, 2_A\}(x)$ and $\{3_{\mathrm{fs}}, 2_B\}(x)$ can be used together with the DDCM equation for a direct feeding transition (equation 3.19) to find the lifetime of level 2.

For the case where the level of interest is $l = 1$, the DDCM equation for a indirect feeding transition (equation 3.23) requires that the quantity $\{3_{\rm fs},2_B,1_A\}(x)$ is measured. This is found by rearranging $\{3_{\rm fs},H\}(x)$ (equation 3.27) and substituting in the expression for $\{3_{\rm fs},2_A\}(x)$ (equation 3.29),

$$\{3_{\rm fs},2_B,1_A\}(x) = \frac{1+\alpha_1}{\alpha_1}\left[\{3_{\rm fs},H\} - \{3_{\rm fs},2H\}\left(\frac{1}{\alpha_1}+\frac{1}{\alpha_2}\right)\right] \ . \tag{3.34}$$

Coincidence gate: T_Z

The notation can be expanded for a coincidence gate set on any transition shown in fig 3.5. If a gate is set on the fully shifted component of transition T_Z there are Y transitions that can occur after the reset foil, each proceeding by either internal conversion or γ-ray emission. There will therefore be Y high-charge components in the CSD. The intensities of the charge components in the CSD are given by,

$$\{Z_{\rm fs},YH\} = \left(\prod_{i=1}^{Y} P_{i,ic}\right)\{Z_{\rm fs},Y_A\} \ , \tag{3.35}$$

$$\{Z_{\rm fs},XH\} = \sum_{j=1}^{Y}\left(P_{j,\gamma}\prod_{i=1,i\neq j}^{Y} P_{i,ic}\right)\{Z_{\rm fs},Y_A\} + \left(\prod_{i=1}^{Y-1\equiv X} P_{i,ic}\right)\{Z_{\rm fs},Y_B,X_A\} \ , \tag{3.36}$$

...

$$\{Z_{\rm fs},2H\} = \sum_{j=1}^{X}\sum_{k=j+1}^{Y}\left(P_{j,ic}P_{k,ic}\prod_{i=1,i\neq j,k}^{Y} P_{i,\gamma}\right)\{Z_{\rm fs},Y_A\} + ... + P_{2,ic}P_{1,ic}\{Z_{\rm fs},3_B,2_A\} \ , \tag{3.37}$$

$$\{Z_{\rm fs},H\} = \sum_{j=1}^{Y}\left(P_{j,ic}\prod_{i=1,i\neq j}^{Y} P_{i,\gamma}\right)\{Z_{\rm fs},Y_A\} + ... + P_{1,ic}\{Z_{\rm fs},2_B,1_A\} \ , \tag{3.38}$$

$$\{Z_{\rm fs},L\} = \left(\prod_{i=1}^{Y} P_{i,\gamma}\right)\{Z_{\rm fs},Y_A\} + ... + P_{1,\gamma}\{Z_{\rm fs},2_B,1_A\} + \{Z_{\rm fs},1_B\} \ . \tag{3.39}$$

By rearranging the above equations in a similar manner to that done in the previous cases, the number of T_Y transitions occurring after or before the foil are given by,

$$\{Z_{\rm fs},Y_A\}(x) = \left(\prod_{i=1}^{Y}\frac{1+\alpha_i}{\alpha_i}\right)\{Z_{\rm fs},YH\}(x) \ , \tag{3.40}$$

$$\{Z_{\text{fs}},Y_B\} = \{Z_{\text{fs}},L\}(x) + \left(\sum_{i=1}^{X}\{Z_{\text{fs}},iH\}(x)\right) - \{Z_{\text{fs}},YH\}(x)\left[\sum_{i=1}^{Y} C_i(\alpha_1,\alpha_2,...,\alpha_Y)\right] \ , \tag{3.41}$$

where the function $C_i(\alpha_1,\alpha_2,...,\alpha_Y)$ is defined as,

$$\begin{aligned}
C_1(\alpha_1,\alpha_2,...,\alpha_Y) &= \sum_{j_1=1}^{Y}\frac{1}{\alpha_{j_1}} \ , \\
C_2(\alpha_1,\alpha_2,...,\alpha_Y) &= \sum_{j_1=1}^{Y-1}\ \sum_{j_2=j_1+1}^{Y}\frac{1}{\alpha_{j_1}\alpha_{j_2}} \ , \\
C_i(\alpha_1,\alpha_2,...,\alpha_Y) &= \sum_{j_1=1}^{Y-(i-1)}\ \sum_{j_2=j_1+1}^{Y-(i-2)} ... \sum_{j_i=j_{i-1}+1}^{Y}\left(\prod_{j=j_1}^{j_i}\frac{1}{\alpha_j}\right) \ , \\
C_Y(\alpha_1,\alpha_2,...,\alpha_Y) &= \prod_{j=1}^{Y}\frac{1}{\alpha_j} \ ,
\end{aligned} \tag{3.42}$$

and describes the different combinations of Y transitions that can proceed by either γ-ray emission or internal conversion after the foil. Equations 3.40 and 3.41 can be used to find the lifetime of level Y, τ_Y, when a coincidence gate is placed on the direct feeding transitions, T_Z, occurring before the reset foil.

If instead the level of interest is $l = X$, the DDCM equation for an indirect feeding transition (equation 3.23) requires the quantity $\{Z_{\text{fs}},Y_B,X_A\}(x)$. This is found by rearranging $\{Z_{\text{fs}},XH\}(x)$ (equation 3.36) and substituting in the expression for $\{Z_{\text{fs}},Y_A\}(x)$ (equation 3.40),

$$\{Z_{\text{fs}},Y_B,X_A\}(x) = \left(\prod_{i=1}^{X}\frac{1+\alpha_i}{\alpha_i}\right)\left[\{Z_{\text{fs}},XH\}(x) - \{Z_{\text{fs}},YH\}(x)\left(\sum_{j=1}^{X}\frac{1}{\alpha_j}\right)\right] \ . \tag{3.43}$$

Similarly, if the level of interest is $l = W \equiv X-1$, the DDCM equation for an indirect feeding transition requires the quantity $\{Z_{\text{fs}},X_B,W_A\}(x)$. This is found by rearranging $\{Z_{\text{fs}},WH\}(x)$ and substituting in the expressions for $\{Z_{\text{fs}},Y_A\}(x)$ and $\{Z_{\text{fs}},Y_B,X_A\}(x)$. This process can be repeated for any level in the band. In the above equations it is important to note that for a lifetime measurement of a state where there are Y possible internal conversions occurring after the reset foil, then all Y components of the CSD must be measured.

3.4 Applying a Bateman analysis to the charge plunger method

In section 3.3, experimental observables I_L, I_H, ..., I_{YH} were transformed into physical variables relating to the number of T_1, T_2, ..., T_Y transitions occurring before and after the reset foil that could be used within the DDCM framework to directly obtain the lifetime of the Y^{th} state. However, instead of performing a transformation on the variables, one can fit the experimental observables by modelling the de-excitation of excited states in a nucleus with the Bateman equation.

As in the RDDS method, modelling the decay curve of a state using the Bateman equation requires one to have knowledge of the decay properties of all higher energy excited states. There is an added problem in the charge plunger method that the experimental observables are the intensity of components in the CSD and so the de-excitation of a state cannot be directly observed. The problem can be simplified by considering a rotational level scheme such as that shown in fig. 3.5. As a reminder, levels are denoted by a number $l \in \mathbb{N}$ which describes their order in excitation energy. Consecutive levels $l-1$ and l are connected by a transition T_l, which proceeds by either γ-ray emission or internal conversion. The ground state of the band is given the index $l = 0$, whilst the highest level considered is $l = Z$. The differential equation that describes the change in population of some excited level l at time t, $n_l(t)$ is given by,

$$\frac{\mathrm{d}}{\mathrm{dt}} n_l(t) = -\lambda_l n_l(t) + \lambda_{l+1} n_{l+1}(t) \ , \tag{3.44}$$

where the solution to the set of differential equations for the entire band gives the population of the level l at time t as,

$$n_l(t) = n_l(0) e^{-\lambda_l t} + \sum_{i>l} \left[n_i(0) \cdot \left(\prod_{j=l+1}^{i} \lambda_j \right) \cdot \left(\sum_{j=l}^{i} \left(\frac{e^{-\lambda_j t}}{\prod_{p=l,p\neq j}^{i} (\lambda_p - \lambda_j)} \right) \right) \right] \ , \tag{3.45}$$

where $n_l(0)$ is the initial population of level l, at time $t = 0$ [Bat08].

The quantity $n_l(t)$ is the population of level l at time t. Therefore $n_l(t = x/v)$ represents the probability that all transitions T_i $(i > l)$ occur before the reset foil and all transitions T_j $(j \leq l)$ occur after the reset foil. For the entire rotational band shown in fig. 3.5, the relative intensities of the components in the CSD are given by,

$$I_{ZH}(x) = \left(\prod_{i=1}^{Z} P_{i,ic}\right) n_Z(x) \ , \tag{3.46}$$

$$I_{YH}(x) = \sum_{j=1}^{Z} \left(P_{j,\gamma} \prod_{i=1, i\neq j}^{Z} P_{i,ic}\right) n_Z(x) + \left(\prod_{i=1}^{Y} P_{i,ic}\right) n_Y(x) \ , \tag{3.47}$$

$$...$$

$$I_H(x) = \sum_{j=1}^{Z} \left(P_{j,ic} \prod_{i=1, i\neq j}^{Z} P_{i,\gamma}\right) n_Z(x) + \sum_{j=1}^{Y} \left(P_{j,ic} \prod_{i=1, i\neq j}^{Y} P_{i,\gamma}\right) n_Y(x) + ... + P_{1,ic} n_1(x) \ , \tag{3.48}$$

$$I_L(x) = \left(\prod_{i=1}^{Z} P_{i,\gamma}\right) n_Z(x) + \left(\prod_{i=1}^{Y} P_{i,\gamma}\right) n_Y(x) + ... + P_{1,\gamma} n_1(x) + n_0(x) \ , \tag{3.49}$$

where $n_Z(x) \equiv n_Z(t = x/v)$. The quantity $n_0(x) = 1 - \sum_{i=1}^{Z} n_i(x)$, represents the probability that transition T_1 (and therefore all previous transitions) occurs before the reset foil. The equations above can be simultaneously fitted to the experimental values for I_{ZH}, ..., I_H and I_L using the parameters, P_Z, ..., P_1, α_Z, ..., α_1, λ_Z, ..., λ_1.

In order to fit the experimental intensities to a rotational band with Z levels, the number of free parameters is $3Z$, which will result in a significant uncertainty in the obtained lifetime value for the level of interest. It is usually the case that the internal conversion coefficient for the each transition can be fixed using e.g. the BrIcc database [Kib08], and the number of free parameters can be reduced to $2Z$. The next subsection (3.4.1) shows how one can further reduce the number of parameters that are required to measure the lifetime of the first excited state (level 1) in the rotational band by (i) assuming a two-level band and (ii) assuming a rigid-rotor model for the nucleus.

3.4.1 Reducing the number of free parameters in a Bateman fit

Two level rotational band

The whole rotational band can be simplified to a band with only two excited states as shown in fig. 3.7. The second excited level (2_{av}) in the simplified band is then modelled as a state whose properties represent an average of the levels 2, 3, ..., Z in the full rotational band. The decay probability $\lambda_{2\mathrm{av}}$ represents the average depopulation of the levels 2, 3, ..., Z to level 1 (the first excited state), and the value of $P_{2\mathrm{av,ic}}$ represents the average probability for the

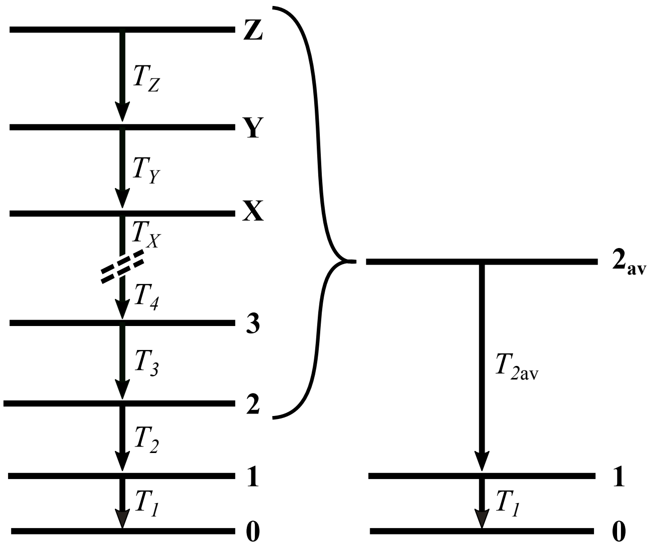

Figure 3.7: The rotational band with Z excited levels is simplified to one with only two excited levels. The properties of the second excited level in the simplified band is an average of the levels $2-Z$ in the whole band.

transitions T_2, T_3, ..., T_Z to undergo internal conversion.

According to equation 3.45 the population of the two excited levels are,

$$n_{2\text{av}}(t) = n_{2\text{av}}(0)e^{-\lambda_{2\text{av}}t} \ , \tag{3.50}$$

$$n_1(t) = n_1(0)e^{-\lambda_1 t} + n_{2\text{av}}(0)\frac{\lambda_{2\text{av}}}{\lambda_1 - \lambda_{2\text{av}}}\left[e^{-\lambda_{2\text{av}}t} - e^{-\lambda_1 t}\right] \ . \tag{3.51}$$

The intensities of components in the CSD are given by,

$$I_{(i\geq 2)H}(x) = n_{2\text{av}}(x)\cdot P_{2\text{av,ic}}\cdot P_{1,\text{ic}} \ , \tag{3.52}$$

$$I_H(x) = n_{2\text{av}}(x)\left[P_{2\text{av,ic}}\cdot P_{1,\gamma} + P_{2\text{av},\gamma}\cdot P_{1,\text{ic}}\right] + n_1(x)\cdot P_{1,\text{ic}} \ , \tag{3.53}$$

$$I_L(x) = (1 - n_1(x)) + n_{2\text{av}}(x)\cdot P_{2\text{av},\gamma}\cdot P_{1,\gamma} + n_1(x)\cdot P_{1,\gamma} \ , \tag{3.54}$$

where $I_{(i\geq 2)H}(x) = \sum_{i=2}^{Z} I_{iH}(x)$. In most cases the lifetime of states in a rotational band decreases with excitation energy [Boh75b], and the decay properties of level 2_{av} will be dominated by those of level 2 in the full rotational band,

$$\lambda_{2\mathrm{av}} \approx \lambda_2 \ , \tag{3.55}$$

$$P_{2\mathrm{av},ic} \approx P_{2,ic} \ . \tag{3.56}$$

Rigid rotor model

In section 2.4.2, equation 2.40 gave the lifetime for levels which de-excite via stretched $E2$ transitions between successive levels in a $K = 0$ rotational band. This sort of level scheme is commonly seen in deformed even-even nuclei and assumed in the rotational band shown in fig. 3.5. The equation is given again here,

$$\tau(I) = \frac{0.826}{E_\gamma^5 Q_0^2 (1+\alpha)} \frac{8I^2 - 2}{3(I-1)I} \ \ [\mathrm{ps}] \ , \tag{3.57}$$

where E_γ is the transition energy in MeV, α is the internal conversion coefficient for the transition, Q_0 is the intrinsic quadrupole moment in units of $e\,\mathrm{b}$ and $\langle I\,020|I{-}2\;0\rangle$, the relevant Clebsch-Gordan coefficient, is replaced by an expression depending on I. If a deformed rigid-rotor model is assumed for the nucleus then a single quadrupole moment is used to describe the whole band. The lifetime for every state in the band is then contained within a single free parameter, Q_0. This model is used in chapter 5 to allow for a better fit to experimental data when using the Bateman method to obtain lifetime information for low-lying states in the ground-state rotational band of ^{178}Pt.

Chapter 4

Experimental Methodology and Apparatus

An experiment was performed at the Accelerator Laboratory of the University of Jyväskylä, Finland to measure the lifetime of excited states in ^{178}Pt. The experimental setup and method are described in this chapter. A 2 pnA beam of ^{32}S from the K130 cyclotron was used to bombard a 1 mg/cm^2 ^{152}Sm target with an upstream 1.5 mg/cm^2 Ta backing at an energy of 192 MeV over a period ∼2 days. The DPUNS plunger housed the target and a movable 0.29 mg/cm^2 Ni charge reset foil which was employed downstream of the target with respect to the beam direction. DPUNS was connected to the MARA recoil separator which separates ions by the mass/charge (m/q) value. The JUROGAM 3 spectrometer surrounded the target position and was used to detect prompt γ radiation. An MWPC and DSSSD were employed at the focal plane of MARA in order to detect recoiling ions and their subsequent decays. Data were collected for 12 plunger distances that belong to the region-of-sensitivity to measure the lifetime of the 2_1^+ excited state.

4.1 Heavy ion fusion evaporation reactions

Heavy ion fusion evaporation is an extensively used tool in nuclear physics experiments to create heavy proton-rich nuclei. A projectile, ${}^{A_p}_{Z_p}X$, collides with a stationary target nucleus, ${}^{A_t}_{Z_t}Y$, to create a compound nucleus in an excited state via ${}^{A_p}_{Z_p}X + {}^{A_t}_{Z_t}Y \rightarrow {}^{A_p+A_t}_{Z_p+Z_t}C^*$. For the fusion to happen the projectile ion must have enough energy to overcome the Coulomb barrier that is caused by the repulsion of positive protons in each nucleus. The height of the fusion barrier can be calculated using the classical Bass model [Bas74],

$$B_{\text{fusion}} = 1.44\frac{Z_pZ_t}{R_{pt}}\left[\frac{R_{pt}}{R_{pt}+d_{\text{fu}}} - \frac{1}{x}\frac{d}{R_{pt}}\exp\left(\frac{-d_{\text{fu}}}{d}\right)\right]\text{[MeV]} \tag{4.1}$$

where the dimensionless quantity,

$$x = 1.44\frac{Z_pZ_t}{R_{pt}}\frac{1}{a_sA_p^{1/3}A_t^{1/3}} \tag{4.2}$$

is the ratio of the Coulomb force to the nuclear force at the point of contact $r = R_{pt} = r_0(A_p^{1/3}+A_t^{1/3})$. The constant $a_s = 17.23\,\text{MeV}$ is the surface-term constant in the liquid-drop model. The "fusion distance", d_{fu}, depends on the fragment pair,

$$\frac{d_{\text{fu}}}{d} \approx \frac{-\ln x}{1-2\frac{d}{R_{pt}}}. \tag{4.3}$$

According to ref. [Bas74], the range of the nuclear interaction $d = 1.35\,\text{fm}$ is a good value for heavy projectiles when $r_0 = 1.07\,\text{fm}$ is used.

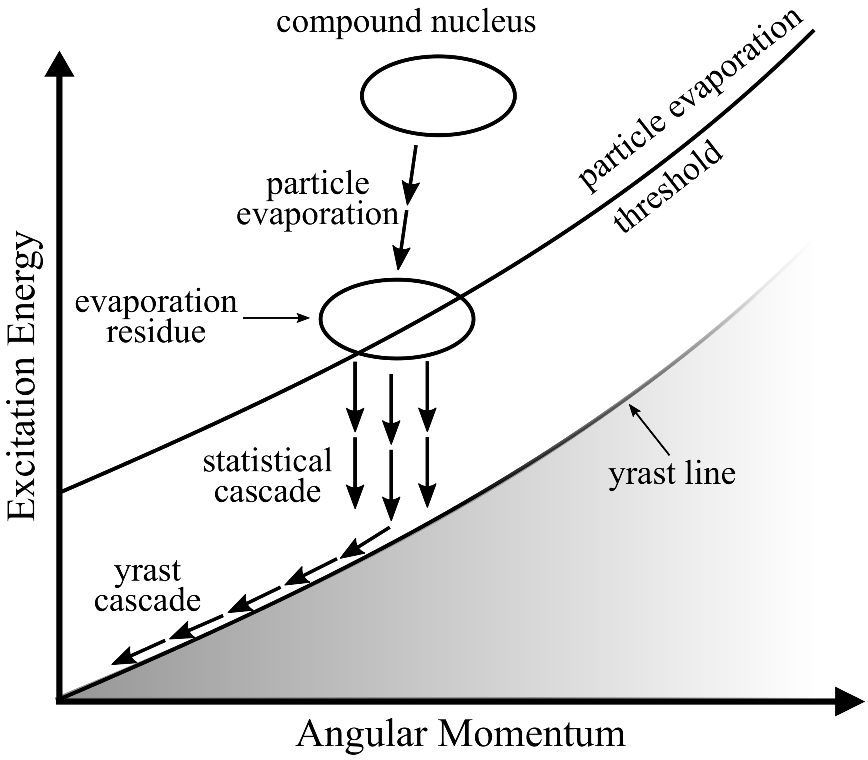

Figure 4.1: De-excitation of a compound nucleus after the fusion of a projectile and target nucleus. The yrast line follows a $I(I-1)$ dependence. At high angular momentum ($I > 30$) the yrast line is shown to fade out as this dependence becomes unlikely due to e.g. pair breaking [And76].

Typically, the projectile ion has to be accelerated to energies $> 100\,\mathrm{MeV}$ to overcome this barrier where the fusion the two particles can take place. The compound nucleus is formed with a high excitation energy and a large angular momentum. The de-excitation process of the compound nucleus is shown schematically in fig. 4.1. It quickly de-excites ($t \sim 10^{-19}$s) via the emission of neutrons, protons and alpha particles. Typical values for the kinetic energy of these particles range between 1-2 MeV for neutrons to around 20 MeV for alpha particles. Once the excitation energy goes below the particle evaporation threshold, the compound nucleus de-excites from a continuum of states down to low-energy discrete states, via a statistical cascade of high energy, low angular momentum γ rays. The nucleus then transitions down to its ground state via low-energy transitions between yrast states. An yrast state is defined as the lowest-energy state for a given angular momentum.

As well as fusion-evaporation products being produced, there is a large background from scattered beam particles and fission products. These two sources of background are much lighter than the fusion-evaporation products and can be removed using a recoil separator (see sec. 4.4) and with recoil tagging techniques (see sec. 4.7).

4.2 JUROGAM 3 in-beam array

The JUROGAM 3 in-beam γ-ray spectrometer is an array of high-purity germanium (HPGe) detectors used to detect prompt γ-ray radiation following heavy-ion fusion-evaporation reactions at the target. The array consists of 15 EUROGAM Phase I [Bea92] and 24 EUROGAM II Clover HPGe detectors [Duc99] arranged into four rings at fixed polar angles with respect to the beam direction, as shown in fig. 4.2. A Phase I detector is a single coaxial n-type HPGe crystal of diameter 72 mm and length 80 mm, whilst the Clover detectors comprise four close packed coaxial n-type HPGe crystals of diameter 50 mm and length 70 mm each, all in a single encapsulation [Ebe08]. Information on the HPGe detectors and the angle of each ring with respect to the beam direction are shown in table 4.1. Due to the geometry of the Clover detectors, two angles are given for the rings containing Clover detectors.

When a γ ray scatters into or out of a HPGe detector it does not deposit its full energy and will contribute to the Compton background. For this reason the HPGe detectors are surround by bismuth germanate (BGO) scintillators which have poor energy resolution but high detection efficiency. When a HPGe detector and a BGO detect a γ ray in coincidence the event is vetoed and discarded from the data. The BGO detectors therefore act as Compton-suppression

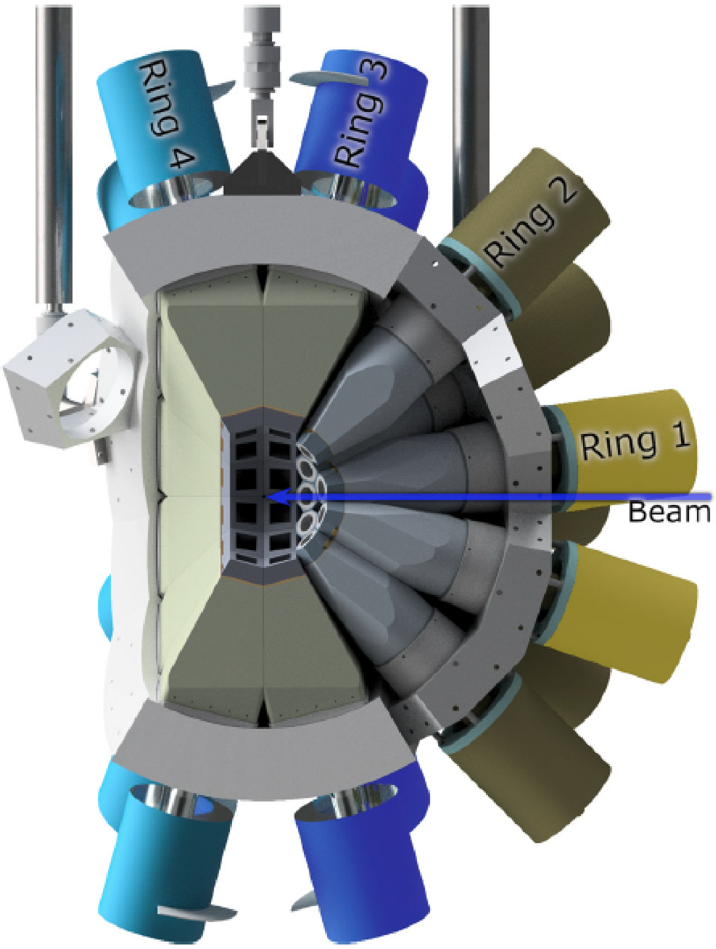

Figure 4.2: A rendered design of the JUROGAM 3 spectrometer with 15 Phase I and 24 Clover detectors arranged into 4 rings. Information on each ring is given in table 4.1. This figure is taken from ref. [Pak20].

shields and reduce the background of scattered events. The detection efficiency of the entire JUROGAM 3 array is reported to be 11.3(2)% at 356 keV and 5.2(1)% at 1332 keV. The full array has a full-width half-maximum (FWHM) resolution of 2.11(41) keV at 356 keV and 2.85(37) keV at 1332 keV [Pak20].

In a typical experiment, γ rays are emitted from recoiling nuclei moving at velocities that are in the range $\beta = v/c = 1 - 8\%$ [Pak20]. This causes the detected energy to be Doppler shifted. This effect gives rise to the Doppler broadening of the γ-ray peaks, which is given

Table 4.1: The JUROGAM 3 spectrometer is made up of a combination of Phase I and Clover germanium detectors arranged into four rings at different angles with respect to the beam direction. Two angles are given for the Clover detector due to the arrangement of the crystals.

Ring	Detector Angle (deg)	Type of detectors	Number of detectors
1	157.6	Phase I	5
2	133.57	Phase I	10
3	(100.0, 109.0)	Clover	12
4	(71.0, 80.0)	Clover	12

by,

$$\Delta E = \beta \sin(\theta)\,\Delta\theta\, E_0 \tag{4.4}$$

where $\Delta\theta$ is the opening angle of the detector, θ is the detector angle with respect to the recoil velocity and E_0 is the γ-ray energy in the rest-frame of the nucleus [Ebe08]. The direction that the recoil travels is along the beam axis. The crystals of the Clover detectors have smaller opening angles which reduces the effect of Doppler broadening. For this reason the Clover detectors are placed at angles close to 90° relative to the beam direction where broadening is greatest.

Equation 3.1 gave the Doppler-shifted energy of a γ ray emitted from a nucleus moving with some velocity. By considering this equation for a nucleus moving at non-relativistic speeds, as expected in a heavy ion fusion-evaporation reaction, the difference between the Doppler-shifted energies, $|E - E_0|$, will be minimum at $\theta \sim 90^\circ$ and maximum at 0°, 180°. The RDDS method benefits from being able to easily distinguish different Doppler-shifted components of a γ-ray transition. Therefore, in an ideal setup for RDDS experiments, detectors would be placed at angles such that $|E - E_0|$ is maximised.

In JUROGAM 3 the more efficient Clover detectors are placed at angles close to 90°, which is not ideal for RDDS experiments. However, there are still 15 Phase I detectors placed at large angles with respect to the beam direction. For this reason RDDS techniques have been used frequently with the JUROGAM spectrometer [Gra05, MG19, Gra06, O'D09, Gra16, Wat11, Pro11, Hod16, Pro10, Gra09, Say17, Sch10, Don15, Tay13a, Pro12, Tay15, Pro13, Don17a, Li16, Don17b]. In an experiment using the charge plunger method, the use of JUROGAM 3 allows one to apply a DDCM coincidence analysis to the data (see section 3.3) [Bar20b, Hee21]. A DDCM coincidence analysis requires recoils to be selected in coincidence with the feeding transition to the level of interest occurring before the reset foil. Therefore, the analysis benefits from being able to easily resolve different Doppler-shifted components in the γ-ray energy spectrum, similar to the RDDS method.

4.3 DPUNS plunger device

The Differential Plunger for Unbound Nuclear States (DPUNS) [Tay13b] is a plunger device purposely built to perform lifetime measurements at the University of Jyväskylä Accelerator Laboratory on excited states in exotic nuclei with low population cross sections. A schematic of the device is shown in fig. 4.3. DPUNS was built to work in either a vacuum or gas environment and as such can be coupled to both the RITU and MARA separators. As it was essential that the charge state of ions remained unchanged when travelling to the focal plane, DPUNS was coupled to MARA in this experiment as shown in fig. 4.4. The part of DPUNS that houses the target and degrader was surrounded by the JUROGAM 3 spectrometer to measure prompt γ rays. The degrader foil was replaced with a 0.29mg/cm^2 Ni charge reset foil.

The DPUNS plunger device is based on the Köln plunger device [Cle78]. A Physik Instrumente (PI) [Phy] linear piezoelectric stepping motor is used to vary the distance between the target and reset foil. The stepping motor has a 30 mm travelling range, with an accuracy of ~ 20 nm. To measure absolute distances it is necessary to find the minimum separation between the target and reset foils. To do this the capacitance method is used [Ale70, Dew12]. The target and reset foil are stretched on cones to ensure a flat surface. The foils are aligned

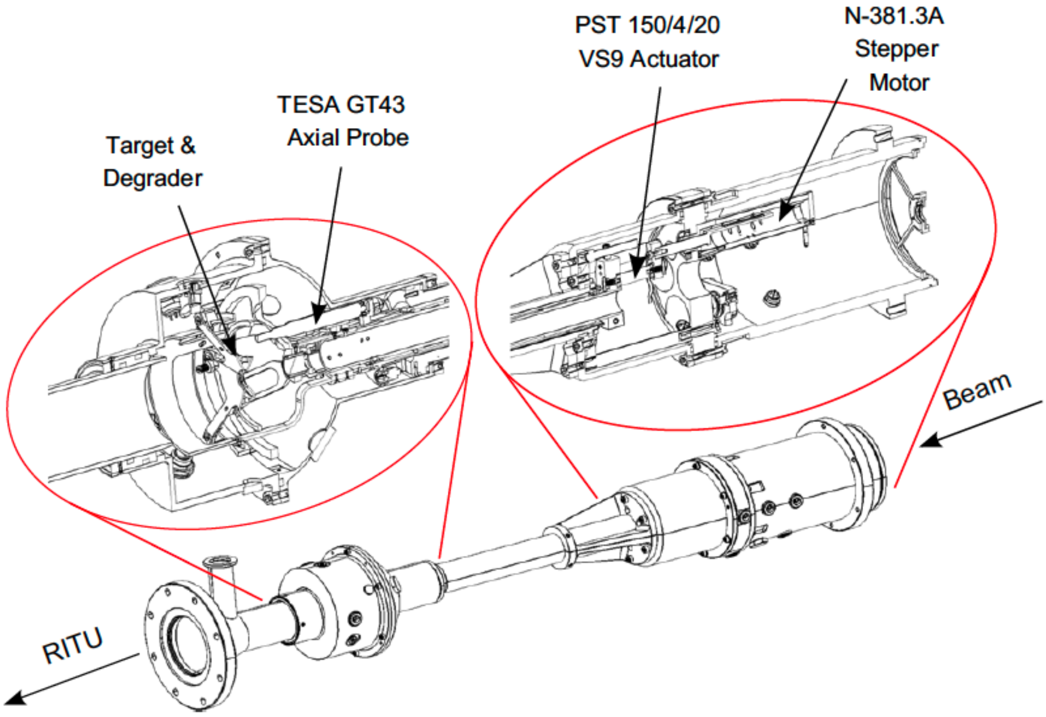

Figure 4.3: Schematic of the DPUNS plunger device. This figure is taken from [Tay13b]. DPUNS was originally commissioned to work with the RITU separator. However, it can also be used with the MARA separator.

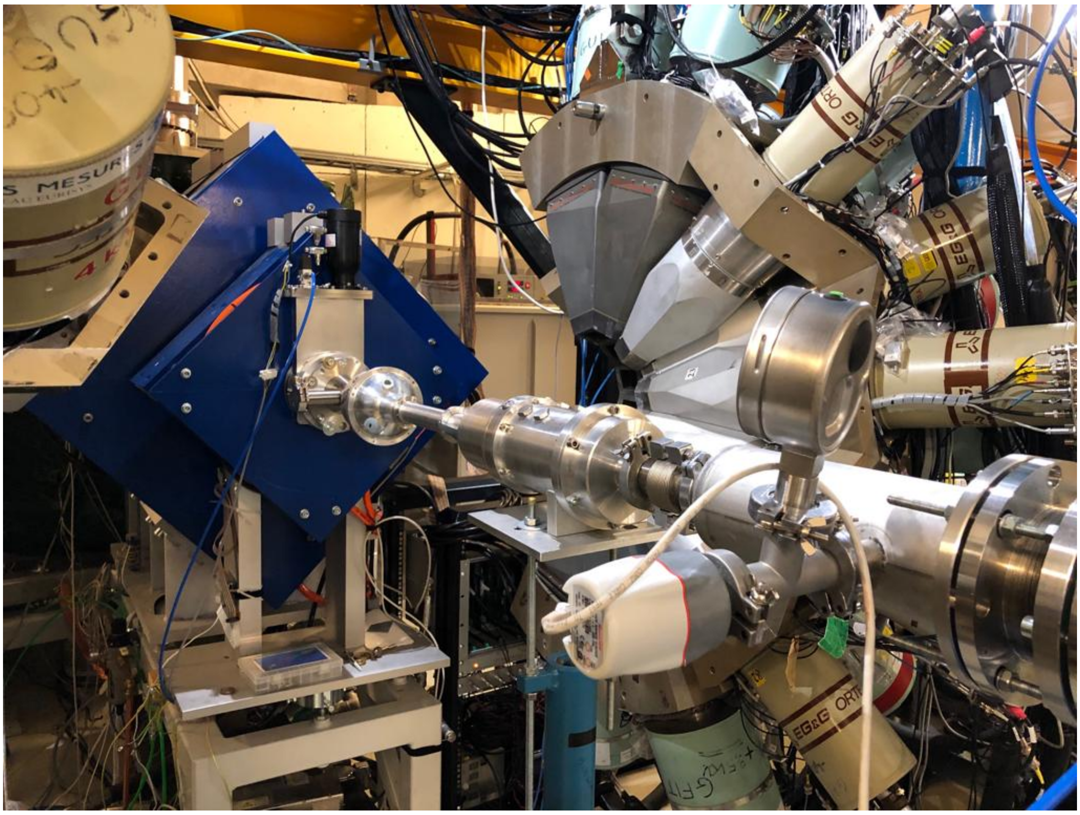

Figure 4.4: The DPUNS plunger coupled to the MARA recoil separator. The DPUNS target area is surrounded by the JUROGAM 3 spectrometer.

to each other by eye to form a parallel plate capacitor with capacitance,

$$C(x) = \varepsilon_0 \frac{A}{x} \tag{4.5}$$

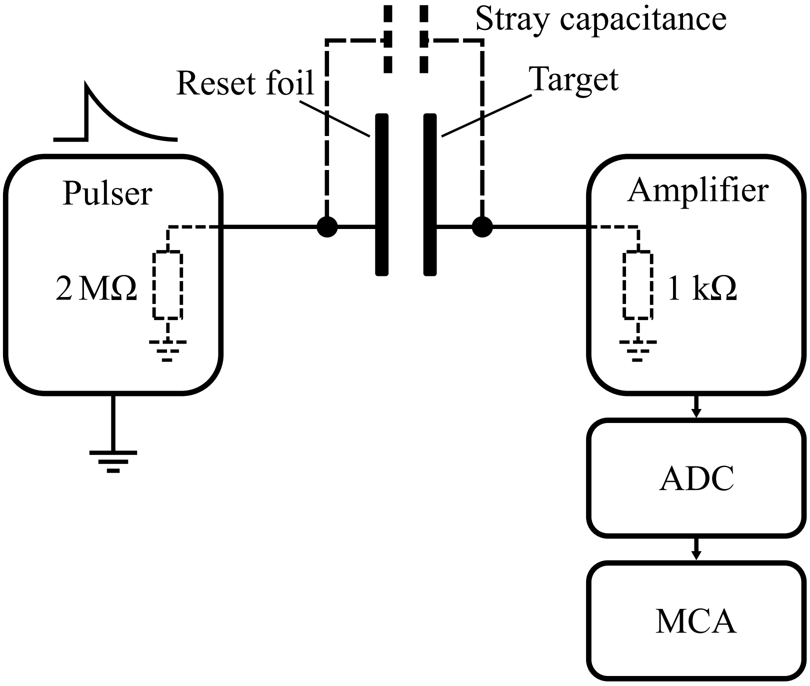

Figure 4.5: The capacitance method is used to calibrate the distance between the target and reset foils. This figure has been adapted from [Dew12] for the DPUNS device.

where A is the area of the stretched target foil, x is the target-to-reset foil separation, and ε_0 is the vacuum permittivity. A voltage pulse (V_i) applied to the reset foil induces a voltage ($V(x) \propto C(x)V_i$) on the target. This induced voltage is proportional to the inverse of the distance between the two foils. The induced target voltage is calibrated to the target-to-reset foil separation at the start of the experiment using a TESA GT 43 axial miniature probe [TES] coupled to a TT20 electronic micrometer. Fig. 4.5 shows a schematic diagram demonstrating the capacitance method. The distance calibration curve, taken at the start of the experiment, in fig. 4.6a shows induced voltage, $V(x)$, against micrometer reading (x_{micro}). Electrical contact between the foils was observed at a micrometer reading of $x_{\text{micro}} = -982.0\,\mu\text{m}$.

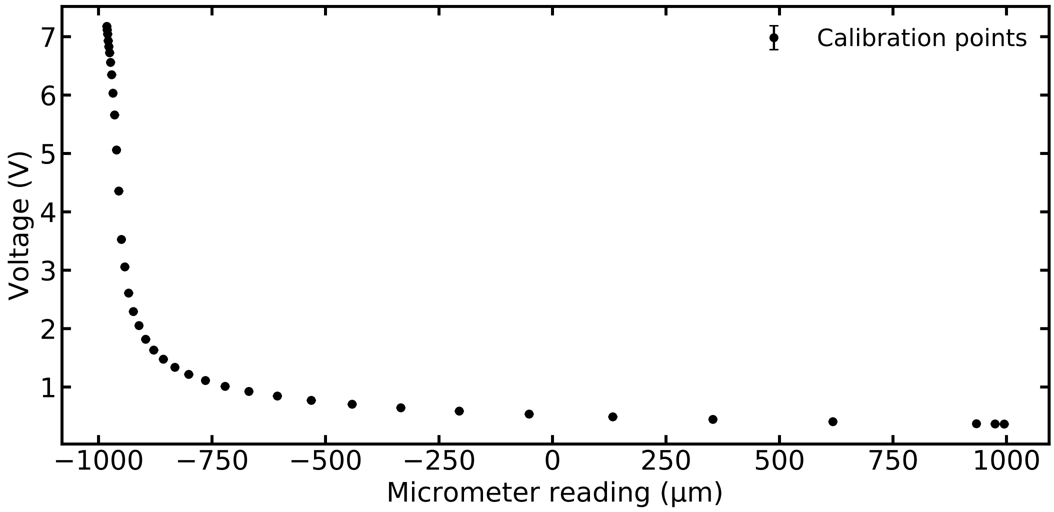

(a) V vs. x_{micro}

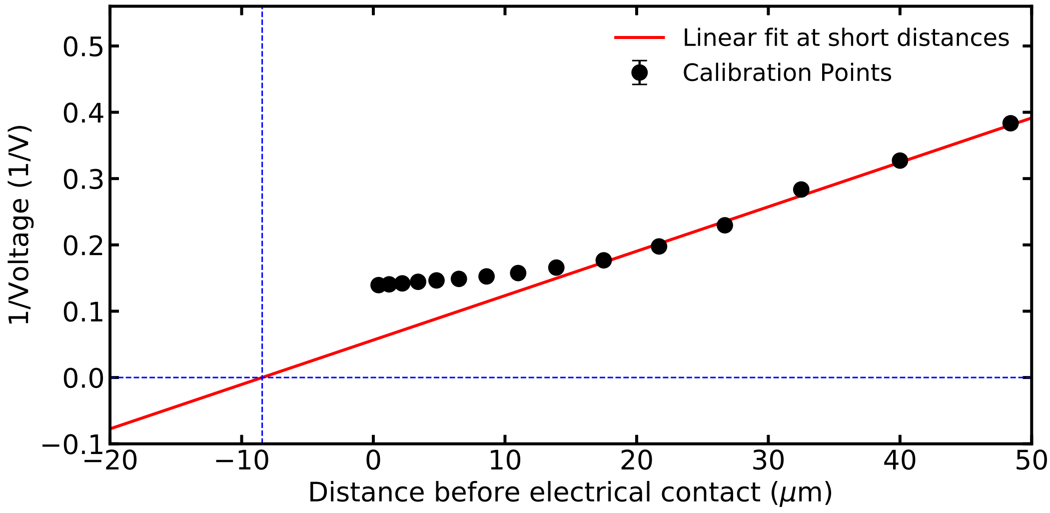

(b) $1/V$ vs x at short distances

Figure 4.6: (a) Target-to-reset foil distance calibration. The micrometer reading at electrical contact was $x_{\text{contact}} = -982.0\,\mu\text{m}$. (b) For a parallel plate capacitor the induced voltage V varies linearly with target-to-reset foil separation $x = x_{\text{contact}} + 982.0\,\mu\text{m}$. The offset between the true target-to-reset foil separation and electrical contact (see text) is measured in the calibration to be $x_{\text{offset}} = 8(1)\,\mu\text{m}$.

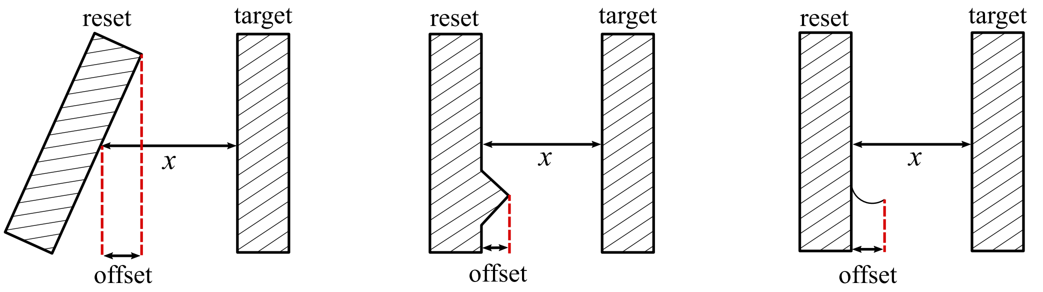

(a) Imperfect alignment (b) Surface defect (c) Dust particles on surface

Figure 4.7: During the distance calibration the two foils are brought closer to each other until electrical contact is achieved. However due to various effects the point at which electrical contact occurs is not the true zero separation point between the two foils. The effects shown have been enhanced.

Fig. 4.6b shows $1/V(x)$ against target-to-reset foil separation before observed electrical contact, $x = x_{\text{micro}} + 982.0\,\mu\text{m}$. According to equation 4.5 there should be a linear relationship between $1/V(x)$ and x. Such a linear relationship is observed at short distances with gradient $0.0067(3)$ $1/\text{V}\mu\text{m}$ and intercept $0.057(8)$ $1/\text{V}$. The gradient of the line will go to zero if part of the plunger touches a non-conductive region of the target foil, such as an oxide layer [Ale70]. This explains the deviation of calibration points in fig. 4.6b from a linear trend at very short distances ($\leq 15\,\mu\text{m}$). According to equation 4.5 at $x = 0\,\mu\text{m}$, $1/V(x) = 0\,\text{V}^{-1}$, however this is not observed. Fig. 4.7 schematically shows some of the reasons why this occurs. The foils are aligned by eye and therefore may not be perfectly parallel, there may be surface defects, or the presence of dust particles that cause a protrusion from the surface of the foil. These all contribute to an offset between the true target-to-reset separation and the point of electrical contact. From the distance calibration curve in fig. 4.6b, this offset is measured to be $8(1)\,\mu\text{m}$.

At long distances ($\geq 50\,\mu\text{m}$) the relationship becomes non-linear due to the stray capacitance of electrical leads and the target and stopper frames [Dew89]. A semi-empirical least-squares fit of the form $ax^n + bx^2 + cx^{-1}$ has been made to the voltage calibration points for mid- ($50 < x < 500\,\mu\text{m}$) and long-range ($500 < x < 2000\,\mu\text{m}$) distances. The x^{-1} term represents the "perfect" parallel plate capacitor, the x^2 accounts for edge effects on the foil, and x^n term represents higher-order corrections for the stray capacitance [Gil19a, Gil19b]. The fits are shown in fig. 4.8 and the best-fit parameters are given in table 4.2.

As beam ions travel through the target and reset foils they lose energy which causes the target to heat up and expand. Temperatures at the beam spot often reach beyond 100 °C [Dew12]. This means that the distance between the target and reset foil can change during beam on periods. To achieve constant target-to-reset foil separation the feedback method is applied.

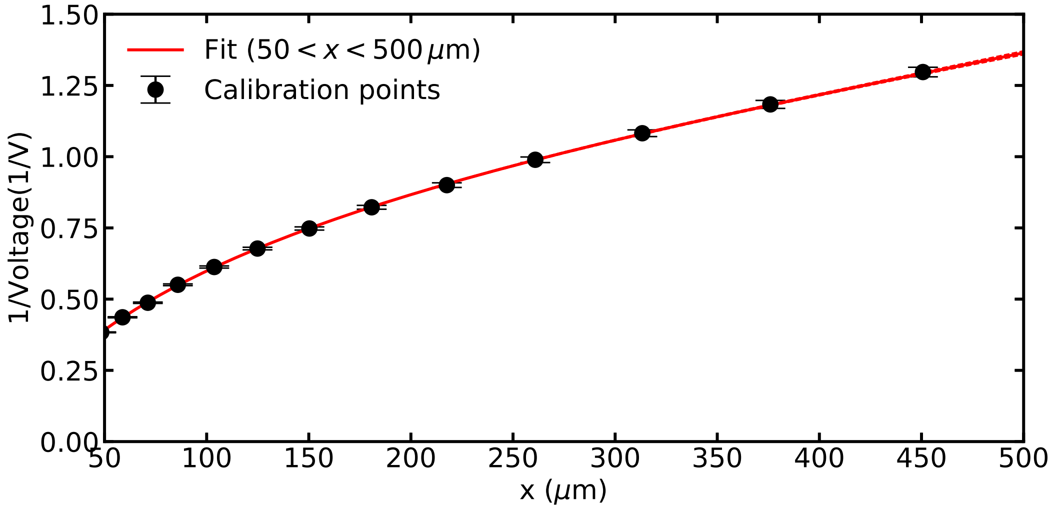

(a)

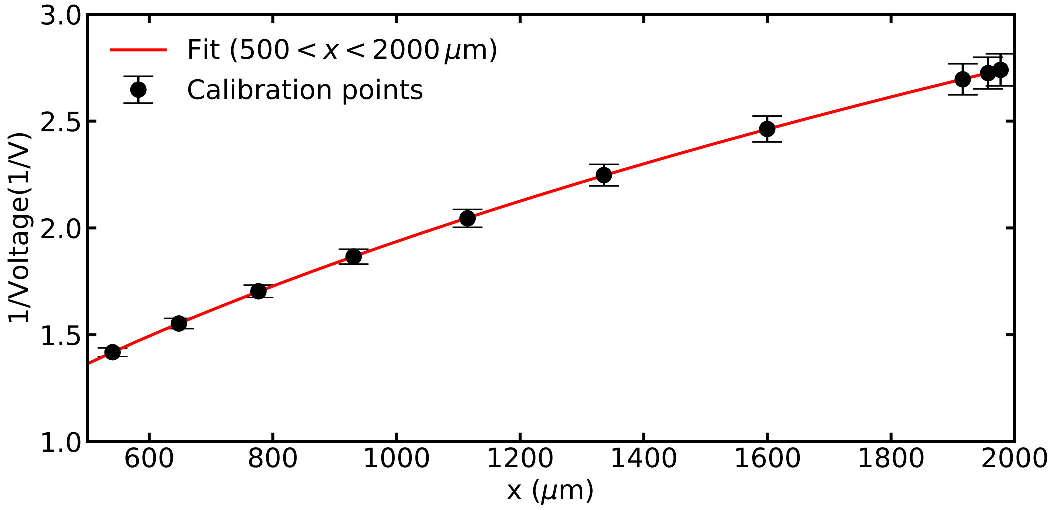

(b)

Figure 4.8: Target-to-reset foil calibrations at (a) mid-range distances ($50 < x < 500\,\mu$m) and (b) long-range distances ($500 < x < 2000\,\mu$m).

The target-to-reset foil separation is measured constantly throughout the experiment using the capacitance method. The induced signal is sampled by a 1.25 MS/s, 16 Bit, National Instruments PCI-6251 M Series data acquisition (DAQ) card and run through a modified version of the Köln plunger control software which then readjusts the target-to-reset foil separation as necessary by applying a voltage to a piezoelectric actuator. Fig. 4.9 shows an example of how the plunger feedback mechanism adjusts the position of the reset foil (blue) to keep a constant voltage value (black).

Table 4.2: Best-fit parameters for target-to-reset foil distance calibration at mid- and long-range distances.

Distance range	$a(\mathrm{V}/\mu\mathrm{m}^n)$	n	$b(\mathrm{V}/\mu\mathrm{m}^2)$	$c(\mathrm{V}\,\mu\mathrm{m})$
$50 < x < 500\,\mu$m	3.85(50)	−0.29(2)	65.4(29)	$-1.46(45) \times 10^{-7}$
$500 < x < 2000\,\mu$m	29.7(59)	−0.57(2)	−63(25)	$1.29(53) \times 10^{-9}$

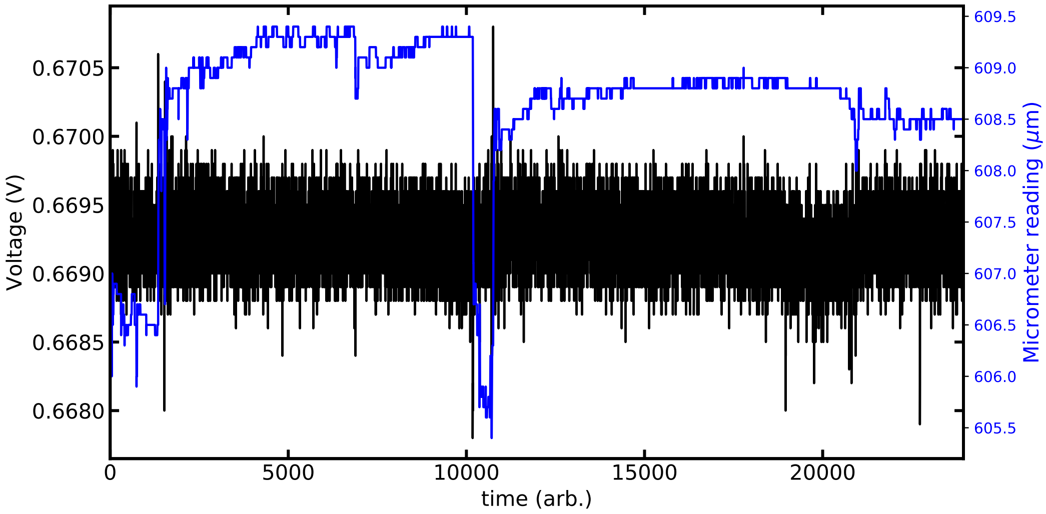

Figure 4.9: Plunger feedback example. The position of the micrometer varies in order to keep the induced voltage constant.

Distances greater than 2000 µm are outside the calibrated range of the micrometer and the feedback method can no longer be used. The target-to-reset foil separation is instead measured using the internal measurement system of the stepping motor. At these distances variations in the thickness of the target and reset foils should be small compared to their separation ($< 1\%$ [MG21a]). The effect can be estimated using the difference between the micrometer reading and the distance calculated using the capacitance method. Accounting for this effect yields an error of $\sim$10 µm for distances where $x >$2000 µm.

4.4 MARA recoil separator

After the DPUNS plunger device, nuclei travel through the vacuum-mode recoil-separator MARA (*Mass Analysing Recoil Apparatus*). MARA separates out scattered beam and fission products from fusion products. As MARA is a vacuum-mode separator, ions are separated by their mass-over-charge (m/q) ratio. For a specific mass, ions of different charge states will take different paths through the separator and arrive at different positions at the focal plane. Quadrupole and dipole magnets are used along with an electrostatic deflector. Fig. 4.10 shows a schematic diagram of the MARA setup. The electrostatic deflector and dipole magnet separate out fusion-evaporation products from beam-like recoils. The quadrupole magnets act to change the focus the beam, and are used to improve the matching of the recoil cone to the acceptance of the electrostatic deflector. A transmission detector is placed at the focal plane and downstream of that is placed an implantation detector. These are the MWPC and DSSSD respectively (see section 4.5 for more details). The horizontal position of ions in the MWPC, x_{MWPC}, determines the m/q ratio of ions.

4.4.1 Electric and magnetic rigidity

The separation of evaporation residues is determined by the magnetic and electric rigidity of the ion. The Lorentz force acting on a particle of mass m, travelling at a velocity $\vec{v}$ through an electric ($\vec{E}$) and magnetic ($\vec{B}$) field is given by,

$$\vec{F} = q\vec{E} + q(\vec{v} \times \vec{B}) \tag{4.6}$$

where q is the charge of the particle.

Magnetic rigidity

Assuming the velocity is perpendicular to the magnetic field the Lorentz force will always act perpendicular to the velocity and the particle will follow a circular path with radius ρ. The centripetal force gives $a = v^2/\rho$, and substituting $a = qvB/m$ from equation 4.6, the magnetic rigidity is given by,

$$\chi_B = B\rho = \frac{mv}{q}. \tag{4.7}$$

The magnetic rigidity can be expressed in a more practical form for non-relativistic energies,

$$\chi_B = 0.1018\frac{\sqrt{E_k m}}{q}\,[\mathrm{Tm}] \tag{4.8}$$

where E_k is the kinetic energy of the ion in MeV, the mass m is expressed in atomic mass units u and the ionic charge is expressed in elementary charges e.

Electric rigidity

For the electric rigidity, it is assumed that the ion velocity is perpendicular to the electric field. The Lorentz force will always act perpendicular to the velocity and the particle will follow a circular path with radius ρ. The centripetal force again gives $a = v^2/\rho$, and substituting $a = qE/m$ from equation 4.6, the electric rigidity is given by,

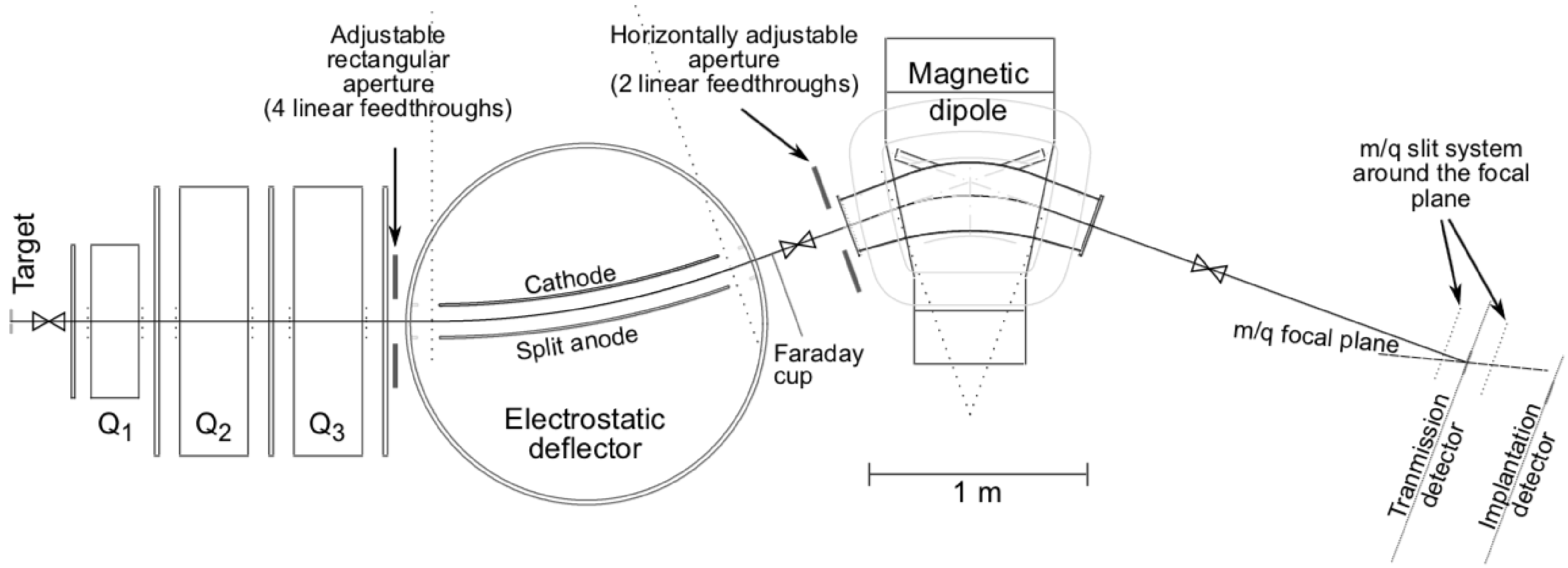

Figure 4.10: Schematic of the MARA recoil separator. This figure is taken from ref. [Sar11].

$$\chi_E = E\rho = \frac{mv^2}{q} \tag{4.9}$$

which can be expressed in more practical units for non-relativistic particles as,

$$\chi_E = \frac{2E_k}{q}\,[\mathrm{MV}] \tag{4.10}$$

where E_k is the kinetic energy of the ion in MeV and the ionic charge is expressed in elementary charges e.

The interplay between the values q, m and E_k are very important since MARA has only a finite total length along the optical axis of 6.85 m and a change in any one of these parameters can result in a very different ρ, affecting the position that ions arrive at the focal plane. Typically only a few ionic charge states can be seen at the focal plane of MARA. It is worth noting the inverse proportionality of the ionic charge state given by,

$$\chi_B, \chi_E \propto \frac{m}{q}. \tag{4.11}$$

Assuming that everything remains constant except for the charge of the ion, the change in the curvature of the path that an ion takes when travelling through MARA decreases for higher charge states. This means that as one goes to higher charge states, the separation between charge states at the focal plane becomes smaller. The opposite effect applies for the mass of the ion, and for a higher mass there will be a greater spread in the charge states observed at the focal plane.

4.4.2 Charge spectra at focal plane

The strengths of the electric and magnetic fields are chosen such that a reference particle of mass m_{ref}, charge q_{ref} and kinetic energy $E_{k,\mathrm{ref}}$ will arrive at the centre of the focal plane. The m/q value of an ion arriving at the focal plane is then calculated by,

$$\frac{m}{q} = \frac{m_{\mathrm{ref}}}{q_{\mathrm{ref}}}\left(1 + \frac{x_{\mathrm{MWPC}}}{\Delta/100}\right) \;, \tag{4.12}$$

where x_{MWPC}, the horizontal position of the ion in the MWPC, is defined such that $x_{\mathrm{MWPC}} = 0$ mm

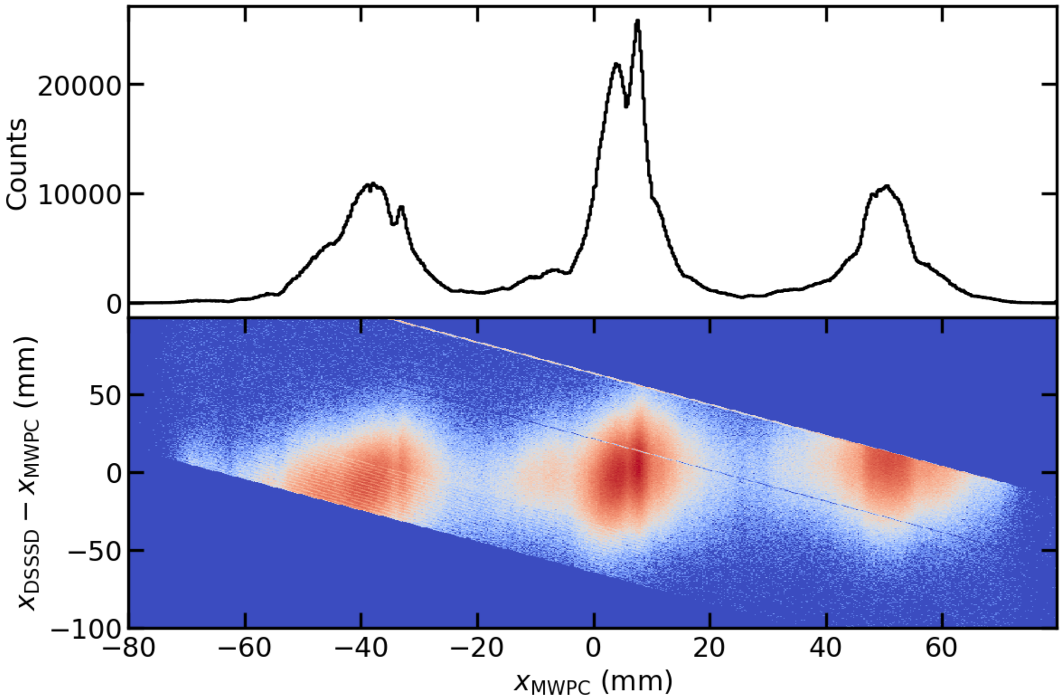

Figure 4.11: Spread of recoils in MARA during this experiment for $m_{\text{ref}} = 178\,\text{u}$, $q_{\text{ref}} = 17\,e$ and $E_{k,\text{ref}} = 23\,\text{MeV}$. The side charge states ($q = 16, 18\ e$) have a weaker transmission, in part due to the finite size of the implantation detector.

corresponds to the centre of the focal plane, and Δ is the dispersion of ions in MARA. Using the nominal quadrupole fields $\Delta = 8.0\,\text{mm}/(\%\text{ in } m/q)$ [Sar08].

Fig. 4.11 (top) shows the x_{MWPC} spectrum for a reference particle with $m_{\text{ref}} = 178\,\text{u}$, $q_{\text{ref}} = 17\,e$ and $E_{k,\text{ref}} = 23\,\text{MeV}$, obtained in this experiment. The three large peaks correspond to ^{178}Pt charge states $q = 16, 17, 18\ e$. The bottom panel of fig. 4.11 shows $x_{\text{DSSSD}} - x_{\text{MWPC}}$ against x_{MWPC} for recoils in this experiment, where x_{DSSSD} is the horizontal position of an ion in the DSSSD. The central region corresponds to the reference particle and has the strongest transmission. The intensity of the side charge states is cut off due to the finite size of the DSSSD. Therefore the intensities of the side charge states are not directly comparable to the central charge state.

4.5 Focal plane detectors

The detectors used downstream of MARA are part of the GREAT [Pag03] setup with some of the original components missing or unused. A position sensitive multiwire proportional counter (MWPC) lies at the focal plane. It is important that the MWPC is position sensitive as the horizontal position of the recoil is related to its m/q value (see equation 4.12). Just behind the MWPC is a double sided silicon-strip detector (DSSSD). Recoils pass through the

MWPC, depositing some of their energy as they go, and implant into the DSSSD. Correlated signals in the MWPC and the DSSSD allow one to distinguish between a recoil event, which will trigger a signal in both detectors, and a subsequent decay event which can only trigger a signal in the DSSSD.

4.5.1 MWPC

The MWPC has an aperture of 131 mm (horizontal) × 50 mm (vertical). The detector volume is filled with isobutane gas. Thin Mylar windows are used for the entrance and exit windows. A central anode is set to a voltage of 500 V and is surrounded by a grid of wire cathodes at ground potential. The wires are separated by 1 mm. A recoil travelling through the MWPC causes ionisation of gas particles via collisions. The subsequent free electrons are accelerated by the large electric field to the nearest wire and have enough energy to cause further ionisation. This results in an avalanche process in the high-field region close to the wire, which induces a pulse proportional to the energy deposited by the recoil.

Using a system of delay lines, a time-to-amplitude converter (TAC) is used to find the time difference between the signal coming from the central anode and the wire cathode. This gives the positional information of the wire cathode and in turn the recoil path.

4.5.2 DSSSD

After the MWPC, recoils are implanted into the DSSSD. The purpose of the DSSSD is to measure the energy of the implantation and the energy released by any further decay events. In total it consists of 72 vertical and 192 horizontal strips giving 13,824 pixels. The dimensions of the DSSSD are $48 \times 128\,\mathrm{mm}^2$ and each pixel size is $0.69 \times 0.69\,\mathrm{mm}^2$. The DSSSD has a thickness of $300\,\mu$m. The pixels allow for spatial correlation of a recoil implantation and a subsequent alpha decay as they must both occur in the same pixel. The horizontal and vertical strips were set to high and low gains respectively. This allows the horizontal strips to detect low energy signals, resulting from e.g. alpha decays, and the vertical strips to detect signals from high energy events, resulting from e.g. recoil implantation.

4.6 Data acquisition system (DAQ)

The total data readout (TDR) acquisition system is employed to process signals from JUROGAM 3 and the focal planes detectors [Laz01]. TDR is a triggerless data acquisition system whereby all the data from each detector channel is timestamped and stored. The data from all detector channels are then ordered in an event builder, and spatial and temporal correlation conditions are set using software off line. The timestamping is done using a 100 MHz clock giving a precision of 10 ns for the time difference between separate events occurring in different detector channels. The TDR system eliminates common dead time losses and is suitable for a system with a high data rate. The Grain data analysis program was used to sort the data collected with the TDR system [Rah08].

4.7 Recoil identification techniques

Despite the separation from fusion-evaporation products using MARA, there will still remain a large background of scattered beam and fission products at the focal plane. In order to perform detailed spectroscopy on nuclei produced with low cross sections, tagging techniques must be performed using energy and time coincidence gates. By setting conditions for the energy of recoils, and their time of flight between the MWPC and the DSSSD, one can distinguish between heavy fusion-evaporation residues and lighter scattered beam and fission products. Subsequent recoil-decay tagging or γ-decay tagging techniques can then be used to unambiguously identify the nuclear species of a recoil.

4.7.1 Identifying fusion-evaporation reaction products

Recoiling nuclei pass through the MWPC, depositing energy ΔE, and implant into the DSSSD where they lose the rest of their energy E. The time of flight (t.o.f.) of the recoils is defined as the time difference between the signals in the MWPC and the DSSSD, calculated using a time-to-amplitude convertor. The t.o.f. for a heavy fusion-evaporation recoil is $\sim$10 ns. A 2D histogram plot of the t.o.f. against the recoil energy detected in the DSSSD is shown in fig. 4.12 for all recoils. There is an overwhelming background originating from scattered beam and fission products. A 2D gate is set around the region corresponding to fusion-evaporation residues, shown as a black dashed line. Any recoils that did not fulfil the conditions of this gate were discarded from the data. This greatly reduces the background.

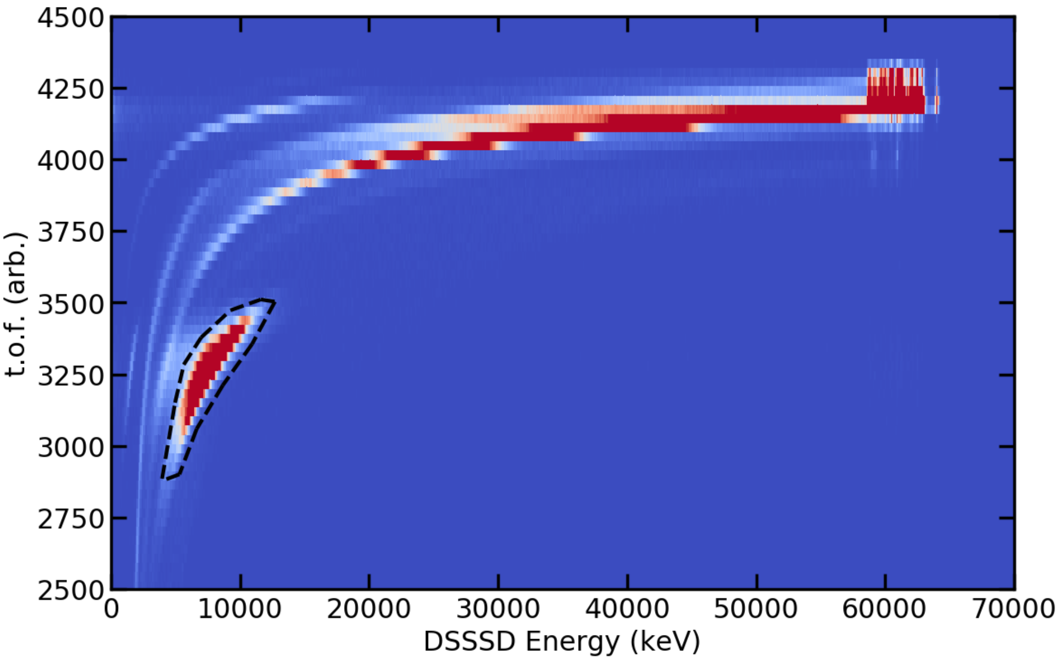

Figure 4.12: 2D histogram plot of recoil t.o.f. vs. DSSSD energy, *E* for all incoming recoils. A 2D gate is set on fusion-evaporation residues, shown as a black dashed line.

4.7.2 Recoil-decay tagging

Fusion-evaporation reactions at the target can create several neighbouring nuclear species. Due to the different products having similar masses and atomic numbers, they will all have significant transmission through the MARA recoil separator. Recoil-decay tagging (RDT) techniques are most commonly employed to distinguish the prompt γ-ray transitions emitted by a particular nucleus above the background [Pau95]. In RDT, the decay properties of a nucleus (e.g. characteristic alpha decay energy) are used to identify the species of a recoil through spatial and temporal correlations. Further temporal correlations are then used to search for prompt γ rays that originate from the tagged nucleus. Fig. 4.13 shows a schematic demonstrating how the recoil decay tagging technique works when using a recoil separator.

Consider the data stream seen by the DAQ shown in table 4.3. A reaction product (recoil

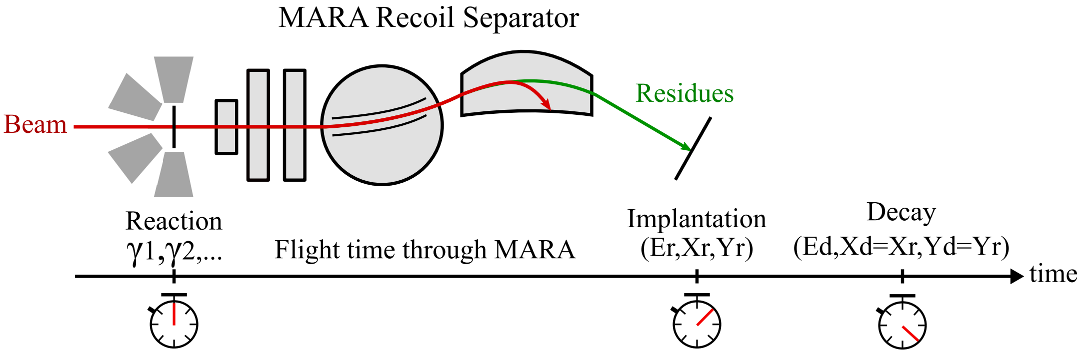

Figure 4.13: Schematic diagram to describe the recoil decay tagging technique. This figure is adapted from ref. [The15].

A) is created at the target and travels downstream towards the recoil separator. Prompt γ-ray emissions are detected with energy $E_{\gamma,A}$ by JUROGAM 3 detectors surrounding the target. The DAQ records the detection of these γ rays at a time t_0. After passing through the separator, the recoil will travel through the MWPC, depositing energy $\Delta E_{r,A}$, and implant into a pixel P_1 of the DSSSD, where it is stopped, depositing an energy $E_{r,A}$. The DAQ records the recoil implantation at a time t_2. If the nuclear species is unstable then after a certain amount of time the nucleus will decay, depositing energy $E_{d,A}$ into the same pixel, P_1, of the DSSD. This decay is recorded by the DAQ at a time t_4.

A different nucleus (recoil B) implants in to a different pixel, P_2, of the DSSSD with energy $E_{r,B}$ at an earlier time t_1 ($t_0 < t_1 < t_2$). Recoil B then decays with energy, $E_{d,B}$, at a time t_3 ($t_2 < t_3 < t_4$). By searching for events that are spatially correlated (i.e. occurring in the same pixel of the DSSSD), it is ensured that the decay in pixel P_2 ($E_{d,B}$) is not falsely assigned to recoil A.

A third nucleus from an earlier implantation (recoil C), decays in pixel P_1 with an energy $E_{d,C}$ at a time t_5. In this case, the time difference between recoil A and the decay of recoil C is $t_5 - t_2 >> t_{1/2,A}$, where $t_{1/2,A}$ is the half-life of the nuclear species which recoil A belongs to. By searching for events that are temporally correlated (i.e. occurring on a timescale similar to the half-life of the nuclear species), it is ensured that the decay of recoil C in pixel P_1 ($E_{d,C}$) is not falsely assigned to recoil A. Therefore, both spatial and temporal correlations must be performed in order to correctly assign the decay in pixel P_1 ($E_{d,A}$) to recoil A. This

Table 4.3: Example of the data stream coming from an experiment using JUROGAM 3 and the MARA recoil separator with an MWPC and DSSSD at the focal plane. The time difference between the recoil being detected in the MWPC and in the DSSSD recoil is smaller than the timestamping frequency of the DAQ and so they are registered at the same time. As mentioned in sec. 4.7.1, the flight time between the MWPC and DSSSD is measured using a TAC.

Detector	Energy	Time
JUROGAM 3	$E_{\gamma,A}$	t_0
MWPC	$\Delta E_{r,B}$	t_1
DSSSD (Pixel P_2)	$E_{r,B}$	t_1
MWPC	$\Delta E_{r,A}$	t_2
DSSSD (Pixel P_1)	$E_{r,A}$	t_2
DSSSD (Pixel P_2)	$E_{d,B}$	t_3
DSSSD (Pixel P_1)	$E_{d,A}$	t_4
.	.	.
.	.	.
DSSSD (Pixel P_1)	$E_{d,C}$	t_5

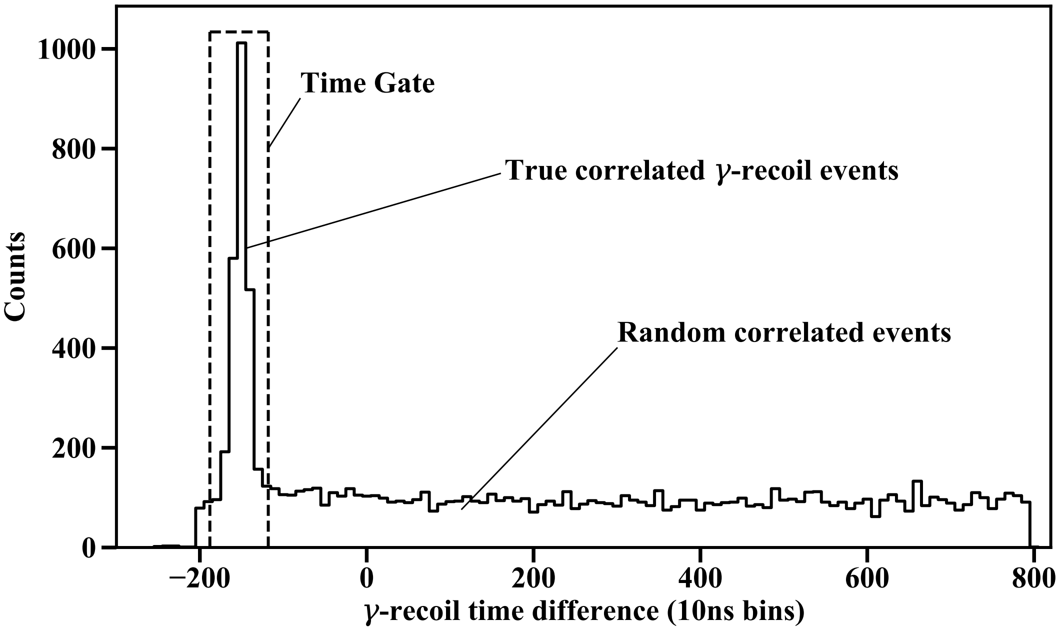

Figure 4.14: γ- recoil time difference spectrum. A peak exists for true correlated γ-recoil events. There is a flat background corresponding to random correlated γ-recoil events. A time gate is applied to choose the true correlated events.

allows for the nuclear species of the recoil to be unambiguously identified using RDT.

Another way to identify the recoil would be to use γ-recoil tagging (GRT). This is suitable when the level scheme of the nucleus is already well understood and the known energy of a γ-ray transition can be used to identify the nuclear species. Consider the example in table 4.3 again. The γ-ray energy, $E_{\gamma,A}$, is used to identify the nuclear species. However, this alone does not unambiguously assign that species to recoil A. For example, the $E_{\gamma,A}$ event could be falsely correlated with the $E_{r,B}$ event. This would correspond to a random correlation.

Fig. 4.14 shows the spectrum of γ-recoil time differences, $\Delta t_{\gamma-r}$. This spectrum was taken during the experiment described in this work. A peak exists for true correlated γ-recoil coincidences, corresponding to the flight-time of recoils through MARA (~µs). To remove random correlations a condition is placed on $\Delta t_{\gamma-r}$ so that only γ-recoil events that fall within the time gate shown are considered. Using this gate, the $E_{\gamma,A}$ event is correctly correlated with the $E_{r,A}$ event, and recoil A is correctly identified.

The advantage of using RDT over GDT or vice versa is dependent on the specific case being studied, and if possible the two techniques can be combined. Both techniques were employed in this experiment. GDT was used for performing a DDCM analysis of the charge plunger data and RDT was used for performing a Bateman analysis.

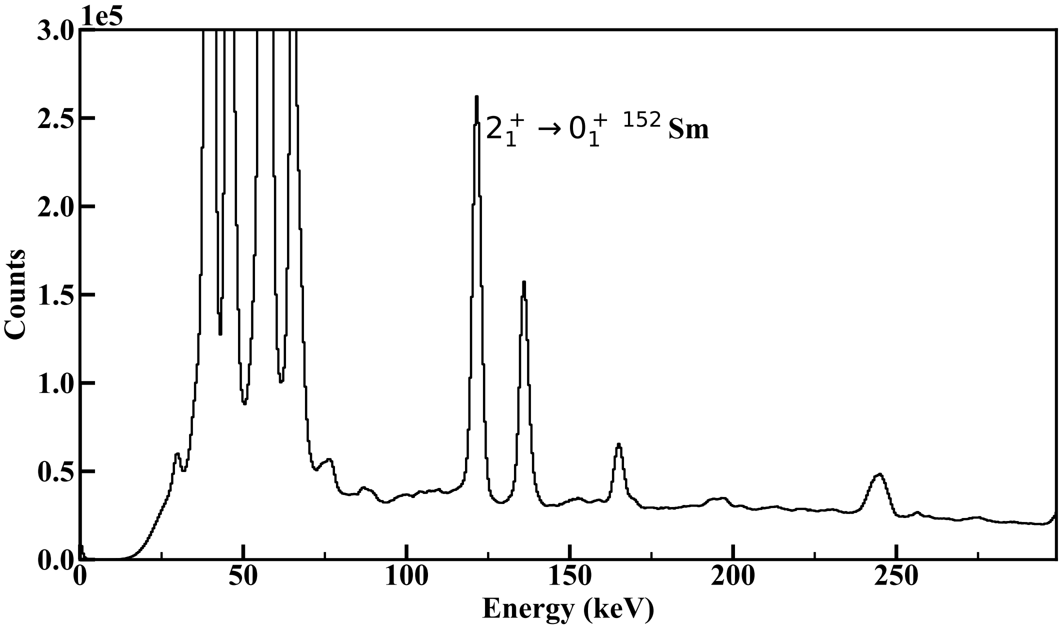

Figure 4.15: The $2_1^+ \rightarrow 0_1^+$ 121 keV peak in ^{152}Sm, populated via Coulomb interactions between beam and target particles, was used to perform normalisation across data sets.

4.8 Data normalisation

To perform analysis of data from a charge plunger experiment, one must measure the relative intensities of ions in low and high charge states for a range of target-to-reset foil distances. This means that the data sets split across different MARA settings and target-to-reset foil distances must be normalised to account for changes in beam current or the length of time in which the data is collected. For example, in this experiment to achieve acceptable statistics in the high charge component, the MARA settings were set to select high-charge ions for a longer period of time than to select low-charge ions.

The population of the 2_1^+ in the ^{152}Sm target was used to normalise the data across the experiment. This state was populated via Coulomb interactions between the beam and the ^{152}Sm target nuclei and was observed via the 121 keV γ-ray transition which depopulates to the ground state. Fig. 4.15 shows part of the raw JUROGAM 3 energy spectrum, with the 121 keV peak labelled. In order to measure the strength of this transition for each data set, a trigger was set on JUROGAM 3 detectors only. Fig. 4.16 shows how the count rate of the 121 keV peak varied with changes in the plunger and MARA settings. Beam current readings taken during the experiment are also shown in magenta. The rate varies smoothly with the beam current, giving a good indication that the measured total intensity for each data set is independent of these changes, and only dependent on the intensity of beam particles incident on the target and the length of time the data was collected for.

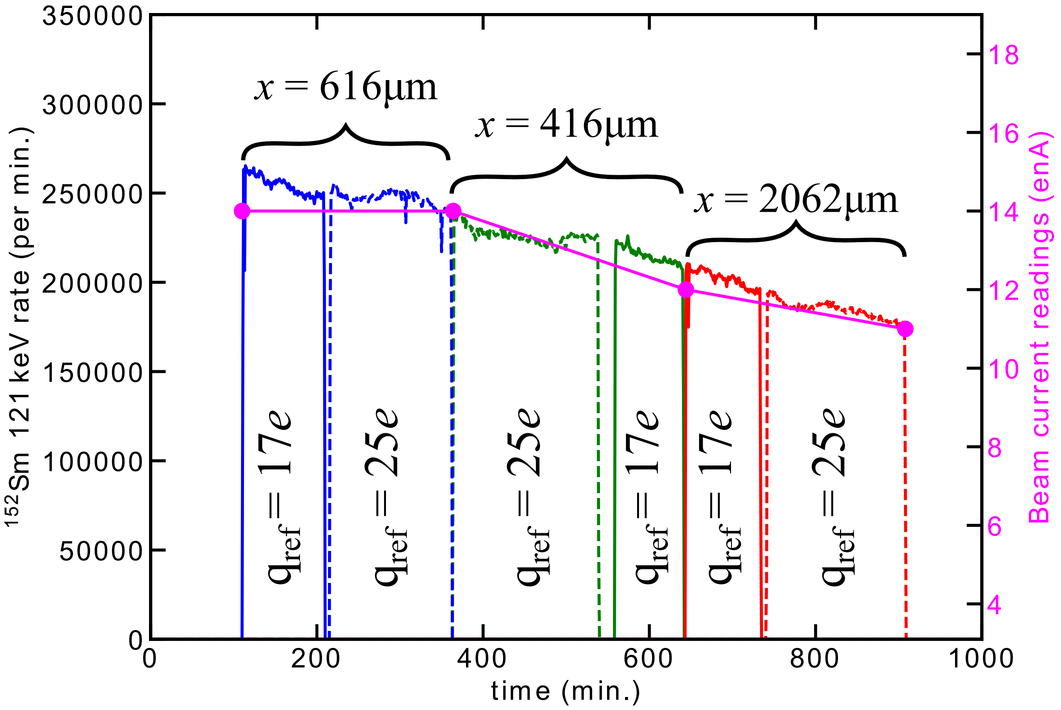

Figure 4.16: Detection rates for the $2_1^+ \rightarrow 0_1^+$ 121 keV transition in ^{152}Sm. Different target-to-reset foil distances are labelled. Beam current readings, taken after each change in target-to-reset foil distance, are shown in magenta. The rate varies smoothly with the change in beam current despite changes in target-to-reset foil distance and q_{ref}. This is a good indication that the Coulomb excitation rate is not affected by changes in MARA or plunger settings.

Chapter 5

Analysis and Results

5.1 ^{178}Pt previous studies

In the midshell region of the nuclear chart, south-west of the doubly-magic ^{208}Pb ($Z = 82$), nuclei display strong collective modes of excitation. The energy required to excite the nucleus collectively is much less than that required to cause a single-particle excitation [Kra88]. It is for this reason that the observed energies of the yrast 2^+ states peaks around magic numbers and is at a minimum in midshell nuclei with atomic mass numbers $150 < A < 190$ and $A > 230$. It is in these regions where rotational modes of excitation are most common and ground-state rotational bands can be extended up to high spin [Twi86]. Since internal conversion coefficients increase with decreasing transition energy, nuclei in these regions provide good cases for testing the charge plunger method. The nuclei in the $150 < A < 190$ are especially good cases due to the high production cross sections that have been observed.

The nucleus ^{178}Pt was first observed by Siivola by bombarding rare-earth targets with heavy ions [Sii66]. Using this method, the ground state was determined to decay by alpha emission with energy $5.44(1)$ MeV and half-life $21.3(15)$ s. Later studies confirmed the measurements and also discovered a 2^+ state at 170 keV, attributed to the first excited state in the ^{178}Pt ground-state rotational band [Dem67, Han70, Hag79, Sch80b, Bow82]. Dracoulis et al. extended the level scheme to higher spins in the ground-state band and performed lifetime measurements of the 4^+_1, 6^+_1 and 8^+_1 states using the RDDS technique with γ-ray singles events [Dra86].

In recent years, more accurate independent lifetimes measurements of these states have been performed using a DDCM γ-γ coincidence technique [Fra19]. In 2014, Li et al. published

Table 5.1: Previous lifetime measurements on yrast states in ^{178}Pt.

State	τ (ps)
2_1^+	412(30) ps [a], 445(100) ps [b]
4_1^+	40.8(24) ps [b], 54.1(46) ps [c]
6_1^+	11.9(11) ps [b], 15.7(12) ps [c]
8_1^+	3.79(50) ps [b], 5.4(5) ps [c]
10_1^+	1.84(82) ps [b]

[a] Li et al. fast-timing technique [Li14]
[b] Fransen et al. DDCM γ-γ coincidences [Fra19]
[c] Dracoulis et al. RDDM γ-ray singles [Dra86]

a result for the lifetime of the 2_1^+ using fast-timing techniques [Li14]. The current lifetime data for yrast states in ^{178}Pt are summarised in table 5.1.

Fig. 5.1 shows the level scheme for the ^{178}Pt ground state band (band *A*) up to a spin of $14\hbar$

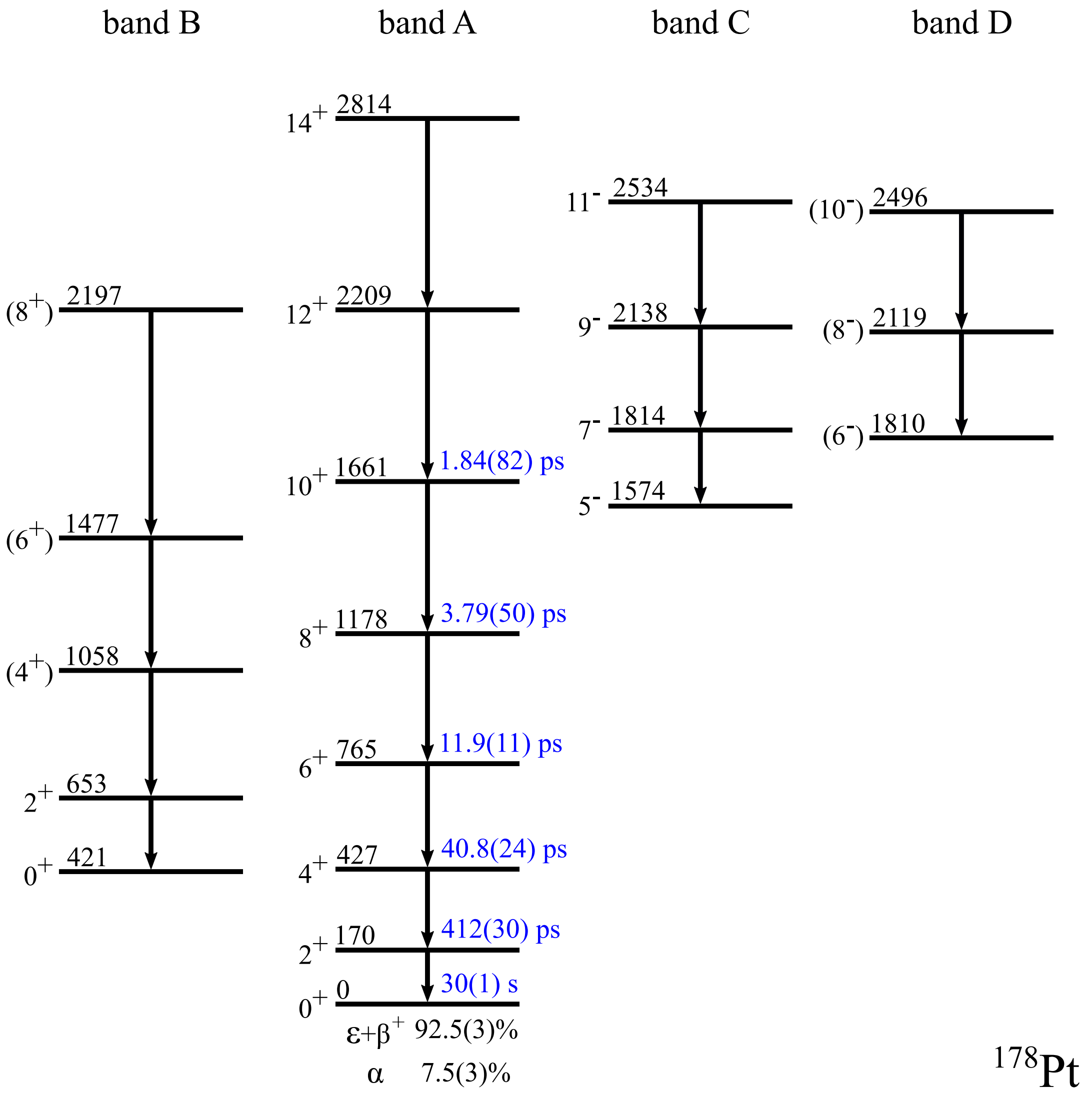

Figure 5.1: ^{178}Pt level scheme from the ENSDF database [Ach09]. Level energies (keV) and J^{π} assignments are given on the left of the level. In the ground-state rotational band (band A) lifetimes from refs. [Li14, Fra19] are given in blue. Transitions in band B were not observed in this work, whilst transitions in band C and D were observed with weak intensities.

using data from the ENSDF database [Ach09]. Internal conversion coefficients for transitions are taken from the BrIcc database [Kib08]. Also included in the figure is a shape-coexisting intruder band (band *B*), which was not seen to be populated in this study, and negative parity odd- and even-spin bands (bands *C* and *D* respectively), which were observed to be weakly populated in this study. Although these bands will not be discussed in detail here, their presence highlights the care that must be taken when using a Bateman analysis to perform lifetime measurements.

5.2 ^{178}Pt alpha-decay spectrum

The recoil decay tagging (RDT) technique was used to search for decay events that were preceded by a recoil event. For each recoil that implanted into the DSSSD, a time window of 200 seconds was used to search for a subsequent decay event. The maximum rate of recoils arriving at the DSSSD (calculated for a MARA reference particle with $q_{\text{ref}} = 17e$ at target-to-reset foil distance $x = 5061\mu\text{m}$) was 0.004 recoils/second/pixel. Fig. 5.2 shows part of the DSSSD spectrum for recoil-decay coincidence events. The spectrum contains a summation of events from all target-to-reset foil distances. At energies $5.0 < E_{\text{decay}} < 6.5$ MeV there are peaks corresponding to characteristic alpha decays. The two separate spectra shown

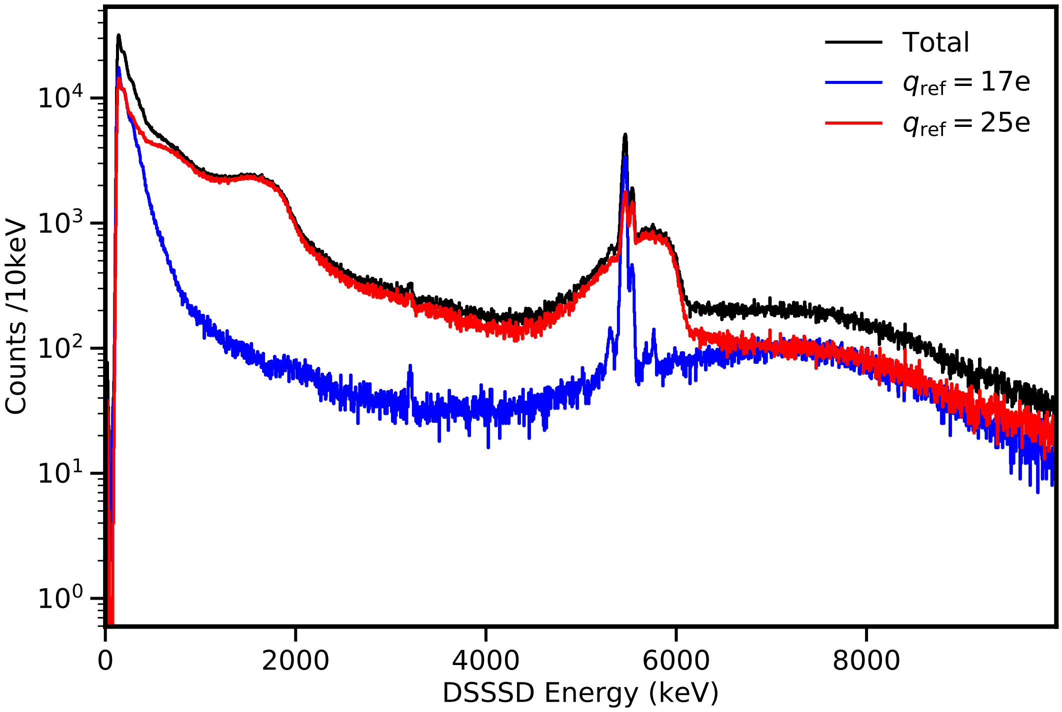

Figure 5.2: Part of the DSSSD energy spectrum for recoil-decay coincidences. This spectrum is a summation of all distances. The blue and red spectra correspond to data taken when MARA settings were optimised to transmit low charged ($q_{\text{ref}} = 17\,e$) and highly charged ions ($q_{\text{ref}} = 25\,e$) respectively.

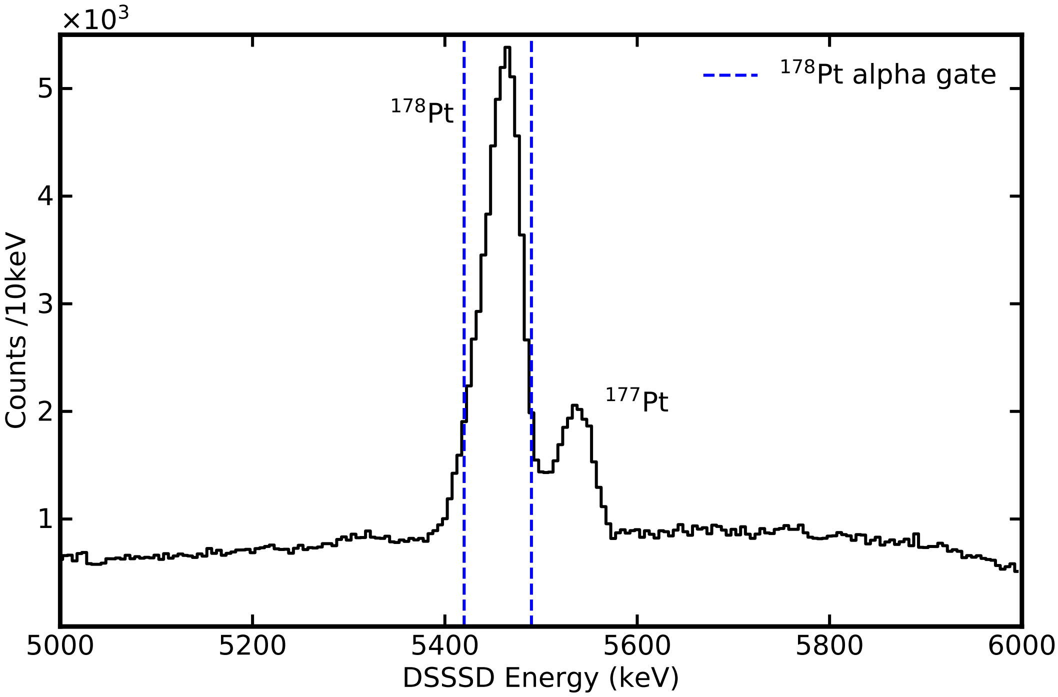

Figure 5.3: Part of the DSSSD energy spectrum for recoil-decay coincidences. This spectrum is a summation of all distances. The prominent peaks originate from the alpha decays of ^{178}Pt and ^{177}Pt recoils. The parent nucleus is labelled for each peak. The energy range used to select ^{178}Pt alpha decays for gating purposes later on in this work are shown as blue dashed lines.

in blue and red correspond to data taken when MARA settings were optimised to transmit low charged ($q_{\text{ref}} = 17\,e$) and highly charged ions ($q_{\text{ref}} = 25\,e$) respectively. There is a much higher background for the high charge ion spectrum. As the q_{ref}, m_{ref} and $E_{k,\text{ref}}$ parameters are related through equations 4.8 and 4.10, changing the MARA settings for a different q_{ref} value in ^{178}Pt will result in a different $E_{k,\text{ref}}$ value for other particles. Therefore the energy distribution of particles arriving at the focal plane will change. The broad distributions seen in fig. 5.2 at $1.5 < E_{\text{decay}} < 3.0$ MeV and $4.0 < E_{\text{decay}} < 6.0$ MeV in the $q_{\text{ref}} = 25\,e$ spectrum correspond to scattered low-Z ions which do not significantly ionize the gas particles in the MWPC, meaning they are not registered as recoils [Sar21].

Fig. 5.3 is the same as fig. 5.2 but expanded around the prominent alpha decay peaks in the spectrum. The strongest peak represents the ^{178}Pt alpha decay. There is also a weaker peak resulting from the alpha decay of ^{177}Pt recoils. In order to select ^{178}Pt recoils to view their charge state distribution, JUROGAM 3 γ-ray energy spectrum, etc., a DSSSD energy gate can be set to select recoil-decay coincidences that fall within a particular energy range. For ^{178}Pt alpha decays this energy gate is chosen to be $5.42 \leq E_{\text{decay}} \leq 5.48$ MeV and is shown as dashed blue lines in fig. 5.3.

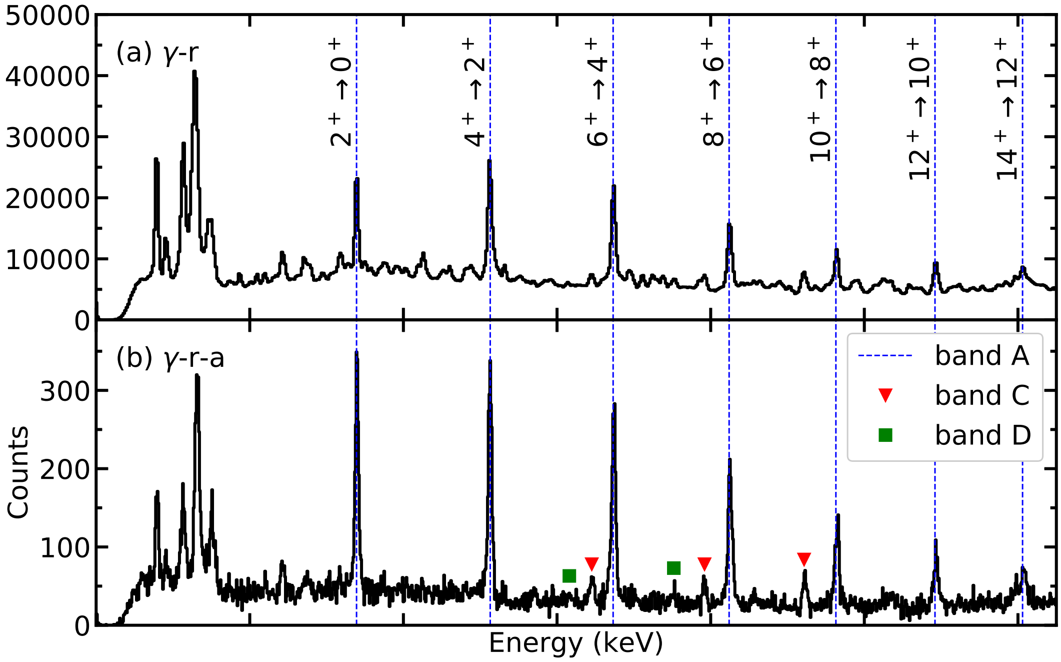

Figure 5.4: (a) Part of JUROGAM 3 spectrum for γ rays that are in coincidence with a recoil implantation. This spectrum is a summation of all distances. Yrast transitions for the ^{178}Pt ground-state rotational band are labelled. (b) Same as (a) but requiring a ^{178}Pt alpha decay to occur at least 200 s after the recoil implantation. Weak transitions originating from band C (red triangles) and band D (green squares) are labelled. See fig. 5.1 for band details.

5.3 ^{178}Pt γ spectrum

Recoils were also selected in coincidence with a γ ray detected by the JUROGAM 3 spectrometer. Fig. 5.4 (a) shows part of the JUROGAM 3 energy spectrum for γ rays detected in coindcidence with a recoil at the focal plane of MARA The spectrum contains a summation of events from all target-to-reset foil distances. At low energies ($E_\gamma < 100.0$ keV) peaks corresponding to platinum, tantalum (backing foil) and samarium (target foil) X rays are present. Intense peaks corresponding to γ-ray transitions in the ^{178}Pt ground-state band can be seen. These transitions are confirmed in fig. 5.4 (b), which shows the same spectrum as 5.4 (a), but requires a ^{178}Pt alpha decay to occur at most 200 seconds after the recoil implantation in the same DSSSD pixel. The ^{178}Pt ground-state band transitions are labelled.

5.4 Evaporation residue velocity measurement

The intensity of internal conversions occurring before and after the reset foil not only depends on the lifetime of the excited states and the target-to-reset foil distance, but also on the average recoil velocity between the target and reset foils. The Doppler shift of ^{178}Pt transitions measured by the JUROGAM 3 spectrometer was used to measure the average recoil velocity.

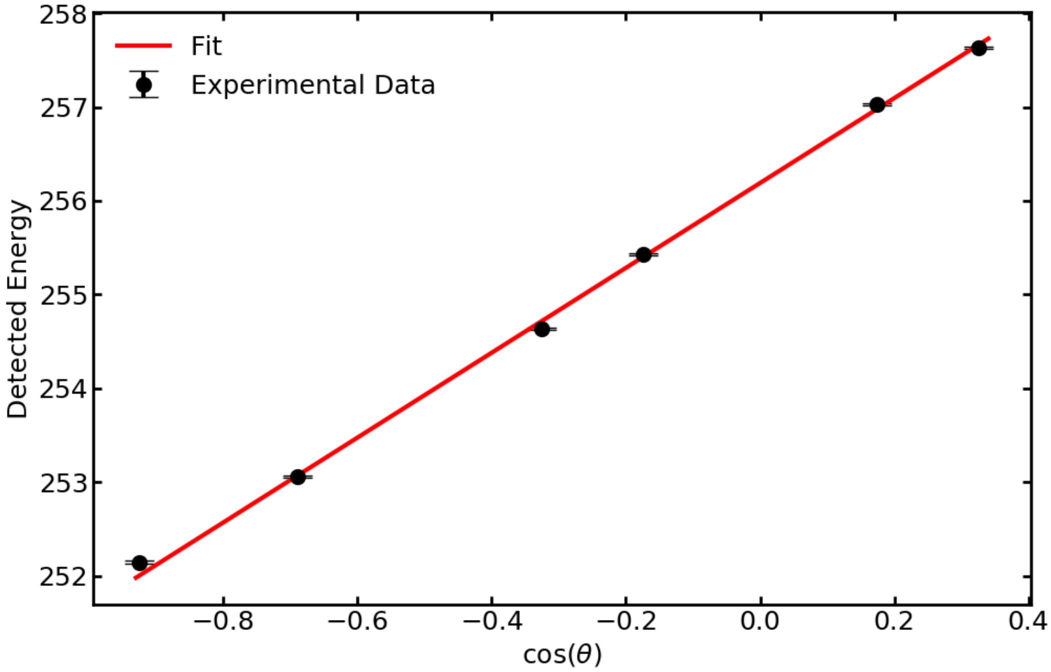

Figure 5.5: The centroid of the $4^+ \rightarrow 2^+$ 257 keV transition against JUROGAM 3 ring angle at target-to-reset foil distance x =5061 µm. A linear fit is made to the data, the gradient of which is proportional to the velocity of ^{178}Pt recoils. A similar fit was made for the $6^+ \rightarrow 4^+$ and $8^+ \rightarrow 6^+$ transitions (see table 5.2).

The measured energy of a γ ray emitted from a recoil moving at a velocity $\beta = v/c$ will be Doppler shifted. At non-relativistic energies the Doppler-shifted energy is approximated by,

$$E = E_0 \left(1 + \beta cos(\theta)\right) \tag{5.1}$$

where E_0 is the energy of the transition when the recoil is stationary and θ is the angle of the detector with respect to the direction of the recoil velocity.

In fig. 5.5, the centroid of the $4^+_1 \rightarrow 2^+_1$ 257 keV γ ray peak is plotted against $\cos(\theta)$ for the different detector angles in JUROGAM 3 . As a reminder, the angles of the JUROGAM 3 rings are given in table 4.1. The data correspond to target-to-reset foil distance x =5061 µm, at which this transition is expected to always occur before the reset foil. A linear fit made

Table 5.2: Measured velocity for three transitions in ^{178}Pt using a linear fit to the Doppler-shifted energy against detector angle for different rings in the JUROGAM 3 spectrometer. A weighted average is also given.

Transition	Energy (keV)	v/c (%)
$4^+_1 \rightarrow 2^+_1$	257	1.77(3)
$6^+_1 \rightarrow 4^+_1$	336	1.77(3)
$8^+_1 \rightarrow 6^+_1$	412	1.73(6)
Weighted Average	-	1.77(2)

to the data shown in fig. 5.5 gives the velocity of ^{178}Pt recoils between the target and reset foils according to equation 5.1. A similar fit was made to data for the $6_1^+ \rightarrow 4_1^+$ and $8_1^+ \rightarrow 6_1^+$ transitions at target-to-reset foil distance $x = 5061$ µm. Table 5.2 shows the velocity measured by each fit along with a weighted average.

5.5 ^{178}Pt charge-state distribution scan

As discussed in section 4.4, the number of charge states that can be seen at the focal plane of MARA will depend on the value of the reference charge state. In this experiment the number of charge states that could be seen at the focal plane varied between three ($q_\text{ref} = 17\,e$) and five ($q_\text{ref} = 25\,e$) charge states. To view the entire charge-state distribution (CSD), a scan must be performed over a range of reference charge states. Before the experiment it was decided that it would take too long to scan the entire CSD for each target-to-reset foil distance. Instead a scan was performed at just three distances, $x = 5061$ µm, 1543 µm and 43 µm. These scans were then used to identify the different charge components in the CSD. For the low and first-high charge component, a single reference charge state was chosen to represent the intensity of that component and, for each plunger run, data were collected using MARA settings corresponding to these reference charge states. Here the distinction is made that a scan is a set of data obtained with the purpose of identifying the different charge components in the CSD; whereas a plunger run is a set of data obtained with the purpose of performing a lifetime measurement. The majority of the beam time during this experiment was spent performing plunger runs.

Fig. 5.6 shows an example 2D histogram of recoil m/q value against recoil decay energy at the focal plane of MARA for recoils in coincidence with a subsequent ^{178}Pt alpha decay during the $x = 1542$ µm CSD scan. A gating condition is set to only integrate counts that fall within the chosen ^{178}Pt alpha decay energy range. This is shown as a lighter shaded region in fig 5.6. A separate gate, shown as a darker shaded region in fig. 5.6, is set to integrate counts in the energy range $5.67 \leq E_\text{decay} \leq 5.73$ MeV. This is used to estimate the number of background counts that arise as random coincidences. The background gate was chosen at this energy as it lies close to the ^{178}Pt alpha energy but does not show any alpha-decay peaks in the recoil-decay DSSSD energy spectrum (fig. 5.3).

Counts within the shaded regions are integrated along the DSSSD energy axis to find the projection of counts onto the m/q axis for each of the shaded regions shown in fig. 5.6. The

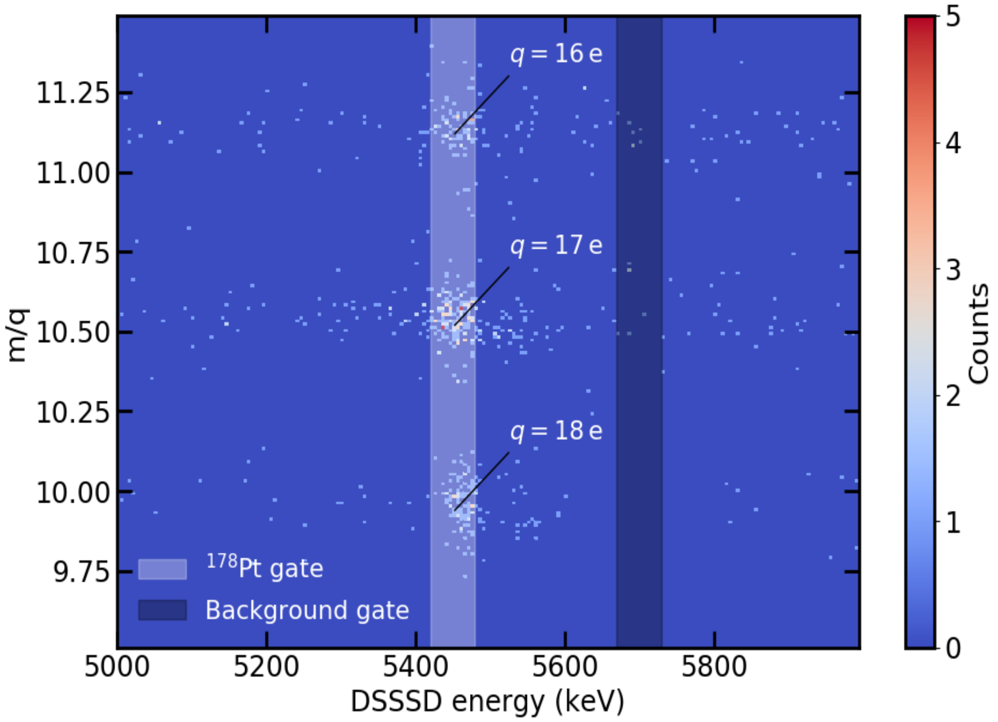

Figure 5.6: Example 2D spectrum of m/q against DSSSD energy taken during a scan of the CSD at target-to-reset foil distance $x = 1542\mu\mathrm{m}$. The reference charge is $q_{\mathrm{ref}} = 17\,e$. The lighter shaded region defines a gate set on ^{178}Pt alpha-decay events, whilst the darker shaded region defines a background gate.

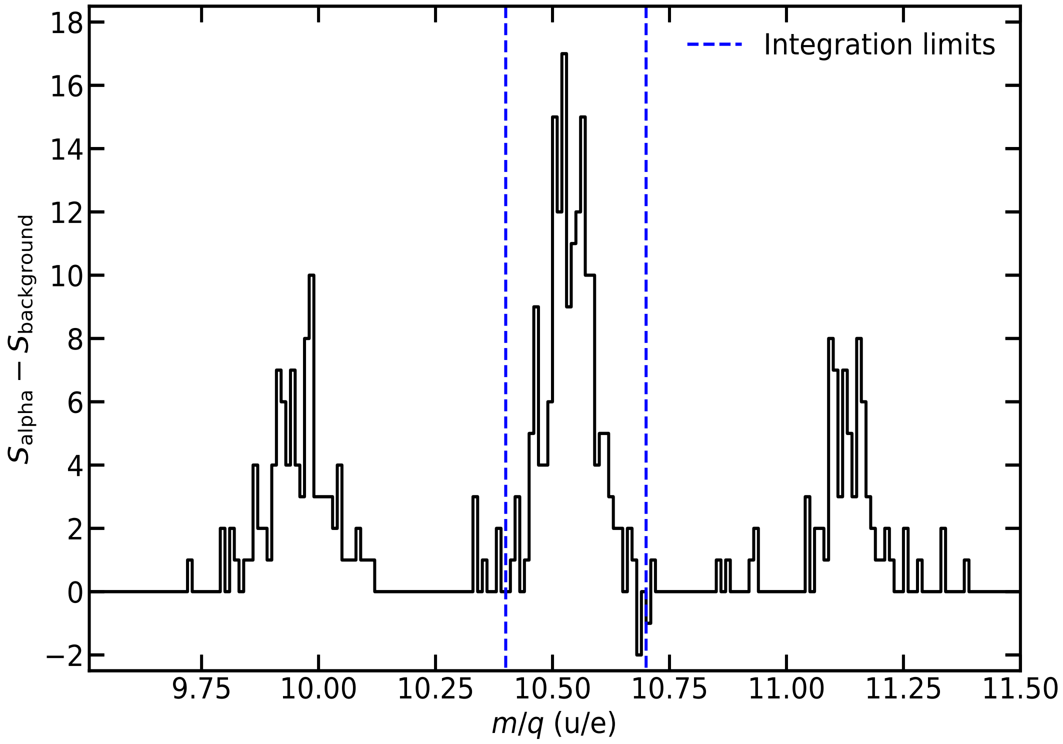

Figure 5.7: Example spectrum of m/q taken during a scan of the CSD at target-to-reset foil distance $x = 1542\mu\mathrm{m}$. The spectrum is the difference between the projection of counts onto the m/q axis for the shaded regions shown in fig. 5.6. The reference charge is $q_{\mathrm{ref}} = 17\,e$. The limits of integration for this charge peak are shown as dashed blue lines.

resultant spectrum, shown in fig. 5.7, is,

$$S(m/q) = S_{\text{alpha}}(m/q) - S_{\text{background}}(m/q) \tag{5.2}$$

where $S_{\text{alpha}}(m/q)$ is the projection of counts in the lighter shaded region and $S_{\text{background}}(m/q)$ is the projection of counts in the darker shaded region. The counts in the central charge peak are integrated to find the number of ^{178}Pt recoils detected in the reference charge state, $I(q_{\text{ref}})$,

$$I(q_{\text{ref}}) = \int_{i_1}^{i_2} S(m/q) \;\; d(m/q) \tag{5.3}$$

where i_1 and i_2 are the limits of integration for the central charge peak, chosen to include the majority of counts in the central charge peak. These limits of integration for the central charge peak are shown as blue dashed lines. A normalised count $I(q_{\text{ref}})_{\text{norm}}$ is then obtained by using the Coulomb excitation of the 2_1^+ state in the ^{152}Sm target as described in section 4.8.

The process was repeated for all reference charge states included in the scan. The CSD of

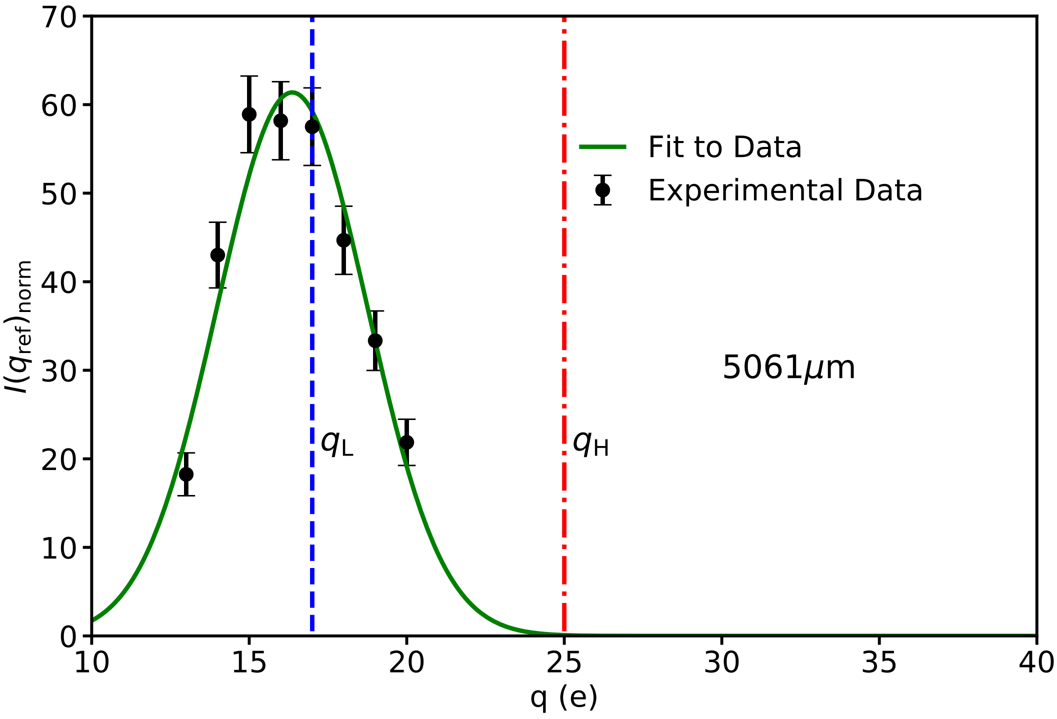

Figure 5.8: Charge-state distribution for ^{178}Pt recoils at target-to-reset foil distance x =5061 µm. The recoils are selected by their subsequent alpha decay in the DSSSD. A Gaussian fit of the form shown in equation 5.4 is made to the experimental data (solid green line). As almost all transitions in ^{178}Pt are expected to occur before the reset foil this fit represents the low charge component in the CSD.

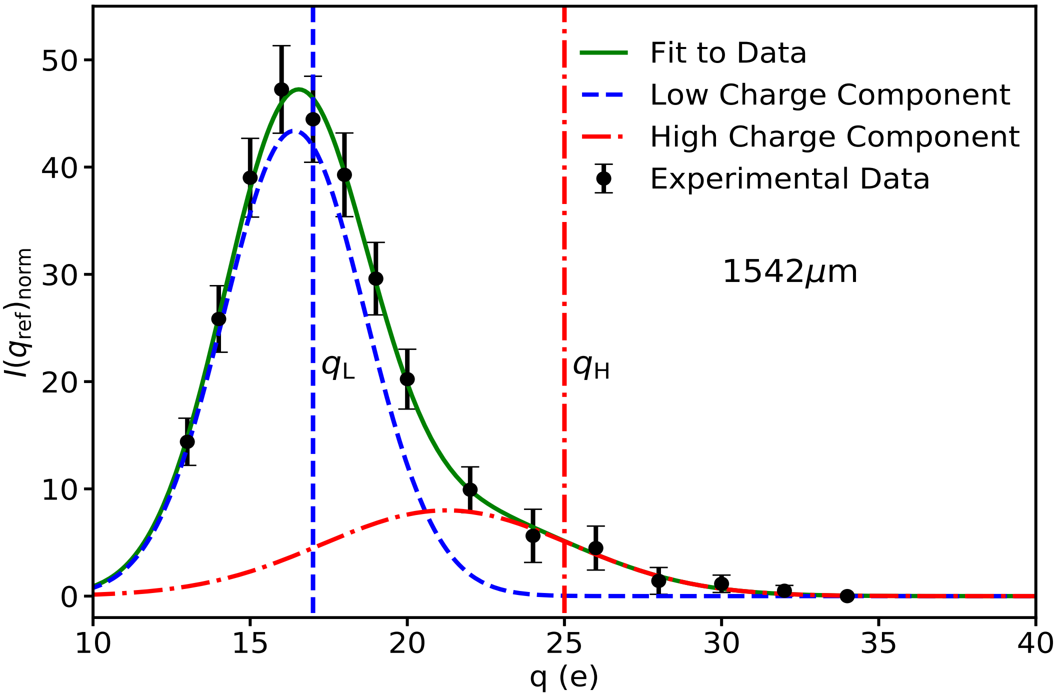

Figure 5.9: Charge-state distribution for ^{178}Pt recoils at target-to-reset foil distance x =1542 µm. The recoils are selected by their subsequent alpha decay in the DSSSD. As the $2_1^+ \rightarrow 0_1^+$ 170 keV transition is expected to occur after the reset foil, a two-component convolved Gaussian fit is made to the experimental data (solid green line). These components represent the low charge (blue dashed line) and first-high charge (red dot-dashed line) components in the CSD.

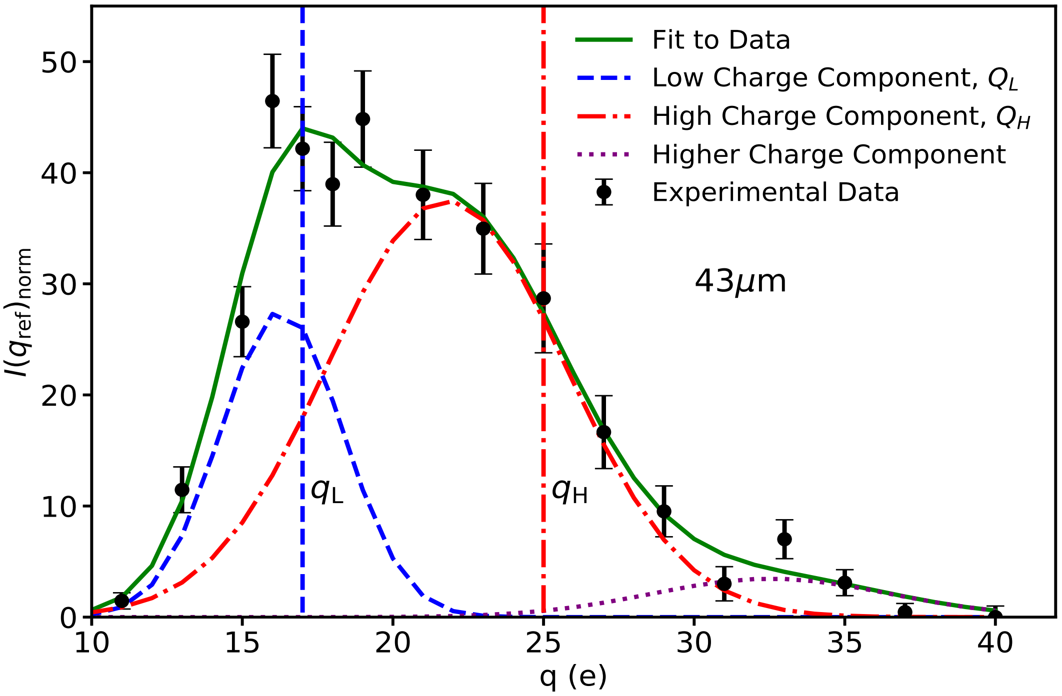

Figure 5.10: Charge-state distribution for ^{178}Pt recoils at target-to-reset foil distance x =43 µm. The recoils are selected by their subsequent alpha decay in the DSSSD. A three-component Gaussian fit is applied to the data (solid green line). The centres and widths of the Q_L (blue dashed line) and Q_H (red dot-dashed line) components are kept fixed using average values from the CSD scans at x =5061 µm and 1543 µm (see figs. 5.8, 5.9 and table 5.3). A higher-charge component is clearly visible (purple dotted line).

Table 5.3: Summary of Gaussian fit parameters for ^{178}Pt CSD spectra at x =5061 µm, 1543 µm and 43 µm.

		Target-to-reset foil distance			
	Parameter	5061 µm	1543 µm	Average	43 µm
Q_L	a	61(4)	43(4)	-	28(30)
	μ (e)	16.4(1)	16.4(1)	16.4(1)	16.3(5)
	σ (e)	2.38(15)	2.25(12)	2.30(9)	2.03(100)
Q_H	a	-	8(2)	-	38(7)
	μ (e)	-	21.2(21)	21.2(21)	21.8(21)
	σ (e)	-	3.95(76)	3.95(76)	3.93(295)
Q_{2H}	a	-	-	-	3(5)
	μ (e)	-	-	-	32.5(134)
	σ (e)	-	-	-	4(10)

^{178}Pt ions at target-to-reset foil distances x =5061 µm, 1542 µm and 43 µm are shown in figs. 5.8, 5.9 and 5.10, respectively.

Based on previous lifetime studies, at x =5061 µm almost all transitions in ^{178}Pt are expected to occur before the charge reset foil and only a low charge component (Q_L) should be present in the CSD. Therefore a single Gaussian distribution is fit using a least-squares fitting routine to the experimental data [New21]. The distribution has the form,

$$F(q) = a\exp\left(-\frac{(q-\mu)}{2\sigma^2}\right) \tag{5.4}$$

where a is the amplitude of the Gaussian peak, μ is the mean charge value, and σ is the width of the distribution. The result of the fit is shown as a solid green line in fig. 5.8.

At x =1543 µm a significant proportion of the $2_1^+ \rightarrow 0_1^+$ 170 keV transition is expected to occur after the reset foil. At this distance a two-component convolved Gaussian fit is made to the experimental data. The fit is shown as a solid green line in fig. 5.9, along with the convolved components, shown as a blue dashed and red dot-dashed line, which represent the low and first-high charge (Q_H) components respectively.

At x =43 µm even higher charge components are expected to contribute to the CSD. At this distance a three-component convolved Gaussian fit is applied to the experimental data. However, due to the number of degrees of freedom in the fit, the best-fit parameters have large errors. To reduce these errors the centres and widths of Q_L and Q_H are allowed to vary by only 3 standard deviations of the average value obtained from the fits performed at x =5061 µm and 1543 µm. When applying the fit in this way a third component is visible within the CSD. Table 5.3 summarises the values for the Gaussian parameters obtained from these fits. Even with the constraints placed on the Q_L and Q_H parameters there are large errors in the best-fit parameters. However, this still validates that at smaller target-to-reset foil distances higher charge components are visible in the CSD as expected.

Using the CSD scans in figs. 5.8, 5.9 and 5.10, two charge states were chosen to represent Q_{L} ($q_{\mathrm{ref}} = 17\mathrm{e}$) and Q_{H} ($q_{\mathrm{ref}} = 25\mathrm{e}$) respectively. These charge states are indicated in each scan as vertical blue dashed and red dot-dashed lines respectively. These charge states were chosen to maximise the intensity of the component of interest whilst also minimising the intensity from overlapping charge components. As previously mentioned, for each plunger run, data were collected using MARA settings corresponding to these reference charge states.

5.6 DDCM analysis

To measure the lifetime of the 2_1^+ state in ^{178}Pt using a DDCM coincidence analysis, recoils are selected in coincidence with a measured γ ray from the $4_1^+ \rightarrow 2_1^+$ 257 keV direct feeding transition. Fig. 5.11 shows part of an example 2D histogram of recoil m/q value against energy deposited in JUROGAM 3 for γ rays in coincidence with a recoil detected at the focal plane of MARA during the $x = 43$ µm, $q_{\mathrm{ref}} = 17\,e$ plunger run.

A similar process to that described in section 5.5 was used to find the m/q spectrum of recoils in coincidence with the $4_1^+ \rightarrow 2_1^+$ 257 keV transition. A gate is set to only integrate counts that fall within the energy range $254 \leq E_\gamma \leq 258$ keV. This is shown as a lighter shaded region in fig. 5.11. As in the CSD scan, a separate gate, shown as a darker shaded region in fig. 5.11, is set to integrate counts in the energy range $246 \leq E_\gamma \leq 250$ keV. This is used to estimate the number of background counts that arise as random coincidences. The background gate was chosen at this energy as it lies close to the 257 keV transition but does not show any γ-ray peaks in the γ-recoil JUROGAM 3 energy spectrum (fig. 5.4).

The counts inside each of these shaded regions were integrated along the γ-ray energy axis to find their projection on to the m/q axis. Equation 5.2 was used to find the resulting m/q spectrum. Fig. 5.12 shows the resulting m/q spectrum for each target-to-reset foil distance at both $q_{\mathrm{ref}} = 17\,e$ and $q_{\mathrm{ref}} = 25\,e$. The transmission through MARA is largest for the reference charge state, q_{ref}, therefore the intensity of high and low charge ions, I_H and I_L respectively,

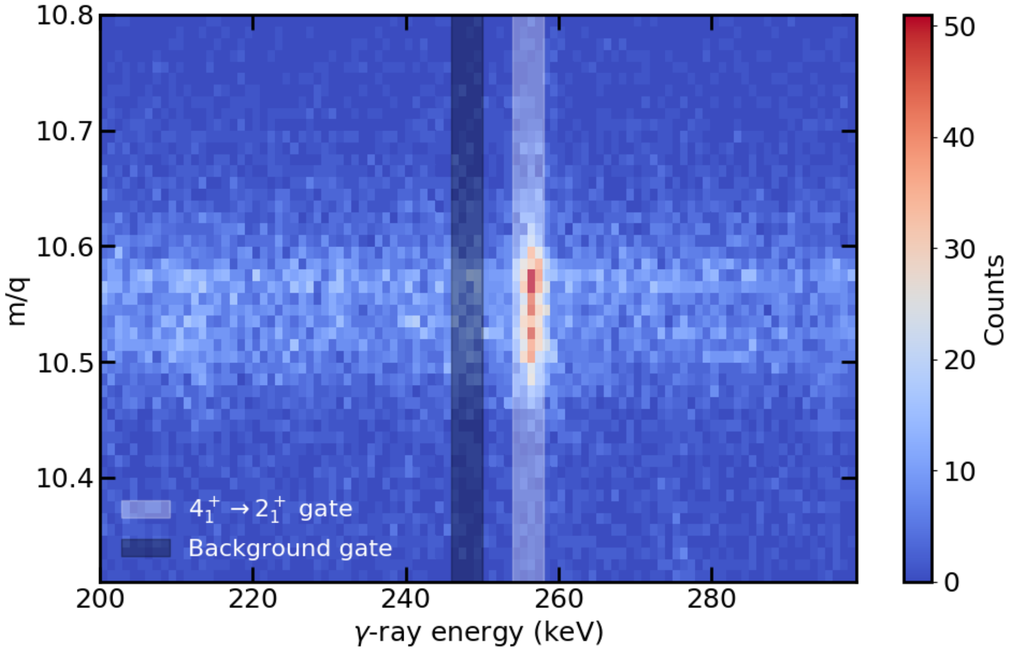

Figure 5.11: Example 2D spectrum of m/q against γ-ray energy taken at target-to-reset foil distance $x = 43$µm. The reference charge is $q_{\text{ref}} = 17\,e$. The lighter shaded region defines a gate set on events in the energy range $254 \leq E_\gamma \leq 258$, whilst the darker shaded region defines a background gate.

were measured by integrating the counts in the normalised charge spectra for the central charge state only. The limits for the integration are shown in fig. 5.12 as dotted lines. The relative intensity of high ($R_H = \frac{I_H}{I_L+I_H}$) and low ($R_L = \frac{I_L}{I_L+I_H}$) charge ions were used in the DDCM equations, given in section 3.3 (equations 3.24 and 3.25), to find the relative intensity of $2_1^+ \rightarrow 0_1^+$ transitions occurring after (R_A) and before (R_B) the reset foil, respectively. The values of R_B and R_A are shown in fig. 5.15(a) and (b), respectively.

The DDCM lifetime equation (see section 3.3, equation 3.19) requires that the coincidence gate is set on feeding transitions occurring before the reset foil. The $4_1^+ \rightarrow 2_1^+$ transition at 257 keV is shown in fig. 5.13 for target-to-reset foil distances $x = 43$ µm and $x = 5061$ µm. At these distances all the transitions are expected to occur after and before the charge reset foil, respectively. As recoils pass through the reset foil they will slow down resulting in a smaller Doppler shift in γ-ray energy, and thus a different energy centroid. Gaussian fits, shown in fig. 5.13, were applied to the $4_1^+ \rightarrow 2_1^+$ peak at both distances. The measured centroids of both Gaussian distributions were $256.54(6)$ keV (43 µm) and $256.74(5)$ keV (5061 µm). The change in the energy centroid, $\Delta E = 0.20(9)$ keV, is much smaller than the full width half maximum (FWHM) of each peak, $3.3(1)$ keV (43 µm) and $3.5(1)$ keV (5061 µm). This meant that it was not possible to set a gate solely on feeding transitions occurring before the reset foil.

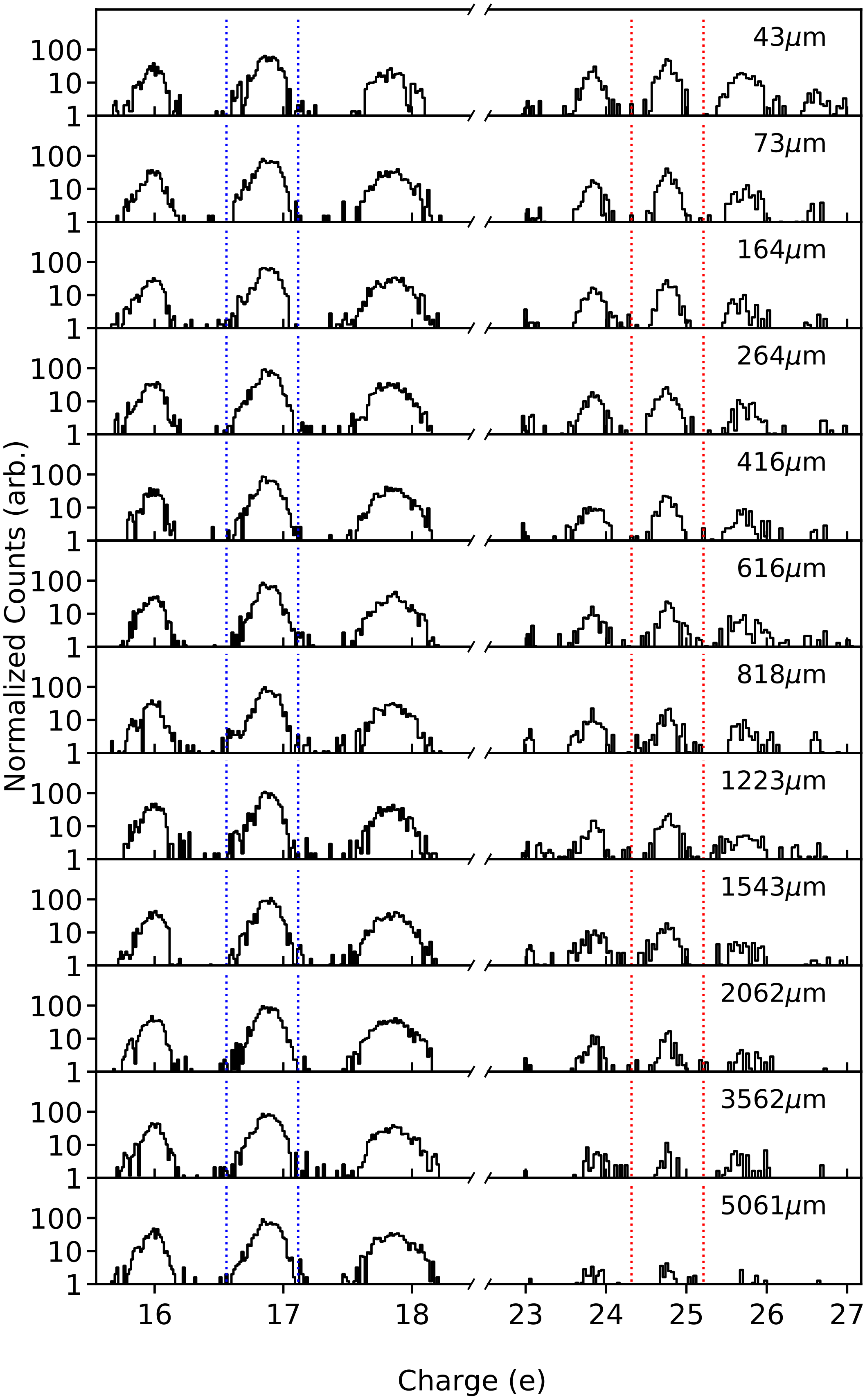

Figure 5.12: Charge spectra at the focal plane of MARA when gating on the $4_1^+ \rightarrow 2_1^+$ transition at 257 keV. In each spectrum counts have been normalised using Coulomb excitation in the target. The central peaks lie at 17e and 25e. The evolution with distance of low and high charge components is shown for all distances. The integration limits of the central charge peaks are shown as blue ($q = 17\,\mathrm{e}$) and red ($q = 25\,\mathrm{e}$) dotted lines.

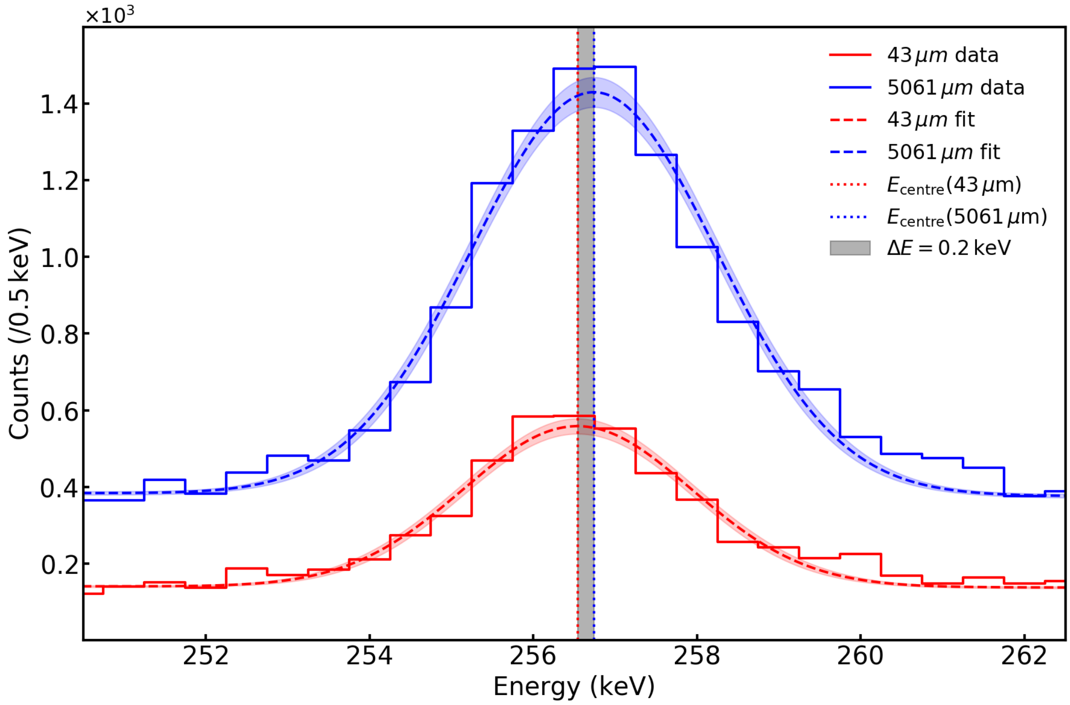

Figure 5.13: Part of the JUROGAM 3 spectrum showing the $4_1^+ \rightarrow 2_1^+$ 257 keV transition for target-to-reset foil distances x =5061 µm and x =43 µm.

Using the unresolved Doppler-shifted components method (UDCM) [Bar20a] it was possible to measure the proportional intensity of $4_1^+ \rightarrow 2_1^+$ transitions occurring before (I_b) and after (I_a) the foil. In the UDCM the components of a γ-ray transition can be characterised by two convolved Gaussian distributions with centroids $\mu_{\mathrm{b,a}}$, widths $\sigma_{\mathrm{b,a}}$, and amplitudes $A_{\mathrm{b,a}}$. In the case that $|\mu_{\mathrm{b}} - \mu_{\mathrm{a}}| << \sigma_{\mathrm{b,a}}$ then for every target-to-reset foil distance, x, a single peak is detected with intensity $I_{\mathrm{tot.}}(x) = I_{\mathrm{b}}(x) + I_{\mathrm{a}}(x)$ and centroid $\langle\mu\rangle(x)$. The intensity of each component is then given by,

$$I_{\mathrm{b}}(x) = I_{\mathrm{tot.}}(x)\left(1 + \frac{\mu_{\mathrm{b}} - \langle\mu\rangle(x)}{\langle\mu\rangle(x) - \mu_{\mathrm{a}}}\right)^{-1} \tag{5.5}$$

$$I_{\mathrm{a}}(x) = I_{\mathrm{tot.}}(x)\left(1 + \frac{\langle\mu\rangle(x) - \mu_{\mathrm{a}}}{\mu_{\mathrm{b}} - \langle\mu\rangle(x)}\right)^{-1} \tag{5.6}$$

where μ_{b} and μ_{a} are obtained by measuring the transition at distances where $x >> \tau \cdot v$ and $x << \tau \cdot v$ respectively, where τ is the lifetime of the depopulated state and v is the velocity of ions between the target and the reset foil.

The relative intensity of $4_1^+ \rightarrow 2_1^+$ transitions occurring after the reset foil is shown in fig. 5.14 against target-to-reset foil distance. The value μ_{a} was measured by bringing the target and reset foils together until electrical contact was achieved. The value μ_{b} was found using the

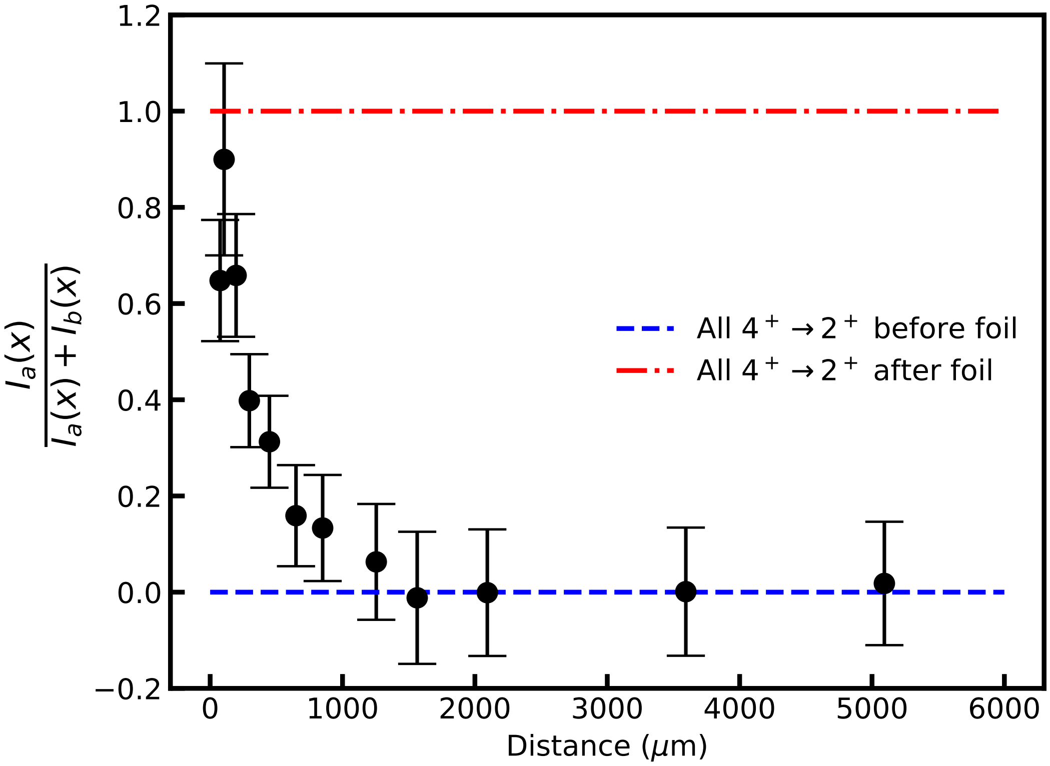

Figure 5.14: Proportional intensity of $4_1^+ \to 2_1^+$ transitions occurring after the reset foil for each target-to-reset foil distance. This was measured by applying the unresolved Doppler-shifted components method (UDCM) [Bar20a]. At distances longer than $x = 1223\,\mu\text{m}$ the proportion of $4_1^+ \to 2_1^+$ transitions occurring after the reset foil is consistent with 0 to within 1σ.

average value of the measured centroid at distances $x > 2000\,\mu\text{m}$. At distances $x \geq 1223\,\mu m$ the proportion of $4_1^+ \to 2_1^+$ transitions occurring after the reset foil is consistent with 0 to within 1σ and the requirement for using the DDCM coincidence analysis is satisfied.

The program `NAPATAU` was used to extract the lifetime of the 2_1^+ state [Sah04]. `NAPATAU` uses equation 3.19 (section 3.3) to extract lifetime information from the data. The program fits a second-degree polynomial, $f(x)$, to the values of R_B at distances chosen by the user (shown in fig. 5.15(a)). In this case the range of distances used were chosen to be sensitive to the lifetime of the 2_1^+ state and with $x \geq 1223\,\mu\text{m}$ to satisfy the requirement that the proportion

Table 5.4: Lifetime values returned by the program `NAPATAU` for the 2_1^+ state in ^{178}Pt at selected target-to-reset foil distances.

Distance (μm)	Lifetime (ps)
1223	431(32)
1543	439(35)
2062	420(42)
3562	429(96)
Average	430(20)

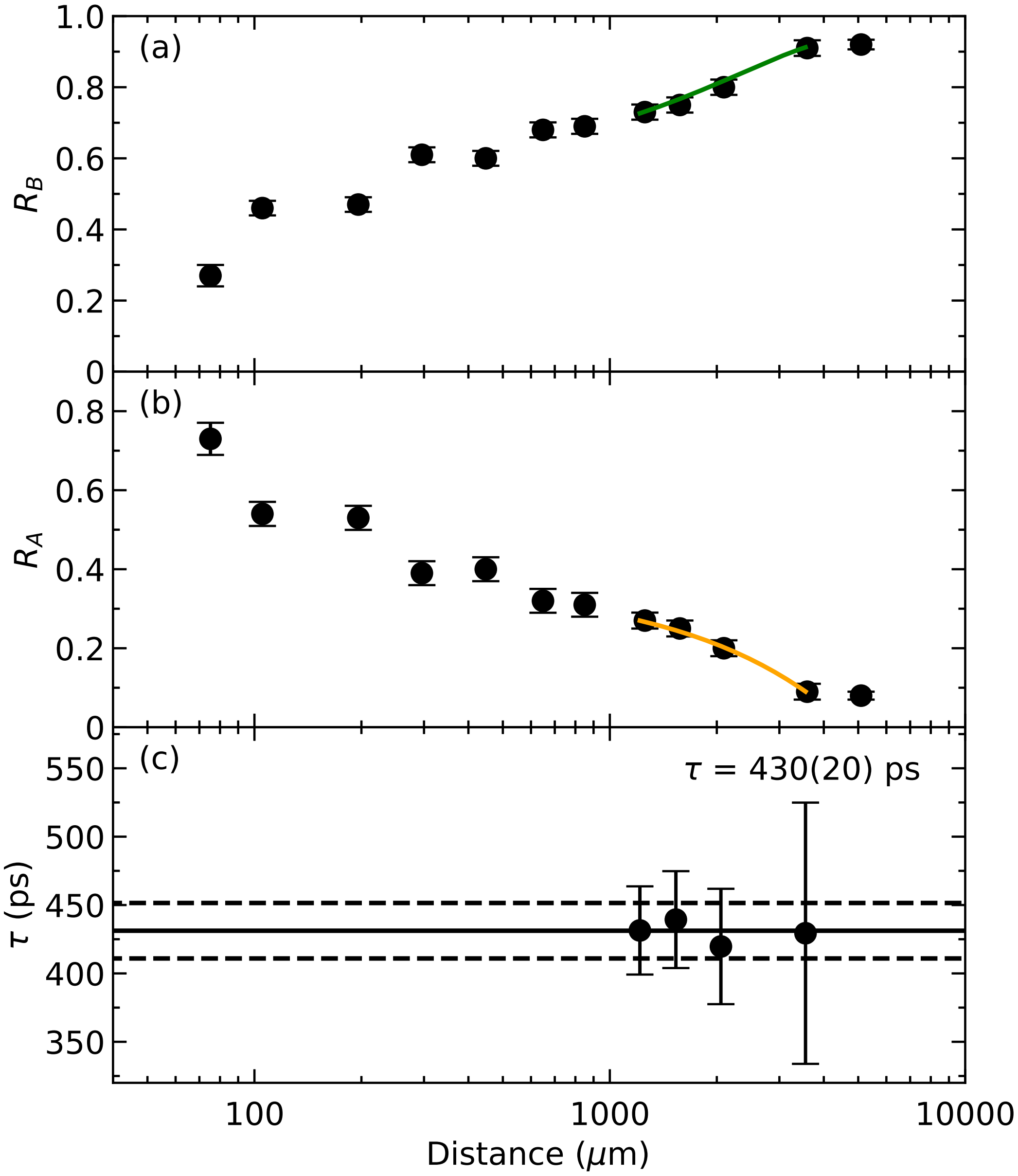

Figure 5.15: Results from the analysis of the normalised charge spectra shown in fig. 5.12 using the program `NAPATAU` [Sah04]. (a) The values R_B are shown with a second degree polynomial $f(x)$ (solid green line) which is fitted to the data. (b) The values R_A are shown along with a function of the form $\tau \cdot v \cdot \frac{df(x)}{dx}$ (solid orange line). (c) The τ-curve of the 2_1^+ state in ^{178}Pt. The weighted average (solid line) of the lifetime found for each distance is shown. The error on the weighted mean is also shown (dashed line).

of $4_1^+ \rightarrow 2_1^+$ occurring after the foil are consistent with 0 (see fig 5.14). The differential of the function $f(x)$ is used in the form $\tau \cdot v \cdot \frac{df(x)}{dx}$ to describe the values R_A (shown in fig. 5.15(b)). A common χ^2 minimisation of $f(x)$ and $\frac{df(x)}{dx}$ is used to find a value for the lifetime at each distance [Dew89]. Fig. 5.15(c) shows the resulting τ-curve for the 2_1^+ state in ^{178}Pt. The lifetime values calculated at each selected distance are given in table 5.4. A weighted average gives a lifetime of $\tau(2_1^+) = 430(20)$ ps.

5.7 Bateman analysis

An alternative method of obtaining lifetime information is to model the CSD spectra using the Bateman equation to describe the de-excitation of states in the ^{178}Pt ground-state band. Recoil-alpha coincidences in the DSSSD (see fig. 5.3) were used to select ^{178}Pt recoils. The resulting normalised charge spectra are shown in fig. 5.16 for all distances. The intensities of the low (I_L) and high (I_H) charge states were measured by integrating the counts in the central charge peak. The limits of integration are shown as dotted lines.

Fig. 5.17 shows the relative intensity of the high charge state $R_H = \frac{I_H}{I_L+I_H}$ against target-to-reset foil distance. At the distances $x \leq 290\,\mu$m the proportion of high charged ions increases rapidly. There are two possible explanations for this. Firstly, there could be highly converted side-feeding transitions that populate the ground-state band. In this case the change in intensity of highly charged ions detected after the reset foil will reflect the lifetime of these side-feeding transitions. This is unlikely, however, as only a small population of bands other than the ground-state band was observed. Additionally, side-feeding from statistical γ rays usually proceeds through high-energy, low angular momentum transitions which have almost negligible internal conversion.

The second, more likely, possibility is that at low distances there will be a significant intensity of a second-high charge component (2 internal conversions after the reset foil). A second-high charge component was observed with a significant intensity in the CSD scan at $x =$43 µm (see fig. 5.10). As only the intensity of charge states corresponding to the low and first-high charge component were measured, the effect of this second-high charge component is ignored. If the intensity of a charge state corresponding to the second-high charge state (I_{2H}) had been measured, then the relative intensity of the high charge state would be $R_H = \frac{I_H}{I_L+I_H+I_{2H}}$. The effect would become negligible at longer distances where $I_{2H} \approx 0$, as can be seen in the CSD scan at $x =$1543 µm. The effect can be estimated using the CSD scan at $x =$43 µm. The normalised intensity at the charge states chosen to represent the different charge components are $I(17\,e) = 46.2(38)$, $I(25\,e) = 28.7(49)$ and $I(33\,e) = 7.0(18)$, where the charge state 33 e has been chosen to represent the second-high charge state. The relative intensity of the high charge state reduces by $8.6^{+24.4}_{-8.6}\%$ when the intensity of the second-high charge state is accounted for. The lower limit on this value is subject to the requirement that $I_{2H} \geq 0$. This correction factor was applied to the data point at $x =$43 µm and is shown in magenta on fig. 5.17. To within 1σ error, the value of R_H at target-to-reset foil distance 43 µm could be reduced significantly when the intensity of the second-high charge state is

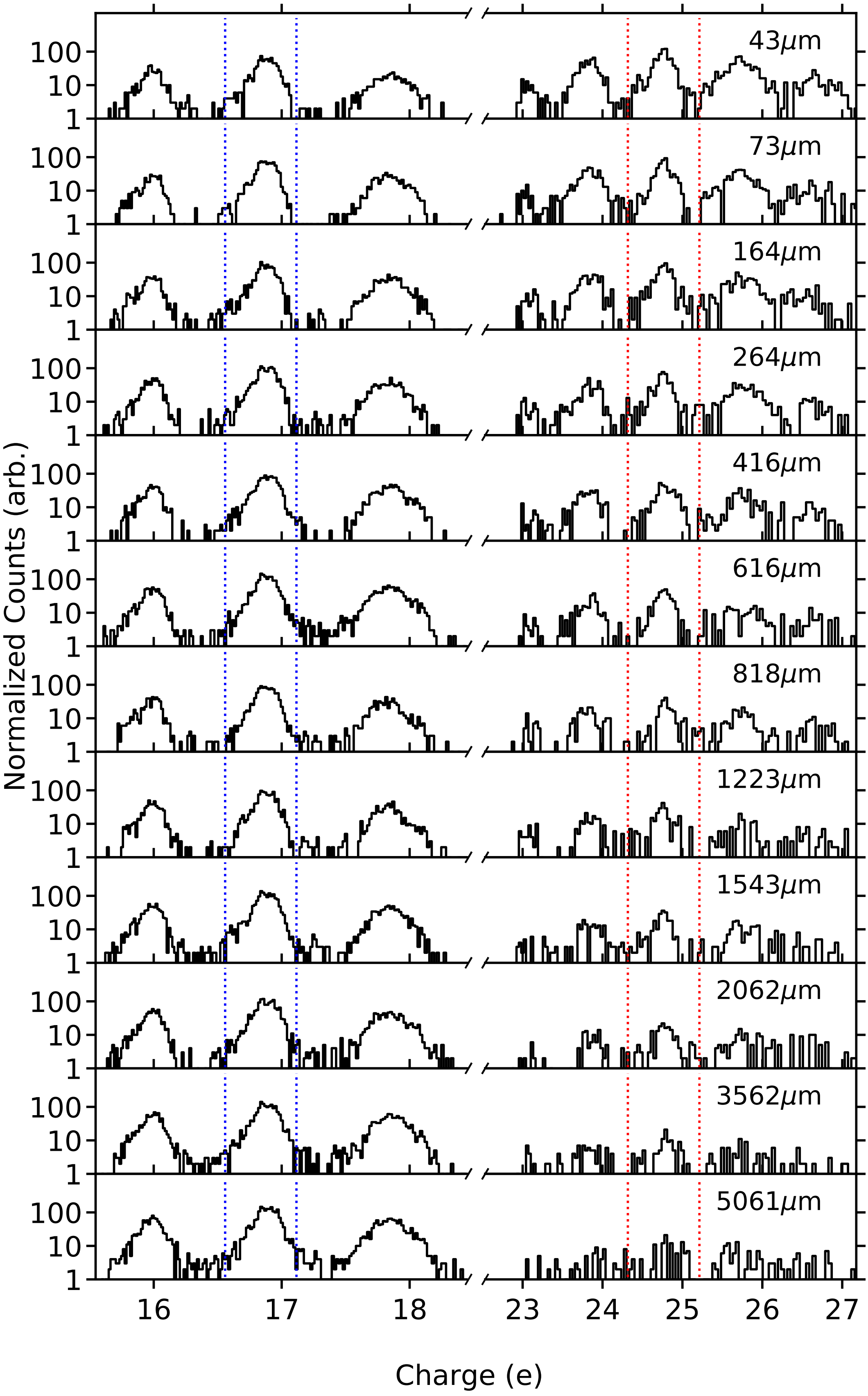

Figure 5.16: Charge spectra at the focal plane of MARA in coincidence with an alpha decay of ^{178}Pt. Normalization is the same as in fig. 5.12. The evolution with distance of low and high charge components is shown for all distances. The integration limits of the central charge peaks are shown as blue ($q = 17\,\mathrm{e}$) and red ($q = 25\,\mathrm{e}$) dotted lines.

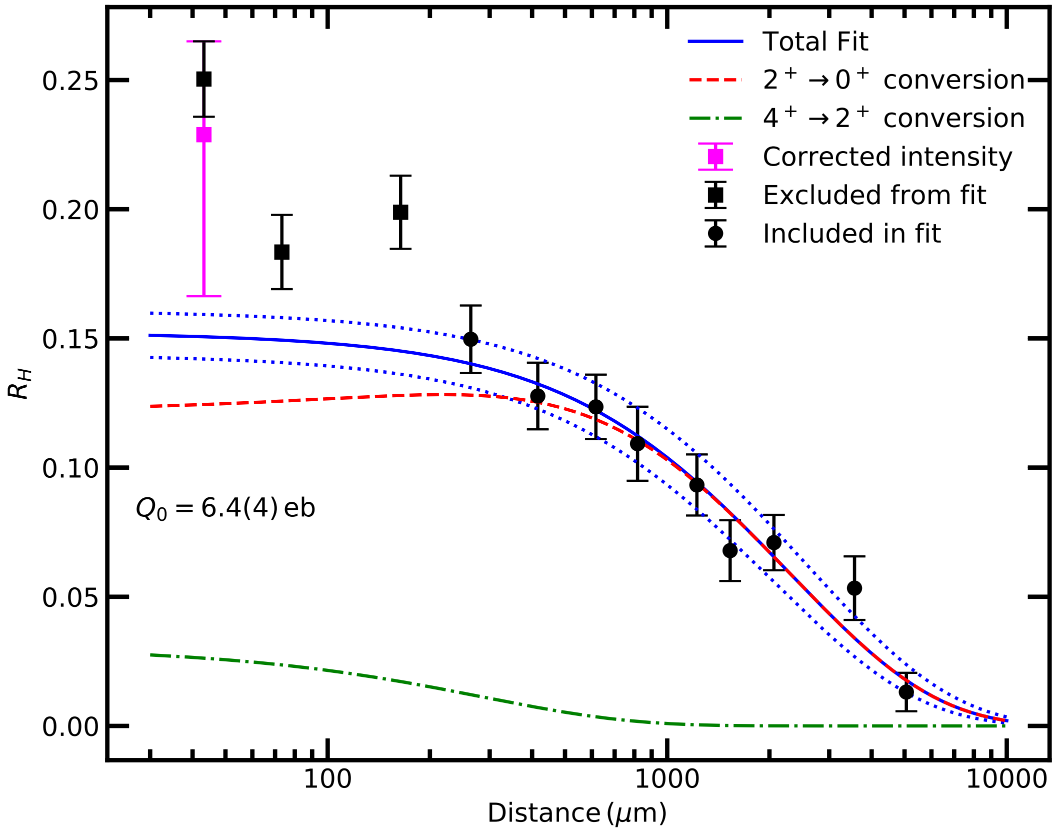

Figure 5.17: The relative intensity of highly charged ions detected at the focal plane as a function of target-to-reset foil distance. The solid (blue) line is the result of fitting a two-state model, described in section 3.4.1, to the data (circles). The lifetimes of the two states are described by a single quadrupole moment, as defined in equation 3.57. Data points below 264 µm (squares) were left out of the fit (see text). The dashed (red) and dot-dashed (green) lines represent the contribution to the high charge component from internal conversion of the $2_1^+ \rightarrow 0_1^+$ or $4_1^+ \rightarrow 2_1^+$ transitions respectively. The dotted line (blue) is the 1σ error on the fit. The magenta data point at $x = 43$ µm is the value R_H when a correction factor is applied to account for the non-zero intensity of the second-high charge state (see text).

accounted for.

A two-state fit of the form described in section 3.4.1 is made to the data points at distances $x \geq 264$ µm. In this model the first excited level corresponds to the 2_1^+ state; the second excited level accounts for the average de-excitation properties of all higher-energy states but is dominated by the lifetime of the 4_1^+ state. This model assumes that the 2_1^+ state is populated solely through the $4_1^+ \rightarrow 2_1^+$ transition. This assumption is validated through a comparison of the 170 keV and 257 keV γ ray intensities, accounting for the internal conversion coefficients of the transition and the efficiency of JUROGAM 3 at these energies. The intensities are equal to within 1σ. To minimise the number of free parameters in the fit, the assumption is made that the rotational band is described by a single quadrupole moment Q_0, with units eb, and the lifetime of each state is defined by equation 3.57. This assumption is justified by the experimental results in ref. [Fra19] which show a constant quadrupole moment within the

Table 5.5: Contributions from different sources of systematic error to final uncertainty in $\tau(2^+)$ and $\tau(4^+)$ for the Bateman analysis. Each error contribution was varied by $\pm 1\sigma$.

Parameter	Value(error)	$\sigma_{\tau(2^+)}$ (ps)	$\sigma_{\tau(4^+)}$ (ps)
$\alpha(2^+ \to 0^+)$	$0.63(1)$	0.6	0.3
$\alpha(4^+ \to 2^+)$	$0.1578(23)$	0.2	0.1
Average recoil velocity, $\beta = v/c$	$0.0177(2)$	4.9	0.6
Target-to-reset foil offset	$8(1)$ µm	0.02	0.003
Total systematic error	-	4.9	0.7

yrast band down to the ground state for ^{178}Pt. The fit, shown in fig. 5.17, gives a quadrupole moment of $Q_0 = 6.4(4)$ eb which corresponds to lifetime values of $\tau(2^+) = 430(50)$ ps and $\tau(4^+) = 54(6)$ ps.

Table 5.5 shows the uncertainty contribution from systematic errors in internal conversion coefficients, average velocity of recoils and the target-to-reset foil offset value. These values were determined by varying each parameter by $\pm 1\sigma$ in the fit. The total systematic error contribution amounts to 1.2% for $\tau(2^+)$ and 1.3% for $\tau(4^+)$, whilst the statistical error is 11%.

As the charge plunger method relies on the internal conversion effect, it is important to estimate the systematic error arising from having no knowledge of internal conversion coefficients, where often only theoretical calculations exist. For the $2^+_1 \to 0^+_1$ transition, it is imperative to have good knowledge of the coefficient as the data points lie in a target-to-reset foil distance range which is sensitive to the lifetime of the 2^+_1 state. To estimate the systematic error arising from having no knowledge of the $4^+_1 \to 2^+_1$ internal conversion coefficient, the value $\alpha(4^+ \to 2^+_1)$ used in the fit is varied between 0 and ∞. This results in an error on $\tau(2^+_1)$ of $\sim 3.7\%$.

Table 5.6 summarises the lifetime measurements of the 2^+_1 and 4^+_1 states from previous measurements and from this work for both the DDCM coincidence and Bateman analysis. There is a clear agreement between the 2^+_1 lifetime values obtained in this work and previous studies. The lifetime measurement for the 4^+_1 state agrees with the value given by Dracoulis et al. and is consistent to within 2.21σ with the value that Fransen et al. give. A further comparison between the results is given in section 6.1.

Table 5.6: Lifetime of excited states in ^{178}Pt deduced from the DDCM coincidence analysis and from the Bateman fits. Previous measurements of the lifetime of the 2_1^+ and 4_1^+ states are also given.

Analysis Method	2_1^+ lifetime (ps)	4_1^+ lifetime (ps)
DDCM coincidence	430(20)	-
Two-state Bateman	430(50)	54(6)
Li et al. [Li14]	412(30)	-
Fransen et al. [Fra19]	445(100)	41(2)
Dracoulis et al. [Dra86]	-	54(5)

Chapter 6

Discussion and Future Work

6.1 Comparison to previous studies

The results of this work will be discussed here within the context of the previous studies measuring the lifetime of excited states in ^{178}Pt. The results of previous studies are given in table 5.6 and the methods they used will be briefly covered. In ref. [Dra86], Dracoulis et al. used the RDDS technique with γ-ray events in singles mode, i.e. γ-γ coincidences were not employed. Using this method they were able to measure the lifetime of the 4_1^+, 6_1^+ and 8_1^+ states. However, these were not independent measurements as the lifetime measurements of the low-lying states were dependent on the measured decay curves of high-lying states. In ref. [Li14], Li et al. used triple-γ coincidences with LaBr$_3$(Ce) and HPGe detectors to perform fast-timing techniques to measure the lifetime of the 2_1^+ state. Whilst this method is able to obtain lifetime information with errors similar to that from the RDDS technique, it relies on the ability to perform a triple-γ coincidence analysis, which may only be possible for the strongest transitions. Finally, in ref. [Fra19], Fransen et al. used the RDDS technique to perform the DDCM with γ-γ coincidences to obtain independent lifetime measurements of the 4_1^+, 6_1^+, 8_1^+ and 10_1^+ states. However, they were only able to quote a lifetime for the 2_1^+ state with an error of 22%.

Fig. 6.1 shows data from all the lifetime measurements of the 2_1^+ state in ^{178}Pt, including the DDCM and Bateman results from this work. The lifetime measurement of the 2_1^+ state in this work clearly agrees with those from previous works. This establishes the charge plunger method, used with a recoil separator and focal plane detection system, as a viable option for performing lifetime measurements on states that de-excite with relatively large internal

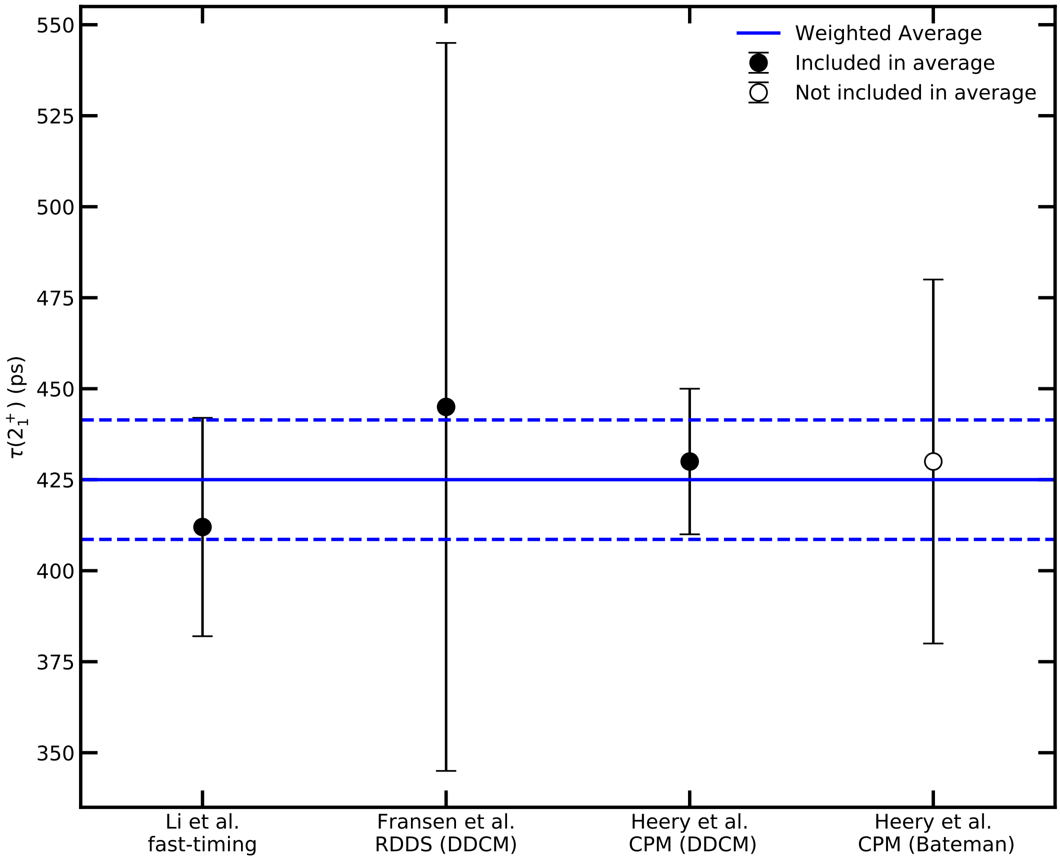

Figure 6.1: Compiled results for lifetime measurements of the 2_1^+ state in ^{178}Pt [Li14, Fra19, Hee21]. The results for both the DDCM and Bateman analysis from this work are included. A weighted average gives $\tau(2_1^+)$ =425(16) ps. The Bateman analysis has not been included in the average.

conversion coefficients. As shown by the measurement from Fransen et al., it is difficult to obtain a precise lifetime value for the 2_1^+ state in ^{178}Pt using the standard RDDS technique due to both the relatively large internal conversion coefficient for the $2_1^+ \rightarrow 0_1^+$ transition and the unfavourable kinematics for asymmetric reactions which produce recoiling nuclei at a slow mean velocity. A weighted average of all the data, except for that obtained with a Bateman analysis, shown in fig. 6.1 gives a lifetime value of $\tau(2_1^+)$ =425(16) ps. The Bateman measurement has not been included in the weighted average in order to not bias the result towards this work.

A lifetime is also obtained for the 4_1^+ state using the Bateman analysis. The true lifetime of the 4_1^+ state will in fact be shorter than the value given here since only a two-state system is used and the lifetime of higher energy excited states are not considered. The value is also dependent on the assumption of a rigid-rotor model for ^{178}Pt which allows for the lifetime of excited states in the rotational band to be contained within a single parameter, the quadrupole moment. Since more data points were taken at longer target-to-reset foil distances, the fit of the quadrupole moment will be more sensitive to the lifetime of the 2_1^+ state. However,

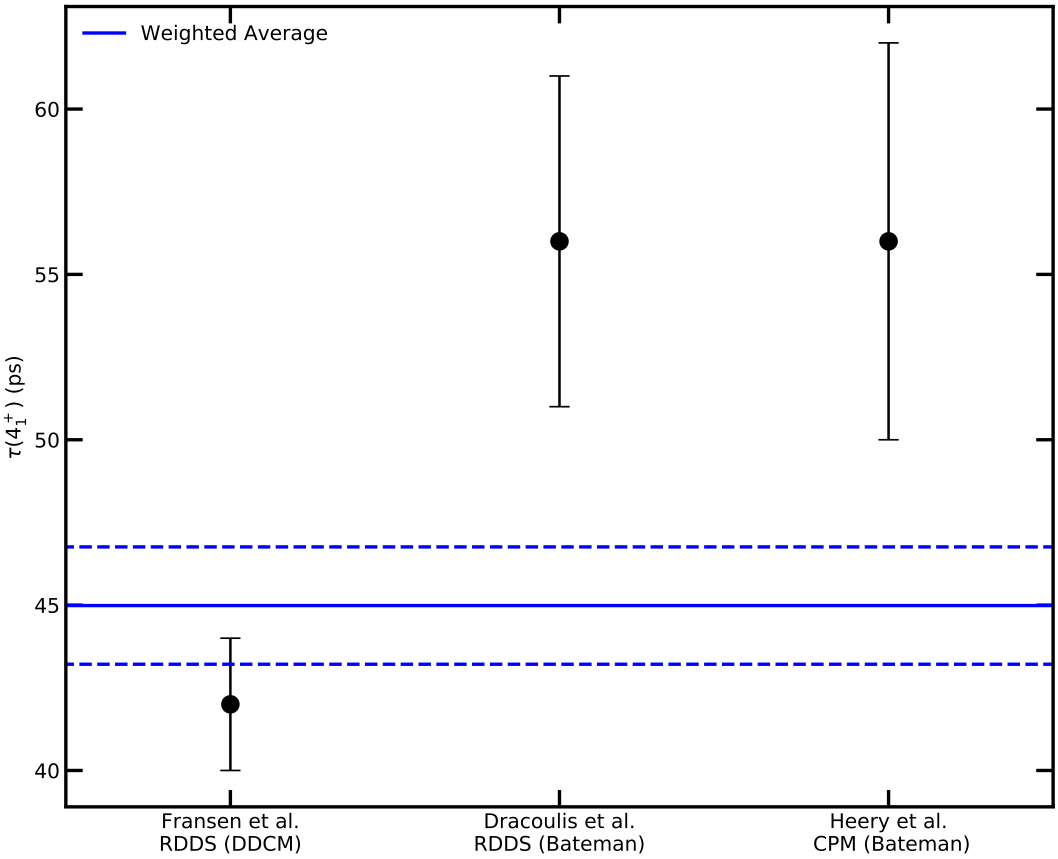

Figure 6.2: Compiled results for lifetime measurements of the 4_1^+ state in ^{178}Pt [Fra19, Dra86, Hee21]. The results for the Bateman analysis from this work are included. A weighted average gives $\tau(4_1^+)$ =45(2) ps.

the lifetime given here agrees to within 2.21σ of the value given by Fransen et al., which is an independent lifetime measurement obtained using the DDCM coincidence method, and is very similar to that obtained using γ-ray singles, given by Dracoulis et al., with a similar error. This suggests that the charge plunger method is vulnerable to the same effects as γ-ray singles measurements. Fig. 6.2 shows all the lifetime measurements of the 4_1^+ in ^{178}Pt, including the Bateman results from this work. A weighted average gives $\tau(4_1^+)$ =45(2) ps. However, it is worth noting that the result from Fransen et al. is a more accurate measurement due to the advantages that the DDCM has over a Bateman analysis, as will be explained in the next section.

6.2 Comparison of Bateman and DDCM analysis

Whilst the value for the 2_1^+ lifetime obtained from the Bateman analysis agrees with the result obtained using the DDCM coincidence analysis and the value given by Li et al., the uncertainty is more than twice that in the DDCM analysis. This is because a DDCM analysis has significant advantages over a Bateman analysis for retrieving lifetime information (see section 3.1).

Firstly, the DDCM is independent of absolute distances between the target and reset-foil, and instead only the relative distances are needed. This means the method is independent of the offset between the foils which can cause an error when analysing the data using a Bateman fit. This, however, will not have such a large effect on the lifetime measurements in this work, as the target-to-reset foil separation distances used were large in comparison to the measured offset. Additionally, the capacitance feedback method limits the variation in foil separation due to heating from the beam.

Secondly, when applying a Bateman fit to the data, there is a dependence on the de-excitation properties of states feeding the level of interest (directly or indirectly). If the de-excitation properties of these feeding states are unknown then they must be included in the fit as free parameters which will introduce more uncertainty in to the final result. In this work it was possible to reduce the number of free parameters by assuming a rigid-rotor model for the nucleus. However, this assumption may not always be valid. A DDCM analysis uses only experimentally accessible variables to obtain a lifetime value.

Additionally, the DDCM becomes an even more favourable method when a γ-ray coincidence gate can be applied to the feeding transition occurring before the reset foil. A γ-ray coincidence gate also removes any systematic error arising from side-feeding.

However, in the charge plunger method, only a DDCM coincidence analysis can be performed. In the conventional recoil distance Doppler-shift (RDDS) technique, where γ ray detection is used to perform a lifetime measurement, the DDCM can be performed using γ-ray singles (DDCM singles) or γ-γ coincidences (DDCM coincidences) analysis. In the DDCM singles analysis framework (see section 3.1.2), one is required to have knowledge of the intensities (before and after the reset foil) from all possible feeding transitions to the level of interest. This is possible when detecting γ rays, since specific transitions can be directly observed and their intensity measured. However, in the charge plunger method, where the measured experimental quantities are the intensities of the different components present in the CSD of recoiling ions, it is not possible to directly determine the intensities of transitions feeding the level of interest. Instead, transition intensities are only inferred from the CSD and the situation becomes complicated when more than one transition feeds the level of interest. Therefore, in general, the DDCM singles cannot be used with the charge plunger method. The consequence of this is that γ-ray-recoil coincidences are required in order to perform a DDCM (coincidence) analysis with the charge plunger method.

A further drawback in performing the DDCM coincidence analysis is the requirement that a gate is set on the feeding transition occurring before the reset foil. In both this work [Hee21] and in ref. [Bar20b], there was only a small change in recoil velocity after passing through the reset foil. This was because the recoils were produced with a relatively slow mean velocity ($v/c = 1.77(2)\%$), and a thin reset foil was necessary to keep an acceptable transmission of ions through the recoil mass separator. The result of this was that the change in the Doppler shift of γ rays emitted before and after the reset foil was much smaller than the resolution of the JUROGAM 3 detectors. Therefore, it was not possible to resolve different Doppler-shifted peaks in the γ-ray spectrum, thus limiting the available data to distances where the feeding transition always occurred before the reset foil (see fig. 5.17).

6.3 Planning charge plunger experiments

Many aspects must be considered when planning a nuclear physics experiment at an accelerator facility. Below are few considerations specific to a charge plunger experiment.

6.3.1 Charge reset foil

Due to the reaction kinematics involved in asymmetric fusion-evaporation reactions of the type employed in this experiment, nuclei are often produced with slow mean recoil velocity. For recoils to have an acceptable transmission through MARA, travel through the focal plane MWPC and then implant into the DSSSD, they must have sufficient energy after the reset foil [Sar08]. For this reason a thin $0.29\,\mathrm{mg/cm^2}$ Ni foil was used for the charge reset in this experiment. Nickel was a suitable material to use for the reset foil as it has a relatively small atomic number and therefore causes less scatter and energy loss of beam and fusion-evaporation particles. Nickel foils are also suitable for plunger experiments as they are flexible and can be easily stretched [Gal70].

In the setup of the first charge plunger experiments in the 1970s, thin carbon foils ($3(1)\,\mathrm{\mu g/cm^2}$) were used to provide a charge reset [Ulf78]. Carbon foils have good electrical and thermal conductivities and their low atomic number minimises the energy loss of recoils in the foil [Tor19]. Carbon foils are also useful as they can be produced very thin ($\sim\mathrm{\mu g/cm^2}$) and the charge state distribution of ions passing through them can be well estimated by empirical formulae [Nik68, Sch01]. However, carbon foils have short lifetimes when exposed to heavy ion beam radiation [Tor19, Kor17]. The thin carbon charge reset foil used in the early charge plunger experiments had to be replaced after every plunger run. Another issue particularly related to plunger experiments is that when heavy ions pass through a carbon foil, they cause significant damage to the crystalline structure of the foil. This causes 'wrinkles' in the carbon foil with heights of $\sim$10 µm and is an effect that cannot be reduced by decreasing the beam current or wobbling the beam [Fra21]. Another consideration is that very thin amorphous carbon foils are not stretchable, a property which is desirable when small target-to-reset foil separations distances are required.

A current area of interest is the use of graphene foils. These are more stretchable than amorphous carbon and have superior mechanical and thermal properties [Kor17]. For example, when subjected to an ion beam, they are estimated to have up to four times longer durability than conventional carbon foils [Pav12]. Currently the application of these foils has been as stripper foils. However, they may prove to be suitable for use as charge reset foils. First tests have been taken and show encouraging results with respect to the intensity of beam which can be impinged on the foil [MG21b].

6.3.2 Charge state distribution scan

Despite the large cross section for the $^{152}\mathrm{Sm}(^{32}\mathrm{S}, 6\mathrm{n})^{178}\mathrm{Pt}$ reaction at 192 MeV, performing a full scan of the CSD for each plunger distance would be inefficient. Instead an initial scan of the CSD was performed to identify the locations of the different charge components, and two charge states ($q_{\mathrm{ref}} = 17\,e$ and $q_{\mathrm{ref}} = 25\,e$) were chosen to represent the intensities of the low and high charge components present. For each plunger distance data were collected at these two charge states only.

However, as suggested in section 5.7, at short distances a significant intensity in the second-high charge component could affect the Bateman fit. At these distances it would have been suitable to collect data at a charge state corresponding to the second high charge state as well. During the scan of the CSD at target-to-reset foil distance $x = 43$ µm (see fig. 5.10), a second-high charge component is present. In future experiments, if higher charge components are identified during a CSD scan, then care should be taken to understand how their presence will affect the results of a Bateman analysis.

There was very little overlap from the low charge component into the charge state $q = 25\,e$ and, at longer distances, the charge state at $q = 17\,e$ is dominated by the low charge component. This was confirmed by the two-component Gaussian fit of the CSD scan at $x = 1543$ μm. Due to this small overlap, it is possible to approximate the relative intensities of the low and high charge components using just the intensities of the charge states at $q = 17\,e$ and $q = 25\,e$ respectively. Each successive higher-charge component will have a greater width due to the statistical nature of Auger cascades. Therefore at higher charge states the spread of ions is greater and there will be significant overlap between the different charge components. In this case, the intensity of the different components in the CSD can be more accurately obtained by additionally measuring the intensity of the side-charge states ($q_{\mathrm{ref}} - 1$ and $q_{\mathrm{ref}} + 1$) at the focal plane of MARA, and then performing a convolved Gaussian fit using parameters for the centroid and width of each component gained during the initial CSD scan. Performing this type of analysis on the CSD would also increase the statistics by a factor ~ 3.

If this type of analysis were to be performed, care would have to be taken to measure a correction factor for the loss of transmission of $q_{\mathrm{ref}} - 1$ and $q_{\mathrm{ref}} + 1$ relative to q_{ref} (see section 4.4). It is also worth noting that for this analysis to be successful accurate values for the centroid and width of the different components in the CSD would be necessary. Table 5.3 in section 5.5 shows that even when the centroids and widths from the low and high charge component have been fixed using the scans at longer distances, the scan at $x = 43$ μm still gives large errors on the fit parameters for the second-high charge component. In future experiments, CSD scans should aim to collect sufficient statistics at high charge states in order to perform accurate fits to the higher charge components.

In future charge plunger experiments the following steps should be taken at the start of the experiment:

(a) Perform a scan of CSD to identify the charge components present, with a concentration on gaining sufficient statistics at higher charge states.

(b) Choose reference charge states, q_{ref}, at which data will be collected.

(c) For each q_{ref}, perform a scan of the side-charge states, $q_{\mathrm{ref}} - 1$ and $q_{\mathrm{ref}} + 1$, to obtain correction factors for the reduced transmission to the focal plane compared to q_{ref}.

6.3.3 Using JUROGAM 3

It is important to discuss the merits of aiding a charge plunger experiment with the use of a γ-ray spectrometer such as JUROGAM 3 . The use of JUROGAM 3 allows for a DDCM coin-

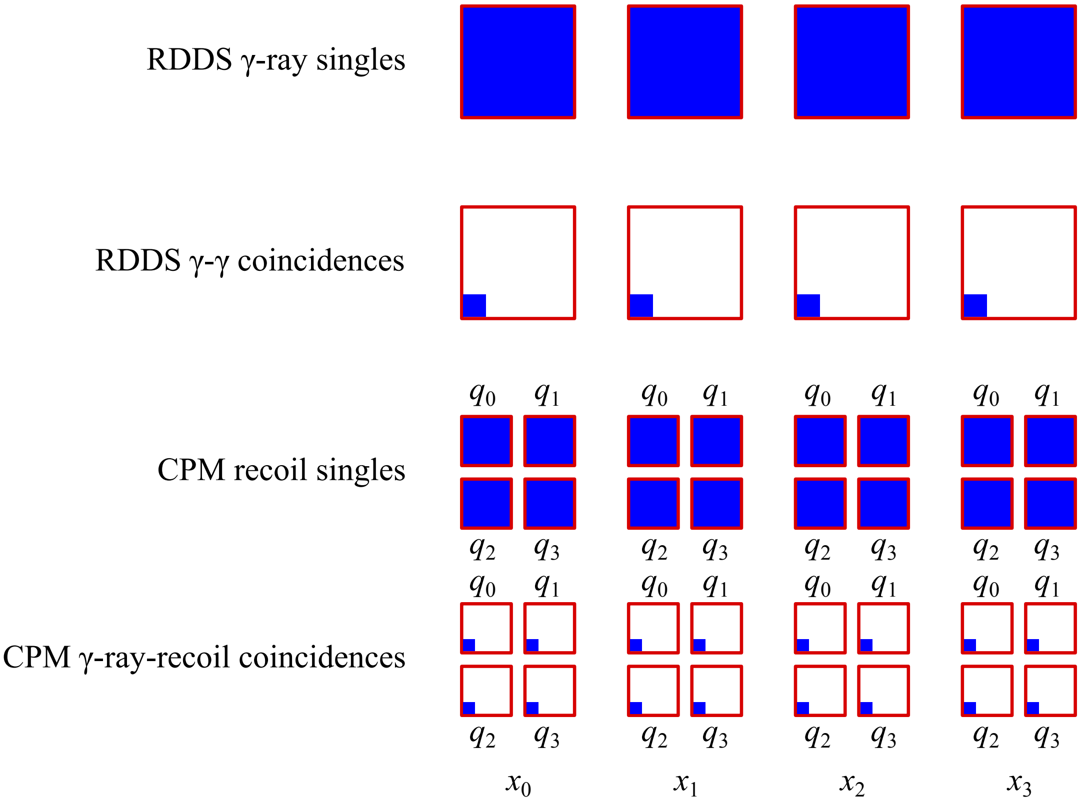

Figure 6.3: Schematic to show how collected data are split during an RDDS or charge plunger method (CPM) experiment. During a charge plunger experiment the data are not only split between different target-to-reset foil distances, but also between the different MARA settings. The available data are reduced by a factor of 20 when requiring the detection of an additional γ ray corresponding to a 5% detection efficiency. For illustration purposes four distances and four different charge states are shown.

cidence analysis to be performed with the charge plunger method. As discussed in section 6.2, a DDCM analysis has significant advantages over a Bateman analysis for performing lifetime measurements. However, for experiments aiming to measure the lifetime of weakly populated states, there is a trade off between the benefits of performing a DDCM analysis and the reduction of data due to requiring γ-ray-recoil coincidences. The JUROGAM 3 spectrometer has an absolute efficiency of 5.2% at 1.3 MeV [Pak20]. Using this efficiency, the available statistics in an experiment are reduced by a factor of ~ 20 when one requires a γ-ray-recoil condition. The data are then further split between the number of measured charge states and target-to-reset foil distances. Fig. 6.3 visualises how the data from an RDDS and charge plunger experiment are split, first between different target-to-reset foil distances, and then between different reference charge states. The reduction in data due to requiring the detection of an additional γ-ray is also shown for both techniques.

Comparatively, the detection efficiency of recoiling ions in the DSSSD after separation in MARA is $\sim 100\%$. Subsequent alpha decays, which either travel out of or further into the DSSSD, then have a detection efficiency of $\sim 50\%$. This value can be increased by using box detectors or, in the case of an alpha-decay chain, searching for child alpha decays [Pag03].

Two options should be considered for future experiments aiming to use the charge plunger method to perform lifetime measurements of excited states in nuclei with low production cross-sections:

(a) Collect the necessary statistics to analyse γ-ray-recoil coincidences at fewer charge states along the CSD, allowing for a DDCM coincidence analysis to be used.

(b) Collect data at more charge states along the CSD and use a Bateman analysis to obtain lifetime information.

In the first option, measurements at fewer charge states along the CSD may be needed compared to the second option. This is because a coincidence gate selects a specific decay path, limiting the number of internal conversion decays that occur after the reset foil. For future experiments using the charge plunger, the use of JUROGAM 3 to obtain γ-ray-recoil coincidences will depend heavily on the specific case.

6.4 Planned experiments

Further experiments have been planned to perform lifetime measurements on heavy nuclei using the charge plunger method. This has resulted in the submission of two proposals to the Program Advisory Committee (PAC) of the University of Jyväskylä Accelerator Laboratory. The first experiment, which was approved by the PAC in March 2020, will concentrate on the nucleus ^{222}Th. The experiment will be used to further develop the charge plunger method for cases where several internal conversions are expected during the de-excitation of the ground-state band. The second experiment, which was submitted to the PAC in March 2021, will look at performing a measurement of the lifetime of the 2_1^+ state in ^{254}No. This would constitute the heaviest nucleus for which the lifetime of a non-isomeric state has been made using plunger techniques. Both experiments will be briefly explained here.

6.4.1 ^{222}Th

As discussed in section 2.4.2, using the Bohr-Mottelson rotational model the intrinsic quadrupole moment for even-even nuclei can be obtained through measurements of $E2$ transition strengths.

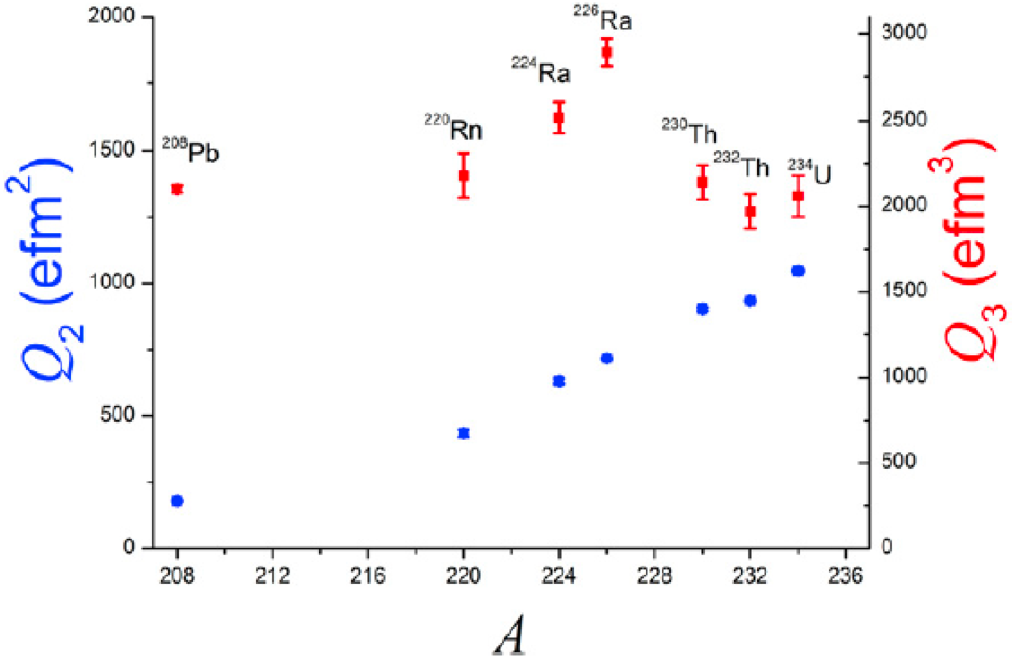

Figure 6.4: Summary of octupole (and quadrupole) moments available for nuclei in the actinide region of the chart. This figure is taken from ref. [But16].

In the model, higher order intrinsic moments, Q_L, are similarly related to EL transition strengths by,

$$B(EL; I_i \rightarrow I_f) = \frac{2L+1}{16\pi} Q_L^2 |\langle I_i K_i L0 | I_f K_f \rangle|^2 \tag{6.1}$$

where $\langle I_i K_i L0 | I_f K_f \rangle$ is the relevant Clebsch-Gordan coefficient for the transition [But16]. Interactions between negative and positive parity bands gives rise to $E1/E3$ transitions in nuclei with collective octupole deformation.

A definitive measure of the octupole collectivity comes from $E3$ transition rates. In the electromagnetic decay of states, lower order ($E1$ and $E2$) transitions dominate, and $E3$ transition strengths are difficult to obtain via lifetime measurements. In recent years, Coulomb excitation experiments using radioactive beams at facilities such as ISOLDE have been able to directly determine reduced transition probabilities and intrinsic electric octupole moments for isotopes of radon and radium [Gaf13]. This has spawned a new interest in the field and there have been several experimental and theoretical developments [Rob13, But19]. A recent review of the status of the field can be found here [But16]. Fig. 6.4 shows a summary of the octupole moment data obtained using Coulomb excitation techniques on nuclei above ^{208}Pb.

Thorium isotopes are predicted to show enhanced octupole collectivity around $A = 224 - 230$. There already exist plenty of experimental data [Sch86, Ack93, Web98, McG74] to suggest that these thorium isotopes exhibit rigid octupole shapes. However, the intrinsic octupole moment has so far been measured for only two of these nuclei ($A = 230, 232$) [But16]. This is in part due to the difficulty in producing these nuclei as radioactive beams for Coulomb excitation experiments. A programme of complementary experiments measuring the lifetimes and branching ratios of excited negative parity states in these thorium isotopes would make it possible to extend the knowledge of the strengths of octupole moments in this region of the chart.

The nucleus ^{222}Th provides a good case for developing the charge plunger method due to the relatively high internal conversion of the $2_1^+ \rightarrow 0_1^+$ ($\alpha = 0.93$), $4_1^+ \rightarrow 2_1^+$ ($\alpha = 0.28$) and $6_1^+ \rightarrow 4_1^+$ ($\alpha = 0.16$) transitions. The lifetimes of the 4_1^+ and 2_1^+ states have been previously measured to be $240(20)$ ps and $40(6)$ ps. The nucleus is also of interest due to the presence of a negative parity band interacting with the positive-parity ground state band through E1/E3 intraband transitions that compete with interband E2 transitions, a clear sign of octupole deformation [But96].

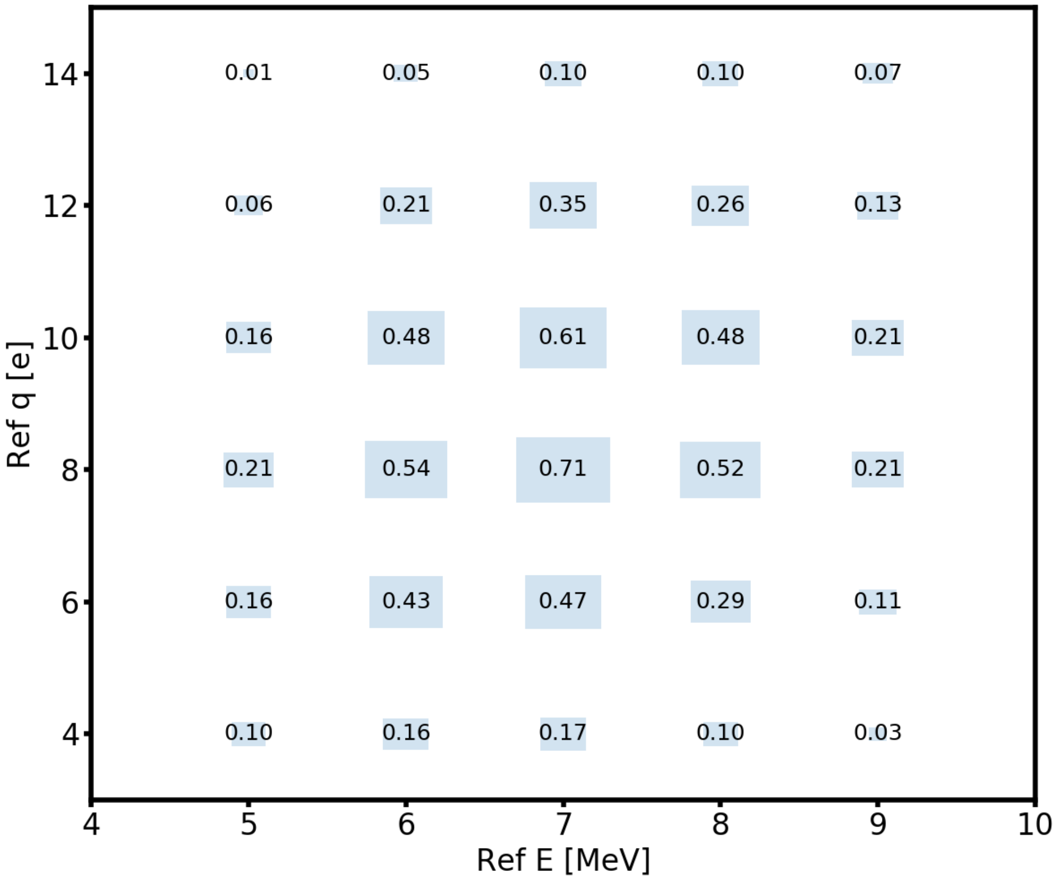

Figure 6.5: Simulated absolute transmission probability of ^{222}Th ions through MARA for different reference energies and charges. Each blue box represents a simulation of 2×10^4 recoils created before MARA and the number in each box represents the percentage of all recoils that are transmitted to the DSSSD for the given MARA settings. The simulation code was written by J. Sáren [Sar11]. In this scenario all excited states decay before the charge reset foil so only the low charge component remains.

An experiment has been planned to use the ^{208}Pb(^{18}O,4n)^{222}Th reaction at a beam energy of 95 MeV to populate low-lying states in ^{222}Th. The differential plunger DPUNS will be coupled to the MARA recoil separator and surrounded by the JUROGAM 3 spectrometer. MARA will be used to separate out the different ionic charge states, as has been done in the present work. A 0.5 mg/cm^2 ^{208}Pb foil will be used for the target, with a 50 µg/cm^2 carbon charge reset foil placed downstream. The low beam energy will result in ^{222}Th recoils with a low kinetic energy, $v/c \sim 1\%$. Therefore, to have sufficient transmission through MARA, such a thin reset foil is necessary. A simulation code written by J. Sáren [Sar11] has been used to estimate the transmission of ^{222}Th recoils through MARA. The results are shown in fig. 6.5. A maximum transmission probability of $\lesssim 1\%$ is expected when the MARA settings are set for a reference particle with $q_{\text{ref}} = 8\,e$, $E_{\text{ref}} = 7$ MeV and $m_{\text{ref}} = 222$ u. As the kinetic energy of recoils is so low, the MWPC will be removed from the setup so that the position of recoils in the DSSSD is instead used to calculate the m/q ratio of recoiling ions.

It is worth noting here that the charge plunger provides a more efficient method than the RDDS technique for measuring lifetime information in ^{222}Th. This is in part due to the relatively high internal conversion coefficients for the low-energy transitions. A perhaps more important factor is that the shift in ionic charge due to internal conversion is not affected by the recoil velocity, whereas the Doppler shift in γ ray energy is. A thin reset foil will be required to ensure a sufficient transmission through MARA, but this will also result in only a small change in velocity between recoils before and after the reset foil. This means it will be very hard to separate out the Doppler-shifted components for low energy transitions in the γ-ray spectrum. In this case, one is presented with an extremely difficult task to measure the lifetime of low-lying states using the RDDS technique.

In ref. [Smi95], the authors reported that, during a 48 h period using the same reaction with a similar beam energy and target thickness, they were able to collect 3.74×10^7 triple γ-ray coincidences that were attributed to ^{222}Th using the Eurogam spectrometer (a predecessor of JUROGAM 3) [Bea92, Nol92, Bec92]. Assuming similar statistics combined with a transmission efficiency through MARA of 0.7% a DDCM coincidence analysis would be possible and therefore this experiment will benefit from the use of JUROGAM 3 . However, as mentioned above, it will not be possible to separate Doppler-shifted components in the γ-ray spectrum and therefore target-to-reset foil distances should be chosen where the feeding transition always occurs before the reset foil.

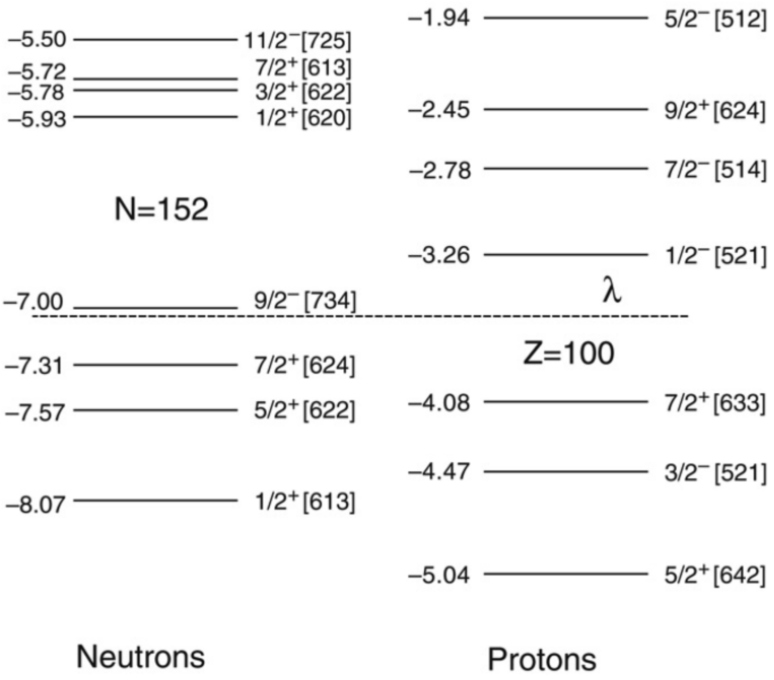

Figure 6.6: The single-particle levels in the region of the deformed shell gaps at Z=100 and N=152, calculated using a Woods-Saxon potential. This figure is taken from ref [Her08].

6.4.2 ^{254}No

A lot of progress has been made in the study of the transfermium nuclei in the N=150, Z=100 region (see review articles [The15, Dob15, Asa15, Hee15, Ack15]). Their enhanced stability is suggested to be due to shell corrections that allow extra stability against fission when these nuclei become deformed. This theory is supported by a wealth of experimental data on alpha decay and in-beam spectroscopy studies, which all point towards prolate-deformed nuclei with ground-state rotational bands observed up to high spin ($\sim 20\hbar$) that are well replicated using a rigid rotor model. The presence of K-isomerism has also been observed in many of these nuclei and has allowed for the assignment of single-particle configurations to a number of levels. Fig. 6.6 shows the single-particle structure at the Fermi surface for protons and neutrons in this region, determined using a Wood-Saxon potential for ^{250}Fm. Many of the Nilsson orbitals seen here are intruders that originate from higher proton and neutron numbers at sphericity but are brought down in energy by deformation.

A recent laser spectroscopy experiment was able to extract the change in mean square charge radius, $\delta < r^2 >$, for ^{252,253,254}No and, using the hyperfine splitting, was able to calculate the nuclear magnetic moment and spectroscopic quadrupole moment for ^{253}No [Rae18]. These results agreed well with theoretical predictions. However, at present, deformation parameters and intrinsic quadrupole moments in even-even nuclei in the region are determined using

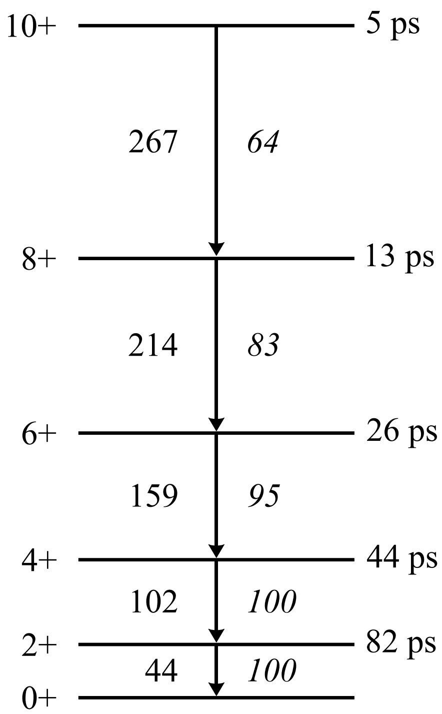

Figure 6.7: ^{254}No ground-state band level scheme. The lifetime of the 2^+ state is calculated using Grodzin's rule, adapted especially for actinide nuclei, shown in fig. 2.6. The lifetime of higher states in the band are then estimated assuming a rigid rotor model. Transition energies are given and in italics are the intensities normalised to the $2^+ \rightarrow 0^+$ 44 keV transition. The intensities of transitions in the ground state band are estimated from the entry distribution given in ref. [Hen14] for a beam energy of 219 MeV.

Grodzin's empirical formula which relates the energy of the 2^+ level to the lifetime of the state [Her01, Gro62] (see fig. 2.6 in section 2.4.3). The energies of these 2^+ states are also only predictions based on the Harris parametrisation [Rei99]. Thus far, lifetime studies have not been possible due to low production cross sections ($\leq 3\,\mu$b) and high internal conversion coefficients for low energy transitions, and consequently no direct measurements of quadrupole deformations exist for these nuclei.

This experiment aims to make the first lifetime measurements of an excited, non-isomeric state in a nucleus with $Z > 98$, by measuring the lifetime of the yrast 2^+ state in ^{254}No ($Z = 102$, $N = 152$). This nucleus provides a good case as it has been observed to have the highest production cross section in the region due to the well-matched beam and target combination of ^{48}Ca and ^{208}Pb which are both doubly-magic nuclei. A lifetime study on ^{254}No would give a direct experimental measurement of quadrupole deformation in an even-even transfermium nucleus, and provide a good test of the theoretical models predicting the nuclear structure in the region. The measurement, when combined with the data in fig. 2.6, will also allow us to make a more accurate extrapolation for determining lifetimes of excited 2_1^+ states in the superheavy region of the chart.

The level scheme of ^{254}No ground-state band is shown in fig. 6.7, including the ground-state

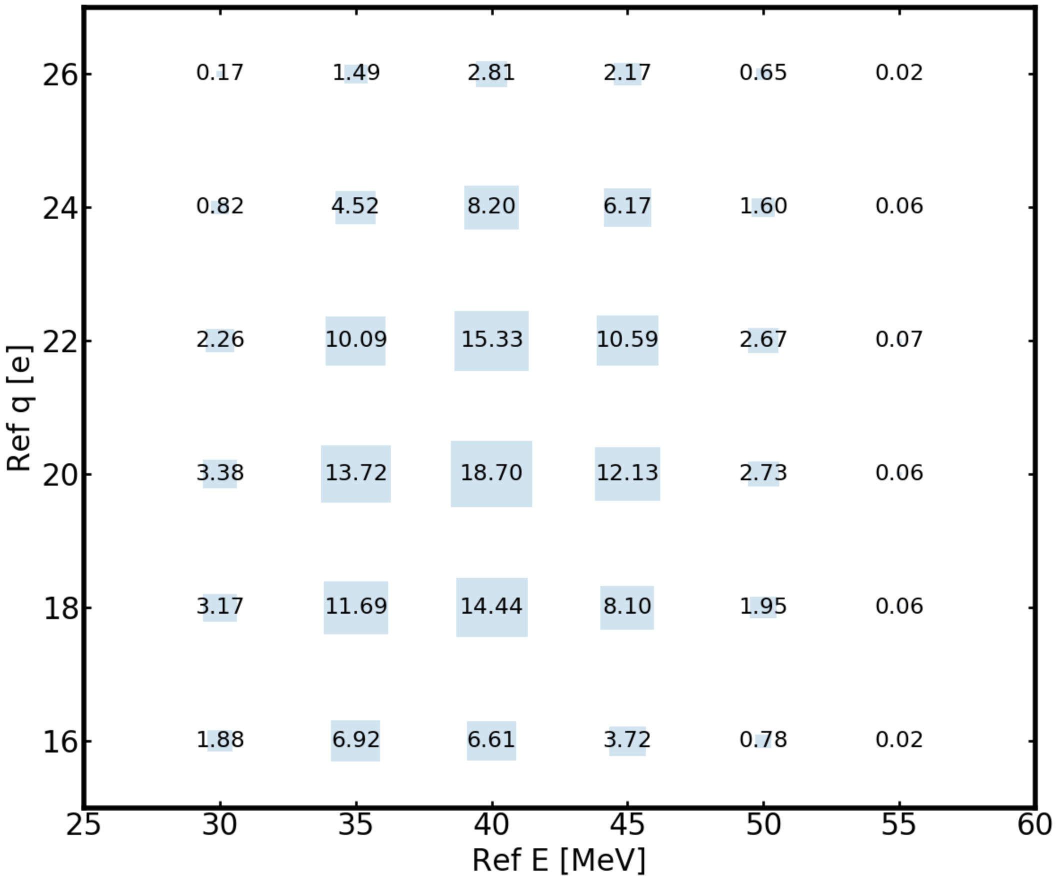

Figure 6.8: Simulated absolute transmission probability of ^{254}No ions through MARA for different reference energies and charges. In this scenario all excited states decay before the charge reset foil so only the low charge component remains.

band up to a spin of $10\hbar$. The lifetime of the yrast 2^+ state is estimated using Grodzin's rule, adapted especially for actinide nuclei, to be ~ 82 ps, and the lifetime of higher states in the band are then calculated using a single quadrupole moment, Q_0, according to equation 3.57. Internal conversion coefficients for each transition, taken from BrIcc [Kib08], are $1510(2^+ \rightarrow 0^+)$, $30(4^+ \rightarrow 2^+)$, $3.94(6^+ \rightarrow 4^+)$, $1.204(8^+ \rightarrow 6^+)$ and $0.535(10^+ \rightarrow 8^+)$.

The ^{208}Pb(^{48}Ca, 2n)^{254}No reaction will be used at a beam energy of 225 MeV. The target will consist of a 0.5 mg/cm^2 ^{208}Pb foil with a 1 mg/cm^2 Au backing to allow stretching of the target. This will result in a beam energy of 215 MeV at the centre of the target, which will give a cross section for production of ^{254}No of $\sigma = 2\,\mu$b [Rei99, Her06]. The doubly magic nature of the beam and the target gives a very clean reaction channel and there will be almost no other fusion-evaporation products. A 50 µg/cm^2 carbon foil will be used to provide a charge reset. The possibility of the use of a graphene foil instead will also be considered.

Unfortunately the ion transport code SRIM is unable to simulate the energy loss of elements beyond uranium. However, using a nucleus with $A = 254$, $Z = 92$ the energy of ions leaving the target is expected to be ~ 40 MeV ($v/c \sim 1.8\%$) and the energy of ions leaving the carbon charge reset foil are expected to be $\sim$ 39 MeV. The ions will then be separated by charge using the MARA recoil separator and detected at the focal plane using a double-sided silicon strip detector (DSSSD) where they will decay. A multi-wire proportional counter (MWPC) employed in front of the DSSSD will be used to differentiate between recoil and decay events. The simulated transmission probability of ^{254}No recoils for different MARA settings are shown in fig. 6.8. A maximum transmission probability of $\sim$ 20% is expected when the MARA settings are set for a reference particle with $q_{\text{ref}} = 20\,e$, $E_{\text{ref}} = 40$ MeV and $m_{\text{ref}} = 254$ u.

Due to a combination of the low cross section expected, the high internal conversion coefficients for transitions in the ground-state band and the need to split the data between different target-to-reset foil distances and MARA field settings, there will not be sufficient statistics to perform a DDCM γ-ray-recoil coincidence analysis. However, germanium detectors surrounding the target will be necessary to normalise the CSD spectra for data collected at different target-to-reset foil distances and MARA settings. The use of a large array of germanium detectors, such as JUROGAM 3 , will also provide a high γ-ray statistics experiment on ^{254}No that could contribute to other data sets.

6.5 Simulating charge-state distribution spectra

The development of a simulation to estimate charge-state distribution spectra at the focal plane of MARA is currently ongoing and will be the focus of future work. The simulation, written in the software package MATLAB [MAT18], uses Monte Carlo techniques to estimate the length of time for a nucleus to fully de-excite down to the ground state after being created at the target. Each transition in the de-excitation can proceed via either γ-ray emission or internal conversion. The changes in ionic charge state due to passing through the reset foil are estimated using the Schiwietz and Grande formula (see section 2.6.2). The increase in ionic charge state due to an Auger cascade is estimated using fig. 2.9 (see section 2.6.1).

The benefit of being able to simulate CSD spectra is that it can aid a CSD scan and help to identify the location of different charge components. The use of a simulation in data analysis may also provide an alternative way to obtain lifetime information. For example, one can vary the input lifetime for a state and compare the resulting simulated decay curves to an experimental decay curve, and obtain the best-solution via a χ^2 minimisation analysis. This type of analysis could reduce the number of distances at which data need to be collected,

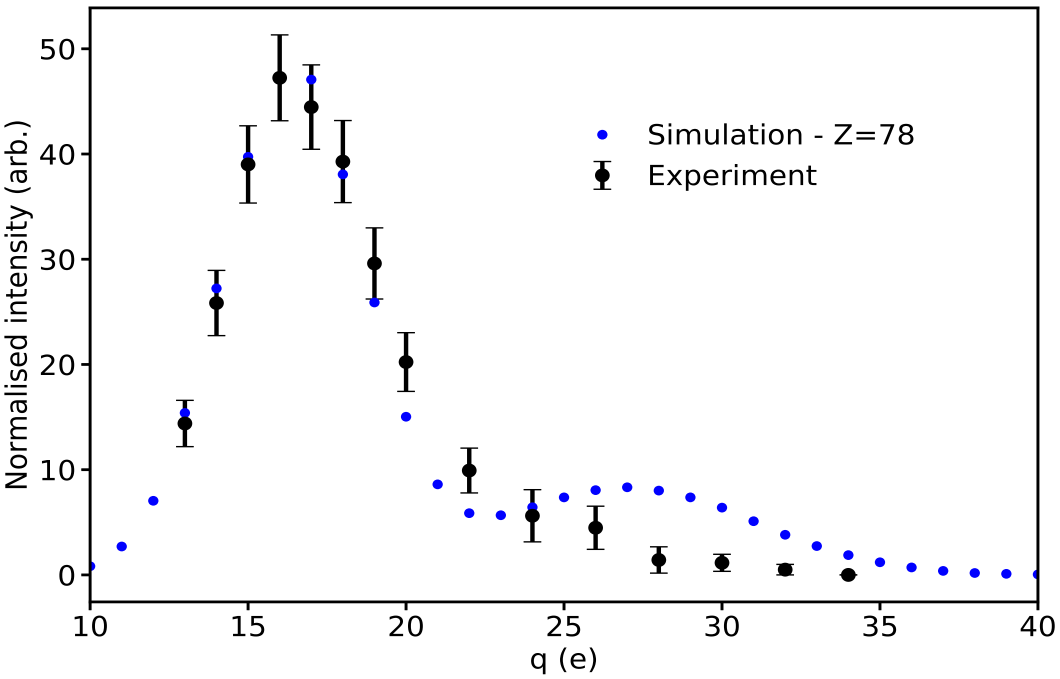

Figure 6.9: Comparison of simulated and experimental CSD spectrum for ^{178}Pt ions at $x = 1542\,\mu\text{m}$.

making it a more viable option for nuclei created with low cross sections. However, the simulation must first be shown to accurately reproduce CSD spectra.

A simulation of ^{178}Pt ions was performed using target-to-reset distance $x = 1542\,\mu\text{m}$. The input level scheme is considered up to the 10^+_1 state with lifetime data taken from experimental measurements and internal conversion coefficients taken from the BrIcc database. The simulated CSD spectra of ^{178}Pt ions is shown in fig. 6.9 (blue points) with the experimental data points (black points) from this work also shown for comparison. The intensities have been normalised to the $q = 16\,e$ value for the experimental data.

The increase in charge due to an Auger cascade is clearly overestimated by simulation. The average increase in charge is taken from the empirical curves shown fig. 2.9 for a nucleus with $Z = 78$. However, those data were collected by ionising neutral atoms using a laser and the data set only consists of two elements above $Z = 40$. In this experiment the average charge state of ions after the reset foil is $16.4\,e$, meaning the ions are already charged when an Auger cascade occurs.

Currently, we are exploring the possibility of improving the estimation of the increase in charge due to an Auger cascade using theoretical models. To do this we have contacted colleagues at the Australian National Laboratory (ANL) who have recently produced the BrIcc-Emis code which models the atomic relaxation process to estimate Auger electron yields for medical applications [Tee20, Kib21].

Chapter 7

Conclusion

This thesis has presented the methodology and analysis techniques for the use of a charge plunger method with a recoil separator to perform lifetime measurements on states which de-excite with large probabilities of internal conversion. Lifetime measurements are an important experimental probe of theoretical models predicting the structure of nuclei. The charge plunger method has considerable applications in heavy deformed nuclei where the combination of large proton numbers and collective excitations gives rise to low-energy transitions which have large internal conversion coefficients. As an example the $2_1^+ \rightarrow 0_1^+$ 44 keV transition in ^{254}No has a calculated internal conversion coefficient of 1510, according to the BrIcc database [Kib08].

A commissioning experiment was performed at the Accelerator Laboratory of the University of Jyväskylä to test the ability of the charge plunger method with a mass separator to measure the lifetime of states in ^{178}Pt which de-excite with relatively large internal conversion probabilities. The differential plunger device DPUNS was coupled to the vacuum-mode recoil separator MARA which was used to select ^{178}Pt ions by their charge state. DPUNS was surrounded by the JUROGAM 3 spectrometer which was used to detect prompt γ rays. After MARA, the ions travelled through a position-sensitive MWPC and were implanted into a DSSSD at the focal plane. The position of ions in the MWPC allowed for the determination of their m/q ratio. Identification of ^{178}Pt recoils was done using either prompt γ-ray-recoil coincidences or recoil-alpha decay coincidences in the DSSSD.

Two methods, namely, a DDCM coincidence analysis and Bateman analysis, were used to retrieve lifetime information. For the the DDCM coincidence analysis, a γ-ray-recoil coincidence gate set on the $4_1^+ \rightarrow 2_1^+$ 257 keV feeding transition and the resulting CSD spectra were analysed in the DDCM framework. This yielded the lifetime for the 2_1^+ state in ^{178}Pt of $\tau = 430(20)\,\mathrm{ps}$. For the Bateman analysis, CSD spectra were obtained using recoil-alpha coincidences. The de-excitation of states were modelled by fitting a two-state Bateman equation to the relative intensity of high charge ions against distance. The lifetime of states in this fit were determined using a single quadrupole moment for the rotational band. This gave the lifetime of the 2_1^+ state as $\tau = 430(50)\,\mathrm{ps}$ and $\tau = 54(6)\,\mathrm{ps}$ for the 4_1^+ state. These values agree with both previous results and the measurement made using a DDCM coincidence analysis.

The success of the commissioning experiment and the development of the analysis techniques used here are crucial for a thorough understanding of how the charge plunger method can be used with a recoil separator. They establish a procedure for future experiments using the technique. Two points in particular should be considered. Firstly, an accurate CSD scan is required. Secondly, it should be taken into consideration the reduction in statistics that will arise when a DDCM coincidence analysis is used. This latter point is highlighted by the two future planned experiments on ^{222}Th and ^{254}No. In the ^{222}Th experiment, it is predicted that there will be sufficient γ-ray-recoil statistics and a DDCM coincidence analysis will be suitable. However, in the ^{254}No case it is expected that the requirement of γ ray detection will reduce the available data set considerably and therefore a Bateman analysis will be necessary.

The success of these future experiments will showcase the ability of the charge plunger method to perform lifetime measurements of excited states in nuclei at the spectroscopic boundary of the nuclear chart.

Bibliography

[Ach09] E. Achterberg, O.A. Capurro, G.V. Marti. Nuclear Data Sheets for A = 178, *Nuclear Data Sheets*, 110(7):1473 – 1688, 2009. DOI https://doi.org/10.1016/j.nds.2009.05.002. URL `http://www.sciencedirect.com/science/article/pii/S0090375209000490`.

[Ack93] B. Ackermann, H. Baltzer, C. Ensel, et al. Collective E1 transitions in even-A Ra, Th, and U nuclei, *Nuclear Physics A*, 559(1):61–82, 1993. DOI https://doi.org/10.1016/0375-9474(93)90180-6. URL `https://www.sciencedirect.com/science/article/pii/0375947493901806`.

[Ack15] D. Ackermann. Nuclear spectroscopy in nuclei with $Z \geq 110$, *Nuclear Physics A*, 944:376 – 387, 2015. DOI https://doi.org/10.1016/j.nuclphysa.2015.09.002. URL `http://www.sciencedirect.com/science/article/pii/S0375947415002018`. Special Issue on Superheavy Elements.

[Ale70] T.K. Alexander, A. Bell. A target chamber for recoil-distance lifetime measurements, *Nuclear Instruments and Methods*, 81(1):22 – 26, 1970. DOI https://doi.org/10.1016/0029-554X(70)90604-X. URL `http://www.sciencedirect.com/science/article/pii/0029554X7090604X`.

[And76] G. Andersson, S.E. Larsson, G. Leander, et al. Nuclear shell structure at very high angular momentum, *Nuclear Physics A*, 268(2):205–256, 1976. DOI https://doi.org/10.1016/0375-9474(76)90461-9. URL `https://www.sciencedirect.com/science/article/pii/0375947476904619`.

[Asa15] M. Asai, F.P. Heßberger, A. Lopez-Martens. Nuclear structure of elements with $100 \leq Z \leq 109$ from alpha spectroscopy, *Nuclear Physics A*, 944:308 – 332, 2015. DOI https://doi.org/10.1016/j.nuclphysa.2015.06.011. URL `http://www.sciencedirect.com/science/article/pii/S0375947415001402`. Special Issue on Superheavy Elements.

[Aug25] Pierre Auger. Sur l'effet photoélectrique composé, *Journal de Physique et le Radium*, 6(6):205–208, 1925. DOI https://doi.org/10.1051/jphysrad:0192500606020500. URL https://jphysrad.journaldephysique.org/articles/jphysrad/abs/1925/06/jphysrad_1925__6_6_205_0/jphysrad_1925__6_6_205_0.html.

[Bac78] H. Backe, L. Richter, R. Willwater, et al. In-beam spectroscopy of low energy conversion electrons with a recoil shadow method — A new possibility for sub-nanosecond lifetime measurements, *Z Physik A*, 285, 1978. DOI https://doi.org/10.1007/BF01408742. URL https://link.springer.com/article/10.1007%2FBF01408742.

[Ban02] I.M. Band, M.B. Trzhaskovskaya, C.W. Nestor, et al. Dirac-Fock Internal Conversion Coefficients, *Atomic Data and Nuclear Data Tables*, 81(1):1 – 334, 2002. DOI https://doi.org/10.1006/adnd.2002.0884. URL http://www.sciencedirect.com/science/article/pii/S0092640X02908843.

[Bar20a] L. Barber, D.M. Cullen, M.M. Giles, et al. Performing the differential decay curve method on γ-ray transitions with unresolved Doppler-shifted components, *Nuclear Instruments and Methods in Physics Research Section A: Accelerators, Spectrometers, Detectors and Associated Equipment*, 950:162965, 2020. DOI https://doi.org/10.1016/j.nima.2019.162965. URL http://www.sciencedirect.com/science/article/pii/S0168900219313567.

[Bar20b] L. Barber, J. Heery, D.M. Cullen, et al. A charge plunger device to measure the lifetimes of excited nuclear states where transitions are dominated by internal conversion, *Nuclear Instruments and Methods in Physics Research Section A: Accelerators, Spectrometers, Detectors and Associated Equipment*, 979:164454, 2020. DOI https://doi.org/10.1016/j.nima.2020.164454. URL http://www.sciencedirect.com/science/article/pii/S0168900220308512.

[Bas74] R. Bass. Fusion of heavy nuclei in a classical model, *Nuclear Physics A*, 231(1):45 – 63, 1974. DOI https://doi.org/10.1016/0375-9474(74)90292-9. URL http://www.sciencedirect.com/science/article/pii/0375947474902929.

[Bat08] Harry Bateman. The solution of a system of differential equations occurring in the theory of radio-active transformations, *Proc. Cambridge Phil. Soc., 1908*, 15:423–427, 1908.

[Bea92] C.W. Beausang, S.A. Forbes, P. Fallon, et al. Measurements on prototype Ge and BGO detectors for the Eurogam array, *Nuclear Instruments and Methods in Physics Research Section A: Accelerators, Spectrometers, Detectors and Associated Equipment*, 313(1):37–49, 1992. DOI https://doi.org/10.1016/0168-9002(92)90084-H. URL https://www.sciencedirect.com/science/article/pii/016890029290084H.

[Bec92] F.A. Beck. EUROBALL: Large gamma ray spectrometers through european collaborations, *Progress in Particle and Nuclear Physics*, 28:443–461, 1992. DOI https://doi.org/10.1016/0146-6410(92)90047-6. URL https://www.sciencedirect.com/science/article/pii/0146641092900476.

[Bet72] Hans-Dieter Betz. Charge States and Charge-Changing Cross Sections of Fast Heavy Ions Penetrating Through Gaseous and Solid Media, *Rev. Mod. Phys.*, 44:465–539, Jul 1972. DOI 10.1103/RevModPhys.44.465. URL https://link.aps.org/doi/10.1103/RevModPhys.44.465.

[Bla52] J.M. Blatt, V.F. Weisskopf. *Theoretical Nuclear Physics*. Dover Publications Inc., 1952.

[Boh75a] Aage Bohr, Ben R. Mottelson. *Nuclear Structure - Volume I: Single-Particle Motion*. W. A. Benjamin Inc., 1975.

[Boh75b] Aage Bohr, Ben R. Mottelson. *Nuclear Structure - Volume II: Nuclear Deformations*. W. A. Benjamin In.c, 1975.

[Böh93] G. Böhm, A. Dewald, P. Petkov, P. von Brentano. The differential decay curve method for the analysis of Doppler shift timing experiments, *Nuclear Instruments and Methods in Physics Research Section A: Accelerators, Spectrometers, Detectors and Associated Equipment*, 329(1):248–261, 1993. DOI https://doi.org/10.1016/0168-9002(93)90944-D. URL https://www.sciencedirect.com/science/article/pii/016890029390944D.

[Bow82] J. D. Bowman, R. E. Eppley, E. K. Hyde. Alpha spectroscopy of nuclides produced in the interaction of 5 GeV protons with heavy element targets, *Phys. Rev. C*, 25:941–951, Feb 1982. DOI 10.1103/PhysRevC.25.941. URL https://link.aps.org/doi/10.1103/PhysRevC.25.941.

[But96] P. A. Butler, W. Nazarewicz. Intrinsic reflection asymmetry in atomic nuclei, *Rev.*

Mod. Phys., 68:349–421, Apr 1996. DOI 10.1103/RevModPhys.68.349. URL https://link.aps.org/doi/10.1103/RevModPhys.68.349.

[But16] P. A. Butler. Octupole collectivity in nuclei, *Journal of Physics G: Nuclear and Particle Physics*, 43(7):073002, jun 2016. DOI 10.1088/0954-3899/43/7/073002. URL https://doi.org/10.1088/0954-3899/43/7/073002.

[But19] P.A. Butler, L.P. Gaffney, P. Spagnoletti, et al. The observation of vibrating pear-shapes in radon nuclei, *Nature Communications*, 10, 2019. DOI https://doi.org/10.1038/s41467-019-10494-5. URL https://www.nature.com/articles/s41467-019-10494-5.

[Car66] T. A. Carlson, W. E. Hunt, M. O. Krause. Relative Abundances of Ions Formed as the Result of Inner-Shell Vacancies in Atoms, *Phys. Rev.*, 151:41–47, Nov 1966. DOI 10.1103/PhysRev.151.41. URL https://link.aps.org/doi/10.1103/PhysRev.151.41.

[Cie20] M. Ciemała, S. Ziliani, F. C. L. Crespi, et al. Testing ab initio nuclear structure in neutron-rich nuclei: Lifetime measurements of second 2^+ state in ^{16}C and ^{20}O, *Phys. Rev. C*, 101:021303, Feb 2020. DOI 10.1103/PhysRevC.101.021303. URL https://link.aps.org/doi/10.1103/PhysRevC.101.021303.

[Cle78] L. Cleemann, J. Eberth, W. Neumann, et al. A plunger device with a piezo-electric fine adjustment and a PLL distance regulation, *Nuclear Instruments and Methods*, 156(3):477 – 482, 1978. DOI https://doi.org/10.1016/0029-554X(78)90747-4. URL http://www.sciencedirect.com/science/article/pii/0029554X78907474.

[Del10] D. S. Delion, R. Wyss, R. J. Liotta, et al. Investigations of proton-neutron correlations close to the drip line, *Phys. Rev. C*, 82:024307, Aug 2010. DOI 10.1103/PhysRevC.82.024307. URL https://link.aps.org/doi/10.1103/PhysRevC.82.024307.

[Dem67] A.G. Demin, T. Fényes, I. Mahunka, et al. New mercury isotopes, *Nuclear Physics A*, 106(2):337–349, 1967. DOI https://doi.org/10.1016/0375-9474(67)90878-0. URL https://www.sciencedirect.com/science/article/pii/0375947467908780.

[Dew89] A. Dewald, S. Harissopulos, P. von Brentano. The differential plunger and the differential decay curve method for the analysis of recoil distance Doppler-shift data, *Z. Physik A - Atomic Nuclei*, 334:163 – 175, 1989. DOI https://doi.org/10.1007/BF01294217. URL https://link.springer.com/article/10.1007/BF01294217.

[Dew12] A. Dewald, O. Möller, P. Petkov. Developing the Recoil Distance Doppler-Shift technique towards a versatile tool for lifetime measurements of excited nuclear states, *Progress in Particle and Nuclear Physics*, 67(3):786–839, 2012. DOI https://doi.org/10.1016/j.ppnp.2012.03.003. URL http://www.sciencedirect.com/science/article/pii/S0146641012000713.

[Dob15] J. Dobaczewski, A.V. Afanasjev, M. Bender, et al. Properties of nuclei in the nobelium region studied within the covariant, Skyrme, and Gogny energy density functionals, *Nuclear Physics A*, 944:388 – 414, 2015. DOI https://doi.org/10.1016/j.nuclphysa.2015.07.015. URL http://www.sciencedirect.com/science/article/pii/S0375947415001633. Special Issue on Superheavy Elements.

[Don15] M. Doncel, T. Bäck, D. M. Cullen, et al. Lifetime measurement of the first excited 2^+ state in ^{112}Te, *Phys. Rev. C*, 91:061304, Jun 2015. DOI 10.1103/PhysRevC.91.061304. URL https://link.aps.org/doi/10.1103/PhysRevC.91.061304.

[Don17a] M. Doncel, T. Bäck, C. Qi, et al. Spin-dependent evolution of collectivity in ^{112}Te, *Phys. Rev. C*, 96:051304, Nov 2017. DOI 10.1103/PhysRevC.96.051304. URL https://link.aps.org/doi/10.1103/PhysRevC.96.051304.

[Don17b] M. Doncel, B. Cederwall, C. Qi, et al. Lifetime measurements of excited states in ^{162}W and ^{164}W and the evolution of collectivity in rare-earth nuclei, *Phys. Rev. C*, 95:044321, Apr 2017. DOI 10.1103/PhysRevC.95.044321. URL https://link.aps.org/doi/10.1103/PhysRevC.95.044321.

[Dra86] G. D. Dracoulis, A. E. Stuchbery, A. P. Byrne, et al. Shape coexistence in very neutron-deficient Pt isotopes, *Journal of Physics G: Nuclear Physics*, 12(3):L97–L103, mar 1986. DOI 10.1088/0305-4616/12/3/005. URL https://doi.org/10.1088%2F0305-4616%2F12%2F3%2F005.

[Duc99] G. Duchêne, F.A. Beck, P.J. Twin, et al. The Clover: a new generation of composite Ge detectors, *Nuclear Instruments and Methods in Physics Research Section A: Accelerators, Spectrometers, Detectors and Associated Equipment*, 432(1):90

– 110, 1999. DOI https://doi.org/10.1016/S0168-9002(99)00277-6. URL http://www.sciencedirect.com/science/article/pii/S0168900299002776.

[Ebe08] J. Eberth, J. Simpson. From Ge (Li) detectors to gamma-ray tracking arrays–50 years of gamma spectroscopy with germanium detectors, *Progress in Particle and Nuclear Physics*, 60(2):283–337, 2008.

[Ell57] J.P. Elliot, A.M. Lane. The Nuclear Shell Model. In S. Flügge, editor, *Structure of Atomic Nuclei*. Springer-Verlag Berlin Heidelberg GMBH, 1957.

[Eml84] H. Emling, E. Grosse, R. Kulessa, et al. Rotation-induced shape transitions in Dy nuclei, *Nuclear Physics A*, 419(1):187–220, 1984. DOI https://doi.org/10.1016/0375-9474(84)90292-6. URL https://www.sciencedirect.com/science/article/pii/0375947484902926.

[ENS] ENSDF. From ENSDF database as of Feb. 23rd, 2021. Version available at http://www.nndc.bnl.gov/ensarchivals/.

[For13] C. Forssén, R. Roth, P. Navrátil. Systematics of 2^+states in C isotopes from the no-core shell model, *Journal of Physics G: Nuclear and Particle Physics*, 40(5):055105, mar 2013. DOI 10.1088/0954-3899/40/5/055105. URL https://doi.org/10.1088%2F0954-3899%2F40%2F5%2F055105.

[Fra19] C. Fransen, F. Mammes, R. Bark, et al. Structural investigation of neutron-deficient Pt isotopes: the case of 178Pt, *EPJ Web Conf.*, 223:01016, 2019. DOI 10.1051/epjconf/201922301016. URL https://doi.org/10.1051/epjconf/201922301016.

[Fra21] Christoph Fransen. private communication, March 2021.

[Gaf13] L. Gaffney, P. Butler, M. Scheck, et al. Studies of pear-shaped nuclei using accelerated radioactive beams, *Nature*, 497:199–204, May 2013. DOI https://doi.org/10.1038/nature12073. URL https://www.nature.com/articles/nature12073.

[Gal70] J.L. Gallant. The preparation of flat target foils for recoil-distance lifetime measurements, *Nuclear Instruments and Methods*, 81(1):27–28, 1970. DOI https://doi.org/10.1016/0029-554X(70)90605-1. URL https://www.sciencedirect.com/science/article/pii/0029554X70906051.

[Gil19a] Michael Giles. Commissioning of a triple-foil plunger for exotic nuclei (TPEN). Ph.D. thesis, The University of Manchester, 2019.

[Gil19b] M.M. Giles, D.M. Cullen, L. Barber, et al. TPEN: A Triple-foil differential Plunger for lifetime measurements of excited states in Exotic Nuclei, *Nuclear Instruments and Methods in Physics Research Section A: Accelerators, Spectrometers, Detectors and Associated Equipment*, 923:139–146, 2019. DOI https://doi.org/10.1016/j.nima.2019.01.089. URL https://www.sciencedirect.com/science/article/pii/S0168900219301597.

[Gra05] T. Grahn, A. Dewald, O. Möller, et. al. RDDS lifetime measurement with JUROGAM + RITU. In *European Physical Journal A*, 2005.

[Gra06] T. Grahn, A. Dewald, O. Möller, et al. Collectivity and Configuration Mixing in ^{186,188}Pb and ^{194}Po, *Phys. Rev. Lett.*, 97:062501, Aug 2006. DOI 10.1103/PhysRevLett.97.062501. URL https://link.aps.org/doi/10.1103/PhysRevLett.97.062501.

[Gra09] T. Grahn, A. Dewald, P. T. Greenlees, et al. Collectivity of ^{196}Po at low spin, *Phys. Rev. C*, 80:014323, Jul 2009. DOI 10.1103/PhysRevC.80.014323. URL https://link.aps.org/doi/10.1103/PhysRevC.80.014323.

[Gra16] T. Grahn, S. Stolze, D. T. Joss, et al. Excited states and reduced transition probabilities in ^{168}**Os**, *Phys. Rev. C*, 94:044327, Oct 2016. DOI 10.1103/PhysRevC.94.044327. URL https://link.aps.org/doi/10.1103/PhysRevC.94.044327.

[Gro62] L. Grodzins. The uniform behaviour of electric quadrupole transition probabilities from first 2^+ states in even-even nuclei, *Phys. Letters*, 2, Aug 1962. DOI 10.1016/0031-9163(62)90162-2. URL https://www.osti.gov/biblio/4698672.

[Hab77] D. Habs, V. Metag, H. J. Specht, G. Ulfert. Quadrupole Moment of the 8-μs Fission Isomer in ^{239}Pu, *Phys. Rev. Lett.*, 38:387–389, Feb 1977. DOI 10.1103/PhysRevLett.38.387. URL https://link.aps.org/doi/10.1103/PhysRevLett.38.387.

[Hag68] R.S. Hager, E.C. Seltzer. Internal conversion tables part I: K-, L-, M-shell conversion coefficients for Z=30 to Z=103, *Nuclear Data Sheets. Section A*, 4(1):1 – 11, 1968. DOI https://doi.org/10.1016/S0550-306X(68)80002-3. URL http://www.sciencedirect.com/science/article/pii/S0550306X68800023.

[Hag79] E. Hagberg, P.G. Hansen, P. Hornshøj, et al. Alpha decay of neutron-deficient mercury isotopes and their daughters, *Nuclear Physics A*, 318(1):29–44,

1979. DOI https://doi.org/10.1016/0375-9474(79)90467-6. URL https://www.sciencedirect.com/science/article/pii/0375947479904676.

[Han70] P.G. Hansen, H.L. Nielsen, K. Wilsky, et al. Studies of the α-active isotopes of mercury, gold and platinum, *Nuclear Physics A*, 148(1):249–272, 1970. DOI https://doi.org/10.1016/0375-9474(70)90622-6. URL https://www.sciencedirect.com/science/article/pii/0375947470906226.

[Har87] S. Harissopulos, A. Dewald, A. Gelberg, et al. Lifetime measurements in 120Xe, using a coincidence plunger technique, *Nuclear Physics A*, 467(3):528–538, 1987. DOI https://doi.org/10.1016/0375-9474(87)90543-4. URL https://www.sciencedirect.com/science/article/pii/0375947487905434.

[Hee15] P.-H. Heenen, J. Skalski, A. Staszczak, D. Vretenar. Shapes and α- and β-decays of superheavy nuclei, *Nuclear Physics A*, 944:415 – 441, 2015. DOI https://doi.org/10.1016/j.nuclphysa.2015.07.016. URL http://www.sciencedirect.com/science/article/pii/S0375947415001748. Special Issue on Superheavy Elements.

[Hee21] J. Heery, L. Barber, J. Vilhena, et al. Lifetime measurements of yrast states in ^{178}Pt using the charge plunger method with a recoil separator, *European Physics Journal A*, 57, 2021. DOI 10.1140/epja/s10050-021-00425-8. URL https://link.springer.com/article/10.1140/epja/s10050-021-00425-8.

[Hei27] W. Heisenberg. Über den anschaulichen Inhalt der quantentheoretischen Kinematik und Mechanik, *Zeitschrift für Physik*, 43:172 – 198, 1927. DOI https://doi.org/10.1007/BF01397280. URL https://link.springer.com/article/10.1007%2FBF01397280.

[Hen14] G. Henning, T. L. Khoo, A. Lopez-Martens, et al. Fission Barrier of Superheavy Nuclei and Persistence of Shell Effects at High Spin: Cases of ^{254}No and ^{220}Th, *Phys. Rev. Lett.*, 113:262505, Dec 2014. DOI 10.1103/PhysRevLett.113.262505. URL https://link.aps.org/doi/10.1103/PhysRevLett.113.262505.

[Her01] R.-D. Herzberg, N. Amzal, F. Becker, et al. Spectroscopy of transfermium nuclei: $^{252}_{102}$No, *Phys. Rev. C*, 65:014303, Dec 2001. DOI 10.1103/PhysRevC.65.014303. URL https://link.aps.org/doi/10.1103/PhysRevC.65.014303.

[Her06] R.-D. Herzberg, P. T. Greenlees, P. A. Butler, et al. Nuclear isomers in superheavy elements as stepping stones towards the island of stability, *Nature*, 442(7105):896–

899, Aug 2006. DOI 10.1038/nature05069. URL https://doi.org/10.1038/nature05069.

[Her08] R.-D. Herzberg, P.T. Greenlees. In-beam and decay spectroscopy of transfermium nuclei, *Progress in Particle and Nuclear Physics*, 61(2):674 – 720, 2008. DOI https://doi.org/10.1016/j.ppnp.2008.05.003. URL http://www.sciencedirect.com/science/article/pii/S0146641008000409.

[Hey94] K. Heyde. *Basic Ideas and Concepts in Nuclear Physics - An Introductory Approach*. IOP Publishing Ltd., 1994.

[Hey11] K. Heyde, J. L. Wood. Shape coexistence in atomic nuclei, *Rev. Mod. Phys.*, 83:1467–1521, Nov 2011. DOI 10.1103/RevModPhys.83.1467. URL https://link.aps.org/doi/10.1103/RevModPhys.83.1467.

[Hod16] D. Hodge, D. M. Cullen, M. J. Taylor, et al. Deformation of the proton emitter ^{113}**Cs** from electromagnetic transition and proton-emission rates, *Phys. Rev. C*, 94:034321, Sep 2016. DOI 10.1103/PhysRevC.94.034321. URL https://link.aps.org/doi/10.1103/PhysRevC.94.034321.

[Jön13] P. Jönsson, G. Gaigalas, J. Bieroń, et al. New version: Grasp2K relativistic atomic structure package, *Computer Physics Communications*, 184(9):2197–2203, 2013. DOI https://doi.org/10.1016/j.cpc.2013.02.016. URL https://www.sciencedirect.com/science/article/pii/S0010465513000738.

[Kib08] T. Kibédi, T.W. Burrows, M.B. Trzhaskovskaya, et al. Evaluation of theoretical conversion coefficients using BrIcc, *Nuclear Instruments and Methods in Physics Research Section A: Accelerators, Spectrometers, Detectors and Associated Equipment*, 589(2):202 – 229, 2008. DOI https://doi.org/10.1016/j.nima.2008.02.051. URL http://www.sciencedirect.com/science/article/pii/S0168900208002520.

[Kib21] Tibor Kibédi. private communication, Jan 2021.

[Kor17] S. Korenev, R. Dishman, A. Yebra, et al. Characterization of Graphene Stripper Foils in 11-MeV Cyclotrons, *Physics Procedia*, 90:369–373, 2017. DOI https://doi.org/10.1016/j.phpro.2017.09.034. URL https://www.sciencedirect.com/science/article/pii/S1875389217301931.

[Kra88] Kenneth S. Krane. *Introductory Nuclear Physics*. John Wiley & Sons Inc., 1988.

[Kuh93] A. Kuhnert, E. A. Henry, T. F. Wang, et al. Search for an M0 transition in ^{170}Yb, *Phys. Rev. C*, 47:2386–2388, May 1993. DOI 10.1103/PhysRevC.47.2386. URL `https://link.aps.org/doi/10.1103/PhysRevC.47.2386`.

[Laz01] I. Lazarus, D.E. Appelbe, P.A. Butler, et al. The GREAT triggerless total data readout method, *IEEE Transactions on Nuclear Science*, 48(3):567–569, June 2001. DOI 10.1109/23.940120. URL `https://ieeexplore.ieee.org/abstract/document/940120`.

[Lee12] B. Q. Lee, T. Kibédi, A. E. Stuchbery, K. A. Robertson. Atomic Radiation in Nuclear Decay, *EPJ Web of Conferences*, 35:04003, 2012. DOI 10.1051/epjconf/20123504003. URL `https://doi.org/10.1051/epjconf/20123504003`.

[Lee13] B. Q. Lee, T Kibédi, A. E. Stuchbery, et al. A Model to Realize the Potential of Auger Electrons for Radiotherapy, *EPJ Web of Conferences*, 63:01002, 2013. DOI 10.1051/epjconf/20136301002. URL `https://doi.org/10.1051/epjconf/20136301002`.

[Li14] C. B. Li, F. Q. Chen, X. G. Wu, et al. Lifetime measurement of the first 2^+ state in ^{178}Pt, *Phys. Rev. C*, 90:047302, Oct 2014. DOI 10.1103/PhysRevC.90.047302. URL `https://link.aps.org/doi/10.1103/PhysRevC.90.047302`.

[Li16] H. J. Li, B. Cederwall, M. Doncel, et al. Lifetime measurements in ^{166}Re: Collective versus magnetic rotation, *Phys. Rev. C*, 93:034309, Mar 2016. DOI 10.1103/PhysRevC.93.034309. URL `https://link.aps.org/doi/10.1103/PhysRevC.93.034309`.

[Lin62] N Lingappa, E Kondaiah, C Badrinathan, et al. Width of the first excited state of Sn116, *Nuclear Physics*, 38:146 – 153, 1962. DOI https://doi.org/10.1016/0029-5582(62)91024-6. URL `http://www.sciencedirect.com/science/article/pii/0029558262910246`.

[Mac89] H. Mach, R.L. Gill, M. Moszyński. A method for picosecond lifetime measurements for neutron-rich nuclei: (1) Outline of the method, *Nuclear Instruments and Methods in Physics Research Section A: Accelerators, Spectrometers, Detectors and Associated Equipment*, 280(1):49–72, 1989. DOI https://doi.org/10.1016/0168-9002(89)91272-2. URL `https://www.sciencedirect.com/science/article/pii/0168900289912722`.

[MAT18] MATLAB. *9.4.0.813654 (R2018a)*. The MathWorks Inc., Natick, Massachusetts, 2018.

[May50] M. G. Mayer. Nuclear Configurations in the Spin-Orbit Coupling Model. I. Empirical Evidence, *Phys. Rev.*, 78:16–21, Apr 1950. DOI 10.1103/PhysRev.78.16. URL `https://link.aps.org/doi/10.1103/PhysRev.78.16`.

[McG74] F. K. McGowan, C. E. Bemis, W. T. Milner, et al. Coulomb excitation of vibrational-like states in the even-A actinide nuclei, *Phys. Rev. C*, 10:1146–1155, Sep 1974. DOI 10.1103/PhysRevC.10.1146. URL `https://link.aps.org/doi/10.1103/PhysRevC.10.1146`.

[Mei22] L. Meitner. Über die Entstehung der β-Strahl-Spektren radioaktiver Substanzen, *Z Physik*, 9:131–144, 1922. DOI 10.1007/BF01326962. URL `https://link.springer.com/article/10.1007%2FBF01326962`.

[Met75] V. Metag, D. Habs, H. J. Specht, et al. Hyperfine interactions and charge distributions of actinide ions recoiling into vacuum, *Hyperfine Interactions*, 1:405–418, June 1975. DOI 10.1007/BF01022471. URL `https://link.springer.com/article/10.1007%2FBF01022471`.

[MG19] C. Müller-Gatermann, A. Dewald, C. Fransen, et al. Shape coexistence in ^{178}Hg, *Phys. Rev. C*, 99:054325, May 2019. DOI 10.1103/PhysRevC.99.054325. URL `https://link.aps.org/doi/10.1103/PhysRevC.99.054325`.

[MG21a] Claus Müller-Gatermann. private communication, June 2021.

[MG21b] Claus Müller-Gatermann. private communication, March 2021.

[Mil77] W. T. Milner, C. E. Bemis, F. K. McGowan. Quadrupole and hexadecapole deformations in the actinide nuclei, *Phys. Rev. C*, 16:1686–1687, Oct 1977. DOI 10.1103/PhysRevC.16.1686. URL `https://link.aps.org/doi/10.1103/PhysRevC.16.1686`.

[Mos89] M. Moszyński, H. Mach. A method for picosecond lifetime measurements for neutron-rich nuclei: (2) Timing study with scintillation counters, *Nuclear Instruments and Methods in Physics Research Section A: Accelerators, Spectrometers, Detectors and Associated Equipment*, 277(2):407–417, 1989. DOI https://doi.org/10.1016/0168-9002(89)90770-5. URL `https://www.sciencedirect.com/science/article/pii/0168900289907705`.

[New21] Matt Newville, Renee Otten, Andrew Nelson, et al. lmfit/lmfit-py 1.0.2. Zenodo. Feb 2021. DOI 10.5281/zenodo.4516651. URL https://doi.org/10.5281/zenodo.4516651.

[Nik68] V.S. Nikolaev, I.S. Dmitriev. On the equilibrium charge distribution in heavy element ion beams, *Physics Letters A*, 28(4):277–278, 1968. DOI https://doi.org/10.1016/0375-9601(68)90282-X. URL https://www.sciencedirect.com/science/article/pii/037596016890282X.

[Nik06] J. Nikkinen, S. Fritzsche, S. Heinäsmäki. Revised and extended Utilities for the Ratip package, *Computer Physics Communications*, 175(5):348–358, 2006. DOI https://doi.org/10.1016/j.cpc.2006.04.010. URL https://www.sciencedirect.com/science/article/pii/S0010465506001895.

[Nol79] P. J. Nolan, J. F. Sharpey-Schafer. The measurement of the lifetimes of excited nuclear states, *Reports on Progress in Physics*, 42(1):1–86, jan 1979. DOI 10.1088/0034-4885/42/1/001. URL https://doi.org/10.1088%2F0034-4885%2F42%2F1%2F001.

[Nol92] P. J. Nolan. EUROGAM: A high efficiency escape suppressed spectrometer array, Aug 1992.

[O'D09] D. O'Donnell, T. Grahn, D. T. Joss, et al. Spectroscopy of the neutron-deficient nucleus ^{167}Os$_{91}$, *Phys. Rev. C*, 79:064309, Jun 2009. DOI 10.1103/PhysRevC.79.064309. URL https://link.aps.org/doi/10.1103/PhysRevC.79.064309.

[Pag03] R.D. Page, A.N. Andreyev, D.E. Appelbe, et al. The GREAT spectrometer, *Nuclear Instruments and Methods in Physics Research Section B: Beam Interactions with Materials and Atoms*, 204:634 – 637, 2003. DOI https://doi.org/10.1016/S0168-583X(02)02143-2. URL http://www.sciencedirect.com/science/article/pii/S0168583X02021432. 14th International Conference on Electromagnetic Isotope Separators and Techniques Related to their Applications.

[Pak20] J. Pakarinen, J. Ojala, P. Ruotsalainen, et al. The JUROGAM 3 spectrometer, *Eur. Phys. J. A.*, 56, 2020. DOI https://doi.org/10.1140/epja/s10050-020-00144-6. URL https://link.springer.com/article/10.1140/epja/s10050-020-00144-6.

[Pas00] A. Pasternak, Y. Sasaki, A. Efimov, et al. DSA lifetime measurements and structure of positive-parity bands of ^{120}Xe, *European Physical Journal A*, 9:293–297, 2000.

DOI https://doi.org/10.1007/s100500070011. URL https://link.springer.com/article/10.1007/s100500070011.

[Pau95] E. S. Paul, P. J. Woods, T. Davinson, et al. In-beam γ-ray spectroscopy above ^{100}Sn using the new technique of recoil decay tagging, *Phys. Rev. C*, 51:78–87, Jan 1995. DOI 10.1103/PhysRevC.51.78. URL https://link.aps.org/doi/10.1103/PhysRevC.51.78.

[Pav12] I. Pavlovsky, R. L. Fink. Graphene stripper foils, *Journal of Vacuum Science & Technology B*, 30(3):03D106, 2012. DOI 10.1116/1.3693594. URL https://doi.org/10.1116/1.3693594.

[Phy] Physik Instrumente (PI) GmbH & Co. http://www.pi.ws.

[Pro10] M. G. Procter, D. M. Cullen, C. Scholey, et al. Lifetime measurements and shape coexistence in ^{144}Dy, *Phys. Rev. C*, 81:054320, May 2010. DOI 10.1103/PhysRevC.81.054320. URL https://link.aps.org/doi/10.1103/PhysRevC.81.054320.

[Pro11] M. G. Procter, D. M. Cullen, P. Ruotsalainen, et al. Lifetime measurements in the transitional nucleus ^{138}Gd, *Phys. Rev. C*, 84:024314, Aug 2011. DOI 10.1103/PhysRevC.84.024314. URL https://link.aps.org/doi/10.1103/PhysRevC.84.024314.

[Pro12] M. G. Procter, D. M. Cullen, C. Scholey, et al. Electromagnetic transition strengths in $^{109}_{52}$Te, *Phys. Rev. C*, 86:034308, Sep 2012. DOI 10.1103/PhysRevC.86.034308. URL https://link.aps.org/doi/10.1103/PhysRevC.86.034308.

[Pro13] M. G. Procter, D. M. Cullen, M. J. Taylor, et al. Isomer-tagged differential-plunger measurements in $^{113}_{54}$Xe, *Phys. Rev. C*, 87:014308, Jan 2013. DOI 10.1103/PhysRevC.87.014308. URL https://link.aps.org/doi/10.1103/PhysRevC.87.014308.

[Rae08] Alastair I. M. Rae. *Quantum Mechanics*. Taylor & Francis Group, LLC, 5 edition, 2008.

[Rae18] S. Raeder, D. Ackermann, H. Backe, et al. Probing Sizes and Shapes of Nobelium Isotopes by Laser Spectroscopy, *Phys. Rev. Lett.*, 120:232503, Jun 2018. DOI 10.1103/PhysRevLett.120.232503. URL https://link.aps.org/doi/10.1103/PhysRevLett.120.232503.

[Rah08] P. Rahkila. Grain-A Java data analysis system for Total Data Readout, *Nuclear Instruments and Methods in Physics Research, Section A: Accelerators, Spectrometers, Detectors and Associated Equipment*, 595(3):637 – 642, 2008. DOI https://doi.org/10.1016/j.nima.2008.08.039. URL http://www.sciencedirect.com/science/article/pii/S0168900208011698.

[Ram89] S. Raman, C.W. Nestor, S. Kahane, K.H. Bhatt. Predictions of $B(E2; 0_1^+ \rightarrow 2_1^+)$ values for even-even nuclei, *Atomic Data and Nuclear Data Tables*, 42(1):1 – 54, 1989. DOI https://doi.org/10.1016/0092-640X(89)90031-4. URL http://www.sciencedirect.com/science/article/pii/0092640X89900314.

[Ram02] S. Raman, C. W. Nestor, A. Ichihara, M. B. Trzhaskovskaya. How good are the internal conversion coefficients now?, *Phys. Rev. C*, 66:044312, Oct 2002. DOI 10.1103/PhysRevC.66.044312. URL https://link.aps.org/doi/10.1103/PhysRevC.66.044312.

[Rei99] P. Reiter, T. L. Khoo, C. J. Lister, et al. Ground-State Band and Deformation of the $Z = 102$ Isotope ^{254}No, *Phys. Rev. Lett.*, 82:509–512, Jan 1999. DOI 10.1103/PhysRevLett.82.509. URL https://link.aps.org/doi/10.1103/PhysRevLett.82.509.

[Rob13] L. M. Robledo, P. A. Butler. Quadrupole-octupole coupling in the light actinides, *Phys. Rev. C*, 88:051302, Nov 2013. DOI 10.1103/PhysRevC.88.051302. URL https://link.aps.org/doi/10.1103/PhysRevC.88.051302.

[Rös78] F. Rösel, H.M. Fries, K. Alder, H.C. Pauli. Internal conversion coefficients for all atomic shells, *Atomic Data and Nuclear Data Tables*, 21(4):291 – 514, 1978. DOI https://doi.org/10.1016/0092-640X(78)90009-8. URL http://www.sciencedirect.com/science/article/pii/0092640X78900098.

[Sah04] Bejoy Saha. Bestimmung der Lebensdauern kollektiver Kernanregungen in 124-Xe und Entwicklung von entsprechender Analysesoftware. Ph.D. thesis, Universität zu Köln, 2004. URL https://kups.ub.uni-koeln.de/1246/.

[Sar08] J. Sarén, J. Uusitalo, M. Leino, et al. The new vacuum-mode recoil separator MARA at JYFL, *Nuclear Instruments and Methods in Physics Research, Section B: Beam Interactions with Materials and Atoms*, 266(19), 2008. DOI https://doi.org/10.1016/j.nimb.2008.05.027. URL http://www.sciencedirect.com/

science/article/pii/S0168583X08007040. Proceedings of the XVth International Conference on Electromagnetic Isotope Separators and Techniques Related to their Applications.

[Sar11] Jan Sarén. The ion-optical design of the MARA recoil separator and absolute transmission measurements of the RITU gas-filled recoil separator. Ph.D. thesis, University of Jyväskylä, 2011.

[Sar21] Jan Sarén. private communication, May 2021.

[Say17] B. Sayği, D. T. Joss, R. D. Page, et al. Reduced transition probabilities along the yrast line in ^{166}W, *Phys. Rev. C*, 96:021301, Aug 2017. DOI 10.1103/PhysRevC.96.021301. URL https://link.aps.org/doi/10.1103/PhysRevC.96.021301.

[Sch63] Arthur Schwarzschild. A survey of the latest developments in delayed coincidence measurements, *Nuclear Instruments and Methods*, 21:1–16, 1963. DOI https://doi.org/10.1016/0029-554X(63)90081-8. URL https://www.sciencedirect.com/science/article/pii/0029554X63900818.

[Sch80a] U. J. Schrewe, P. Tidemand-Petersson, et al. Alpha decay of neutron-deficient isotopes with 78 $\leq$ Z $\leq$ 83 including the new isotopes 183, 184Pb and 188Bi, *Physics Letters B*, 91(1):46 – 50, 1980. DOI https://doi.org/10.1016/0370-2693(80)90659-0. URL http://www.sciencedirect.com/science/article/pii/0370269380906590.

[Sch80b] U. J. Schrewe, P. Tidemand-Petersson, G.M. Gowdy, et al. Alpha decay of neutron-deficient isotopes with $78 \leqslant Z \leqslant 83$ including the new isotopes ^{183,184}Pb and ^{188}Bi, *Physics Letters B*, 91(1):46–50, 1980. DOI https://doi.org/10.1016/0370-2693(80)90659-0. URL https://www.sciencedirect.com/science/article/pii/0370269380906590.

[Sch86] B. Schwarz, C. Ender, D. Habs, et al. In-beam spectroscopy of ^{224}Th, *Z. Physik A - Atomic Nuclei*, 323:489–490, 1986. DOI https://doi.org/10.1007/BF01313532. URL https://link.springer.com/article/10.1007%2FBF01313532.

[Sch01] G Schiwietz, PL Grande. Improved charge-state formulas, *Nuclear Instruments and Methods in Physics Research Section B: Beam Interactions with Materials and Atoms*, 175:125–131, 2001.

[Sch10] M. Scheck, T. Grahn, A. Petts, et al. Lifetimes of odd-spin yrast states in ^{182}Hg, *Phys. Rev. C*, 81:014310, Jan 2010. DOI 10.1103/PhysRevC.81.014310. URL https://link.aps.org/doi/10.1103/PhysRevC.81.014310.

[Sev79] Kenneth D. Sevier. Atomic electron binding energies, *Atomic Data and Nuclear Data Tables*, 24(4):323–371, 1979. DOI https://doi.org/10.1016/0092-640X(79)90012-3. URL https://www.sciencedirect.com/science/article/pii/0092640X79900123.

[Sii66] Antti Siivola. Alpha-active platinum isotopes, *Nuclear Physics*, 84(2):385–397, 1966. DOI https://doi.org/10.1016/0029-5582(66)90377-4. URL https://www.sciencedirect.com/science/article/pii/0029558266903774.

[Smi95] J. F. Smith, J. F. C. Cocks, N. Schulz, et al. Contrasting Behavior in Octupole Structures Observed at High Spin in ^{220}Ra and ^{222}Th, *Phys. Rev. Lett.*, 75:1050–1053, Aug 1995. DOI 10.1103/PhysRevLett.75.1050. URL https://link.aps.org/doi/10.1103/PhysRevLett.75.1050.

[Tay13a] M. J. Taylor, D. M. Cullen, M. G. Procter, et al. Competing single-particle and collective states in the low-energy structure of ^{113}I, *Phys. Rev. C*, 88:054307, Nov 2013. DOI 10.1103/PhysRevC.88.054307. URL https://link.aps.org/doi/10.1103/PhysRevC.88.054307.

[Tay13b] M. J. Taylor, D. M. Cullen, A. J. Smith, et al. A new differentially pumped plunger device to measure excited-state lifetimes in proton emitting nuclei, *Nuclear Instruments and Methods in Physics Research, Section A: Accelerators, Spectrometers, Detectors and Associated Equipment*, 707:143 – 148, 2013. DOI https://doi.org/10.1016/j.nima.2012.12.120. URL http://www.sciencedirect.com/science/article/pii/S0168900213000028.

[Tay15] M. J. Taylor, D. M. Cullen, M. G. Procter, et al. Oblately deformed isomeric proton-emitting state in ^{151}Lu, *Phys. Rev. C*, 91:044322, Apr 2015. DOI 10.1103/PhysRevC.91.044322. URL https://link.aps.org/doi/10.1103/PhysRevC.91.044322.

[Tee20] B. P. E. Tee, T. Kibédi, B. Q. Lee, et al. Development of a new database for Auger electron and X-ray spectra, *EPJ Web Conf.*, 232:01006, 2020. DOI 10.1051/epjconf/202023201006. URL https://doi.org/10.1051/epjconf/202023201006.

[TES] TESA Technology UK Ltd. https://tesatechnology.com/en-gb/home/.

[The15] Ch. Theisen, P.T. Greenlees, T.-L. Khoo, et al. In-beam spectroscopy of heavy elements, *Nuclear Physics A*, 944:333 – 375, 2015. DOI https://doi.org/10.1016/j.nuclphysa.2015.07.014. URL `http://www.sciencedirect.com/science/article/pii/S0375947415001621`. Special Issue on Superheavy Elements.

[Thi14] R. Thibes, S. Oliveira. General solution to Bateman's differential equations with direct index notation, *International Journal of Pure and Applied Mathematics*, 93:879 – 883, 2014. DOI 10.12732/ijpam.v93i6.11. URL `https://ijpam.eu/contents/2014-93-6/11/`.

[Tor19] L. Torrisi, V. Havranek, M. Cutroneo, et al. Characterization of reduced Graphene oxide films used as stripper foils in a 3.0-Mv Tandetron, *Radiation Physics and Chemistry*, 165:108397, 2019. DOI https://doi.org/10.1016/j.radphyschem.2019.108397. URL `https://www.sciencedirect.com/science/article/pii/S0969806X19302622`.

[Twi86] P. J. Twin, B. M. Nyakó, A. H. Nelson, et al. Observation of a Discrete-Line Superdeformed Band up to $60\hbar$ in ^{152}Dy, *Phys. Rev. Lett.*, 57:811–814, Aug 1986. DOI 10.1103/PhysRevLett.57.811. URL `https://link.aps.org/doi/10.1103/PhysRevLett.57.811`.

[Ulf78] G. Ulfert, D. Habs, V. Metag, H.J. Specht. Lifetime measurements of nuclear levels with the charge plunger technique, *Nuclear Instruments and Methods*, 148(2):369 – 379, 1978. DOI https://doi.org/10.1016/0029-554X(70)90191-6. URL `http://www.sciencedirect.com/science/article/pii/0029554X70901916`.

[Ulf79] G. Ulfert, V. Metag, D. Habs, H. J. Specht. Quadrupole Moment of the 200-ns Fission Isomer in ^{238}U, *Phys. Rev. Lett.*, 42:1596–1599, Jun 1979. DOI 10.1103/PhysRevLett.42.1596. URL `https://link.aps.org/doi/10.1103/PhysRevLett.42.1596`.

[War73] D. Ward, H. R. Andrews, J. S. Geiger, et al. Lifetimes for Levels above the "Rotational Phase Change" in ^{158}Er, *Phys. Rev. Lett.*, 30:493–496, Mar 1973. DOI 10.1103/PhysRevLett.30.493. URL `https://link.aps.org/doi/10.1103/PhysRevLett.30.493`.

[Wat11] H. Watkins, D. T. Joss, T. Grahn, et al. Lifetime measurements probing triple shape coexistence in ^{175}Au, *Phys. Rev. C*, 84:051302, Nov 2011. DOI 10.1103/

PhysRevC.84.051302. URL https://link.aps.org/doi/10.1103/PhysRevC.84.051302.

[Web98] T. Weber, J. de Boer, K. Freitag, et al. Nuclear levels in ^{228}Th populated in the decay of ^{228}Pa, *Eur. Phys. J. A.*, 3:25–48, 1998. DOI https://doi.org/10.1007/s100500050146. URL https://link.springer.com/article/10.1007/s100500050146.

[Zam95] N.V. Zamfir, G. Hering, R.F. Casten, P. Paul. Hexadecapole deformations in actinide and trans-actinide nuclei, *Physics Letters B*, 357(4):515–520, 1995. DOI 10.1016/0370-2693(95)00978-T. URL https://www.sciencedirect.com/science/article/pii/037026939500978T.

[Zum84] J. D. Zumbro, E. B. Shera, Y. Tanaka, et al. $E2$ and $E4$ Deformations in ^{233,234,235,238}U, *Phys. Rev. Lett.*, 53:1888–1892, Nov 1984. DOI 10.1103/PhysRevLett.53.1888. URL https://link.aps.org/doi/10.1103/PhysRevLett.53.1888.

[Zum86] J.D. Zumbro, R.A. Naumann, M.V. Hoehn, et al. E2 and E4 deformations in 232Th and 239,240,242Pu, *Physics Letters B*, 167(4):383–387, 1986. DOI 10.1016/0370-2693(86)91285-2. URL https://www.sciencedirect.com/science/article/pii/0370269386912852.